General Disclaimer

One or more of the Following Statements may affect this Document

- This document has been reproduced from the best copy furnished by the organizational source. It is being released in the interest of making available as much information as possible.

- This document may contain data, which exceeds the sheet parameters. It was furnished in this condition by the organizational source and is the best copy available.

- This document may contain tone-on-tone or color graphs, charts and/or pictures, which have been reproduced in black and white.

- This document is paginated as submitted by the original source.

- Portions of this document are not fully legible due to the historical nature of some of the material. However, it is the best reproduction available from the original submission.

NASA CONTRACTOR REPORT

NASA CR-137640(1)

HVAILABLE TO PUBLIC

DIGITAL SIMULATION OF A COMMUNICATION LINK FOR PIONEER SATURN URANUS ATMOSPHERIC ENTRY PROBE

Part I

by C. A. Hinrichs

Prepared by

MCDONNELL DOUGLAS ASTRONAUTICS COMPANY — EAST
St. Louis, Missouri 63166 (314) 232-0232

NATIONAL AERONAUTICS AND SPACE ADMINISTRATION • WASHINGTON, D.C. • FEBRUARY 1975

FOREWORD

This digital simulation study is a continuation of Contract NAS2-7395 and the previous study report (NASA CR-114739)and was performed under the auspices of the NASA Ames Research Center. The first study concentrated on accurately modeling the communications equipment of relay link and the atmospheric scintillation characteristics of an outer planet. This study optimizes the modulation/demodulation link of the previous study and investigates the impact of various scintillation models. For completeness, this report summarizes the results of the previous report. Both the mean error rate and the acquisition properties of the link are explored. The design of simulated equipment was formulated by the TRW Systems Group under subcontract to McDonnell Douglas Astronautics Company-East. Under both studies magnetic tapes of bit error histories were delivered to the Ames Research Center for evaluation of candidate convolutional code structures.

The author expresses his appreciation for the assistance provided by Mr. T. Grant of ARC who performed the decoding analysis and provided the preliminary decoding results for this report.

TABLE OF CONTENTS

PART I

TABLE OF CONTENTS

(CONTINUED)

TABLE OF CONTENTS
(CONTINUED)

LIST OF PAGES

LIST OF TABLES

TABLE OF CONTENTS

PART II

LIST OF PAGES

DIGITAL SIMULATION OF A COMMUNICATION LINK FOR PIONEER SATURN URANUS ATMOSPHERIC ENTRY PROBE

SUMMARY

A digital simulation study is presented for a candidate modulator/demodulator design in an atmospheric scintillation environment with Doppler, Doppler rate and signal attenuation typical of the conditions of an outer planet atmospheric probe. The simulation results indicate that the mean channel error rate with and without scintillation are similar to theoretical characterizations of the link. In addition the simulation gives information for calculating other channel statistics and generates a quantized symbol stream on magnetic tape from which error correction decoding can be analyzed. Some results from the magnetic tape data analyses are also contained herein.

The receiver and bit synchronizer are modeled in the simulation at the level of hardware component parameters rather than at the loop equation level and individual hardware parameters are identified. The atmospheric scintillation amplitude and phase are modeled independently. Both normal and log normal amplitude processes are studied. In each case the scintillations are low pass filtered.

The receiver performance is given for a range of signal to noise ratios with and without the effects of scintillation. The performance is also reviewed for critical receiver parameter variations.

Part I of this report is the body of the study and is bound. Part II of this report contains the appendices and is unbound.

INTRODUCTION

The objective of the study is to determine the performance and to optimize the design parameters of a communications relay link for an outer planet atmospheric probe. The transmission terminal is a probe within the atmosphere of an outer planet, and the reception terminal is a spacecraft in hyperbolic orbit about the planet. As with most space systems the link is power starved, inferring minimal data rates and coding. The simulated terminals were originally designed to support a Saturn/Uranus mission. In the initial system design (ref. 1), "Saturn/Uranus Atmospheric Entry Probe," the data rate is 44 bits per second which is rate 1/2 coded to 88 symbols per second. The link is unique in two respects: first, because of the low data rate the initial frequency uncertainty due to Doppler and oscillator uncertainties is about 400 times the data bandwidth. Second, atmospheric turbulence may cause significant scintillation of the signal.

Preliminary specifications for the terminals were prepared (Refs. 2 and 3) from which a preliminary hardware design was evolved (Ref. 4). This formed the substance of the original simulation (Ref. 5) wherein the design was further refined, and preliminary link effects were given. Upon investigation of the Modem optimization, an error in normalizing the signal to noise ratio for the previous report was discovered and corrected. It is the intent of this report to stand alone, thus the salient and corrected data from the previous report is included in the background section.

This study has three main objectives: first, to extend the optimization of the receiver, second to investigate additional scintillation models, and third to provide additional magnetic tapes of quantized symbols for Ames Research Center coding analyses.

BACKGROUND

The configuration studied consists of three pieces of equipment: the modulator, the receiver, and the bit synchronizer. The modulator, shown in Figure 1, is a continuous phase frequency-shift-keyed modulator. A premodulation filter was added later during the Modem optimization process. The data symbols drive a 20 MHz VCXO which is upconverted by mixing with a fixed local oscillator to the output frequency. The oscillator will typically switch in 20 microseconds; hence, at an 88 symbol per second rate, the modulation may be considered as true continuous phase frequency shift keying. Other continuous phase modulators were also considered, but discarded because of hardware complexity. They are discussed in Appendix X.

The receiver is shown in Figure 2. The limiters are soft, i.e., only limiting when the signal is very large (typically 13 dB above nominal). This is to protect the circuitry during acquisition (when the gain is wide open, at high signal levels).

Mixer offsets were not simulated since the mixer output drift was only $\pm$0.15% over the anticipated voltage range.

Figure 3 shows the bit synchronizer. This is a conventional early-late gate synchronizer with the addition of a baseline correction circuit to "correct" the effect of large numbers of identical bits causing a voltage bias. As in the case of the receiver proper, the voltage offset of the multipliers was determined to cause only a 4% timing error, and was judged to be small enough to be idealized as zero for the simulation. A 1 Hz loop noise bandwidth (approximately a 20 dB advantage) was chosen to maximize the signal to noise ratio in the loop while maintaining reasonable acquisition times.

In order to simulate the hardware as closely as possible, the approach is to simulate the smallest feasible component. For example, each multiplier and filter in a loop are individually simulated, rather than an expression describing the operation of the loop.

A powerful simulation tool is the concept of complex amplitude notation. It is described in Appendix I.

One of the principal reasons for this simulation was to determine the effects of atmospheric scintillation on the Modem. The Gaussian simulation model of amplitude and phase scintillation is:

$$A(t) = A_0 \ (1 + x(t))$$

and

$$\theta(t) = \theta_0 + \theta_1 t + \theta_2 t^2 + s(t),$$

i.e., a linear variation of the amplitude with its scintillation, x(t), and the phase with its scintillation, s(t). The $\theta_1 t$ and $\theta_2 t^2$ terms represent Doppler and Doppler rate, respectively. The x(t) and s(t) terms are typically taken as low-pass zero-mean Gaussian processes with root variances of 0.23 and 0.47, respectively. The filter corner frequencies are typically 2. and 0.2 Hz, respectively and both roll off in proportion to frequency to the -4/3 power.

The 4/3 frequency rolloff presents significant modeling effort, and is detailed in Appendix II. It was seen that the "more efficient" Z transform approach yielded little or no benefit for a 4/3 order filter, in marked contrast to its effect on integer order filters. Thus, tapped delay lines were employed in the computer routine.

Figure 4a is a block diagram of the simulation transmitter, channel and receiver with Figures 4b and 4c detailing the receiver and bit synchronizer together with the salient program symbols. The receiver is "identical" to the hardware block diagram with three exceptions: first, the simulation receiver starts with the input to the first mixer, the radio frequency amplifier being only a constant; and second, the threshold output is directly connected to the sweep, and third, the soft limiters before the coherent amplitude detector and phase detector are not modeled as they only serve in the hardware to protect the following devices from excessive power. It may be argued that the soft limiters would have an effect during high signal to noise acquisitions. However, this region of operation was judged to be inappropriate in this study. Note also in Figure 4 that a soft output is added to aid in coding analyses. A rationale for setting the quanta levels is found in Appendix III.

An abbreviated flow chart for the error rate routine is presented in Figures 5a and 5b. After the initial conditions are established (data, dimension and complex statements) the conditions for a particular test are read in. Next the loop conditions are calculated (time constants, etc.) and the turbulence delay lines initialized. The routine then generates samples for each bit and the loops exercised. The receiver starts below threshold, i.e., the AGC/AFC must acquire and the number of bits to initial lock is determined. The error counter begins when the receiver and bit synchronizer have locked, typically after the reciprocal of the natural frequency (ω_n) of the bit synchronizer loop or approximately 100 bits. This eliminates the error rate "contamination" by both receiver and bit synchronizer lockup effects. Additionally, three other statistics are tabulated: the bit spacing between errors; the conditional probabilities of each quanta level, given the "preceding" level of the soft decision; and the number of times the AGC signal drops below threshold and the number of bits in that dropout. The printout gives the average number of bits per dropout. If the AGC signal is below threshold, a sweep is activated to acquire the signal. Because of the possibility of amplitude scintillation a resweep initiation delay is incorporated into the hardware. Thus, if the scintillation caused only a short amplitude drop-out, the receiver would not restart the long (in terms of symbols) search operation. The minimum value for the delay is determined by the fading time constants. Typically, the amplitude scintillation has a low-pass characteristic with a 3 dB cutoff at 2 Hz (or 4π radians/second), thus the delay should be greater than 80 msec. The maximum value of the delay is constrained by the Doppler rate and the actual loop parameters, e.g., the amount of drift the VCO will undergo during the signal absence condition. The Doppler rate is 13.3 Hz/sec. Assuming a nominal VCO scale factor of 4 KHz/V, phase detector offsets of 1.2 mv, and a loop filter time constant τ_1 of 0.45 sec, the phase detector offset voltage will charge up the loop filter capacitor at the rate of $\Delta V/\tau_1 \approx 2.7$ mv/sec and the VCO will then drift at approximately 10.7 Hz/sec so the total loop drift, including Doppler rate, is of the order of 24 Hz/sec. Since the receiver has a lock-in range of 38 Hz ($\Delta f_L \approx 2\zeta f_n$), the delay should be less than 1.6 sec. Given these two extrema, a time constant of 0.5 sec is recommended to delay the start of sweep after the lock indicator indicates loss of lock. This value could be varied if tests indicate a better

value. The routine then continues until the specified number of bits has been processed. A complete list of symbols is found in Appendix IV, and a complete listing in Appendix V. The language is standard Fortran IV. No special computer library subroutines are required for either the error rate or acquisition routines.

A typical error rate printout is found in Figure 6. Block 1 has the test set-up (signal level, bandwidths, etc.). Block 2 has the mean error rate data and signal amplitude statistics. For this run of 7 dB E/No, the mean error was .035 with a standard deviation of .0041. Lockup occurred in ten bits, but there were 16 AGC dropouts averaging 1.75 bits long. Block 3 is the error spacing matrix, where for this run (reading left to right and top to bottom) 11 bits were in error 1 bit spacing apart, 0 bits 2 spacing, 3 bits 3 spacing . . . 3 bits with 100 or greater spacings. In this run a moderate amount of "burstiness" occurred, i.e., errors not randomly spaced. Block 4 is the data for four conditional probability matrices, which are read with the aid of the figure in the block. The columns of the matrix signify the received quantized level of the current symbol and the rows signify the level of the preceding symbol. The most negative levels occur in the first column and the first row, or the upper left position. For example, given the transmission was -1, -1, which occurred 480 times, the most negative level occurred in both symbols only 4 times. For this matrix the -v, -v quadrant contains all the "corrects", the +v, -v and -v, +v quadrants single errors and the +v, +v quadrant double errors. The quadrant sums are printed out below each matrix. For example there are only 2 double errors for the -1 -1 transmission. The matrices are "conditional" as they are the levels Rx, given the transmitted symbols, Tx. They are also "joint" as the sequences +1+1, -1+1, +1-1, -1-1 are separated. Block 5 is the end points of the random number generators in case an extension of this test is required at a later date. Block 6 is a running count of the number of errors which occurred in groups of 252 symbols.

As the complete receiver simulation is somewhat lengthy, plus having special steering and routines for error measurement, a special routine was adapted for acquisition studies with its own steering requirements. An abbreviated flow chart is shown in Figure 7 (the complete annotated routine is in Appendix IV). The initial setup, problem reading and conversions are identical to those

of the error rate routine. In this case, however, Doppler is injected, and after each receiver acquisition trial, another trial is run until enough trials have been made to determine the probability of acquisition under the initial conditions. It should be noted on the simulation block diagram that the Doppler is injected as a loop stress, rather than a phase time product at the input. Comparing the loop responses in the two cases reveals identical baseband performance even though the double frequency terms which are filtered out are slightly different. Returning to the flow chart, after each acquisition trial, intermediate results are printed. For each trial the receiver is reinitialized and samples are generated. If the sweep goes past the input Doppler, a miss is registered. If the AGC signal goes above threshold an acquisition may have occurred. A check of whether the sweep got to the Doppler determines whether the condition was a true or a false acquisition.

A typical acquisition printout is shown in Figure 8. Blocks 1 and 2 are as stated before. Block 3 shows the conditions at the end of each trial. On the first, third, and twenty-fifth sweep attempts, false acquisitions occurred. On the fourth sweep attempt the signal was missed. All other attempts were successful. The fifth column contains the bit count at the end of that run, the following three columns give the sweep voltage, its value after the AFC loop filter, and the value input to the bit synchronizer.

During the "fabrication" of the acquisition software, it was found that serious aliasing could occur if the sample rate were insufficient. Referring to the input mixer in Figure 4, it is seen that as far as the computer is concerned it is merely multiplying two strings of complex numbers. If they appear to correlate after filtering, large correlated numbers (rather than random zero mean numbers) are detected in the coherent amplitude detector circuit signifying lock. Now, if the samples are widely spaced in time relative to the period of the offset frequency, apparent correlation due to aliasing can occur. This happens periodically when uniformly sweeping the VCO, resulting in a false acquisition. Because of the relatively low sweep rates, this condition occurred long enough for the CAD filter to respond. During the error rate studies a sample rate of 44 samples per bit was used, however, when this rate was used in the acquisition studies, false acquisitions always occurred. The

sample rate had to be increased to 200 samples per bit for 1 kHz Doppler before the aliasing effect was negligible. Higher Doppler shifts would require correspondingly higher sampling rates. Therefore, the acquisition studies were run at 1 kHz offset frequency to conserve computer time.

Figure 9 is an abbreviated flow diagram of the computer routine used to generate the magnetic tapes for the ARC coding analysis. A complete listing is given in Appendix XIII. The receiver portion of the software is identical to that of the error rate routine, but special steering and bit packing is required to generate the 1/2 inch, 556 bits per inch, 7 track tape in the required format. The format begins with a 25 word, 25 bit per word heading in truncated ASCII. This contains the problem set-up data. This is followed by n (usually 10) records, each of which has a 48 bit start time, a 24 bit record number, then 30240 bits of data (in sign-magnitude octal words) and finally a 48 bit stop time. The bulk of the programming is to adapt the CDC 6600 60 bit words into the tape format. As seen in the figure, the data symbols are first broken into 10080 symbol groups (yielding the 30240 bits of octal "data"). The 30360 total record bits are thus 506 CDC words. CDC word 1 is the 48 bit time of start plus 12 bits of the record number. CDC word 2 is the last 12 bits of the record number plus 48 bits of data. CDC words 3 through 505 are data. CDC word 506 is 12 bits of data plus the 48 bit end of record time. The special programming thus consists of partitioning CDC words 2 and 506, "packing" or "filling" the words and "assigning" them once filled. When all 506 60 bit words are assigned, that record is written.

Some subroutines used in the checkout phases, but not used in the production runs, are given in Appendix VII.

There are no significant differences in the programming between the current report and the previous report, although superficially many differences appear to exist. The greatest cosmetic difference is the "elimination" of many subroutines. It was found that folding the subroutines into the main program resulted in significant reduction in running time. A few minor differences are the deletion of the local oscillator detuning (detuning made negligible difference in lock up), the elimination of the sample and hold output (the integrator output was always superior), writing Gaussian noise tables with sufficiently small

granularity, and always starting a problem at the same data and noise points for repeatability. Two diagnostics were added, one which is the quadrent sums of the conditional error matrices (representing hard decisions) and one which tabulates the errors in time (usually 252 bit groups).

Unfortunately, the noise was incorrectly normalized in the initial study, see Appendix XI, resulting in an apparent 3 dB advantage. In the following figures, 10 through 18, which are taken from the previous report, this has been corrected. The figures described below all show performance without premodulation filtering (No PMFILT) of the symbols.

The first step in the initial production runs was to determine the performance for nominal parameters as given in Table I. All the performance data points are based on 1900 bit simulation runs. Before this simulation could be done, however, two additional parameters had to be found: the proper threshold level and the AGC gain.

TABLE I
NOMINAL PARAMETERS

Parameter	Symbol	Value
Bit Rate	BRATE	88. bps
Minimum Loop Signal	ENOMIN	9. dB
Tone Separation	DELF	62. Hz
IF Bandwidth	BIF	1000. Hz
AFC Loop Bandwidth	BL2	176. Hz
AFC Phase Error	PHIDEG	10. deg
AFC Pull-In Range	FDIFF	342. Hz
Bit Sync Bandwidth	BL2B	1. Hz
Bit Sync Phase Error	PHIB	10. deg
Bit Sync Pull-In	FDIFFB	5. Hz
AGC Filter Constant	TAU3	.07957
Sampling Filter Constant	TAU4	.001808
Baseline Filter Constant	TAU5	.01808
Doppler Filter Constant	TAU6	.10603
Baseline Filter Gain	A5	.5

Normally the threshold is initially set at some factor greater than the noise-only output, and then varied to minimize dropouts and minimize false acquisitions. For the simulation, the probabilities of a voltage occurring with noise only (herein -20 dB E/N_0, since it was easier to reduce the signal than to eliminate it) and with signal was determined. This is shown in Figure 10.

The AGC signal processor attempts to keep the voltage into the phase detector constant, to keep a constant open loop gain. Normally for a noise-only input, the gain is maximum, (c on Figure 11) and a gain vs signal function ABC on Figure 11 is produced. However, while determining this function during the debugging operation, it appeared that additional gain below "minimum signal" level would be beneficial, particularly in a scintillation environment, e.g., curve ADE or curve AFG. The additional gain herein is termed the dynamic range, DYNR, in the program. Results of such runs are shown in Figure 12. A DYNR of 3 dB appears to offer the best performance with scintillation, and was thus chosen for the nominal conditions.

The first parameter of interest is the E/N_0 effect on the mean error rate. This is shown in Figure 13. The vertical marks about each experimental point indicate the measurement standard deviation. During these first trial runs the data and noise were not reinitialized for each parameter change. Note that these runs count errors even during AGC dropout after initial acquisition. It should be noted that this performance is only to the mean error rate. In a coded system the distribution of errors is also important. Coding analysis is required to evaluate the performance of the system with scintillation. A rationale for setting the quantization levels for coding is given in Appendix III.

Figure 14 shows the mean and standard deviation of a filter and sample output, and that of an integrate and dump output. As seen in the figure there is only a slight increase in "output" signal-to-noise ratio with increased inputs. At E/N_0 of 10 dB we have a mean to standard deviation of 0.45/0.23 (5.83 dB) and at E/N_0 of 14 dB we have a mean to standard deviation of 0.47/0.19 (7.87 dB). There is only a 2.04 dB apparent increase in output for a 4 dB input increase indicating some memory, intersymbol interference, or possibly implied "noncoherent" signal detection at the lower signal levels.

A number of initial performance runs were made to investigate the effects of varying the parameters of the receiver. These may be roughly broken into two cases: system variations, and hardware variations. Table II lists the system variations.

The results of modulation index variation is shown in Figure 15. As expected the optimum is 0.7, with and without scintillation.

TABLE II

SYSTEM PARAMETER VARIATIONS

PARAMETER	VALUES	
DELF (Modulation index oriented)	26.4, 44, 62, 88, 132	Hz
BIF (IF Bandwidth)	500, 750, 1000, 1500, 2000	Hz
BL2 (AFC $2B_L$)	88, 100, 164, 176, 188	Hz
TAU 4 (Sampled Output Filter)	88, 144, 200	Hz

The second system parameter varied, the intermediate frequency bandwidth, is of some implementation importance. If the bandwidth is too narrow the filter could produce sufficient phase shift in the loop to cause instability. An intermediate frequency bandwidth of ten times the loop filter bandwidth, or 1 kHz was initially recommended. Because of the high Q of this device, wider bandwidths might be easier to fabricate. Figure 16 illustrates the data. The runs at and below 1 kHz were run with 40 samples per bit, and those above proportionally higher. Without scintillation, the higher bandwidths give slightly better performance; apparently beginning to level out in the vicinity of 1500-2000 Hz. With scintillation, the "knee" appears to be between 1000 and 1500 Hz.

The results with the receiver loop bandwidth parameters are shown in Figure 17. The nominal 176 Hz bandwidth appeared to be the best choice but was actually less than the optimum as was later discovered.

The final system parameter varied is the corner frequency of the sampling filter. In conjunction with this, the output of the synchronizer integrate-and-dump was also measured. These data, in Figure 18, are a second set of runs, the first being required to optimize the sampling time. It is seen that wider bandwidths degrade the performance, although less dramatically when scintillation is present. The integrate-and-dump output appears to be

uniformly better. Incidentally, the three points shown for each integrate-and-dump output represent one datum; since no parameter change is made for it; the variations are taken to be experimental scatter.

The expected hardware variations are summarized in Table III. Two "worst cases" were defined: (1) ENODB of 12.2, DELF of 66, and BL2 of 164; and (2) ENODB of 12.2, DELF of 60, and BL2 of 188. The simulation results are shown in Table IV. Worst case 2 shows little variation from the nominal, within the standard deviation of the measurement. Worst case 1 shows between 0.5 and 0.75 dB degradation.

TABLE III

HARDWARE VARIATIONS

Parameter	Nominal	Min	Max	Comment
DELF	62 Hz	60	66	Oscillator pulling range accuracy
BIF	1000 Hz	- Negligible -		Crystal manufacturer data
BL2	176 Hz	164	188	RSS estimate of gain changes, and scale factors
SVRHZ	2.2 kHz/sec	2.1	2.3	5% variance to sweep and VCO scale factor
EVMAX-EVMIN	35 kHz	33	37	5% sweep drift and VCO scale factor
TAU3	.07957	.07718	.08196	3% RSS time constant
TAU4	.001808	.001754	.001862	Same as TAU3
TAU5	.01808	.01754	.01862	Same as TAU3

This concludes the presentation of the data from the previous study (Ref. 5). It was seen that: a) an intermediate frequency bandwidth of 1500 Hertz would be better than 1000 Hertz, b) an integrate-and-dump data output would be preferable to a filter and sample, and c) the effects of hardware degradations are within acceptable ranges. The wider intermediate frequency bandwidth and the integrator output were selected for further study. Although not mentioned *per se*, in all trial acquisitions above 12 dB the receiver acquired every time, thus a curve could not be drawn. Lower signal levels will be shown in the following sections.

TABLE IV

ERROR RATE FOR HARDWARE DEGRADATIONS, E/N_0 = 12.2 dB

Conditions	Nominal	Worst Case 1	Worst Case 2
Scintillation	.024737	.043158	.024737
No Scintillation	.008947	.015789	.0084211

MODEM OPTIMIZATION

The background section described the basic simulation routines and reviewed the results of the previous study. The salient characteristics were an FSK modulator with a symbol rate, R_s, of 88 symbols per second and a modulation index of 0.7 R_s (tone separation to data rate) coupled to a PLL demodulator with a second order loop bandwidth, $2B_L$, of 176 Hertz, $2R_s$. This section explores ways of optimizing the Modem, starting with reducing the loop phase error. Computer data for this section is in Appendix VIII. The optimizations concentrate about symbol error rates of .05, typical of that required for decoding, with the assumption that although not optimized at higher signal levels, the design is still acceptable.

First, the optimum loop bandwidth for an FSK signal was reviewed. A phase error analysis in Appendix XII explores in some detail, from a linearized viewpoint, the effects of phase error on the system and concludes that an increased loop bandwidth in the receiver would decrease loop error and thus potentially reduce the error rate. Figure 19 is an extenion of the runs made in generating Figure 17 and shows that the apparent null at a $2B_L$ of 176 Hz was due to the perverseness of random variables. The true null is about 250 Hertz, $3R_s$. The increased errors with narrower loop bandwidth is due to large phase errors creating temporary phase dropouts, while those with wider bandwidth are simply due to additional thermal noise. Figure 20 illustrates this explanation.

The second optimization step was to determine the effects of various premodulation filters. The premodulation filter is assumed to be a second order filter with the bandwidth as a free parameter. This is shown in Figure 21. The bulk of the effects of these parameter variations are simulated at an E/N_o of 7 dB, which with scintillation (the flight situation), cause a symbol error rate near threshold for convolutional codes, i.e., near 0.05. As seen from the figure a premodulation filter bandwidth of 0.7 of the symbol rate, R_s, appears to be optimal for a tone separation of 62 Hertz. Other tone separations have other optimal premodulation filter points, but result in greater errors than a 62 Hertz separation.

The third optimization step was to vary the tone separation (deviation ratio) parametrically while changing the loop bandwidth. As seen from the linearized analysis in Appendix XII, these parameters are interdependent. Figure 22 shows the parametric performance. For a given tone separation there is an optimal bandwidth, the null being fairly broad. The optimal appears to be a 62 Hertz tone separation in a 294 Hertz ($3.3R_s$) BL2.

The effect of dynamic range was reevaluated for the larger loop bandwidth, and is shown in Figure 23. As seen before, some additional gain below "minimum signal" is still advantageous in a scintillation environment. The knee of the curve is 6 dB.

The initial optimization emphasis has been on the AFC loop; next the AGC loop was reviewed. The AGC filter following the coherent amplitude detector had been set at 2 Hertz, to track the amplitude scintillation. With quite small AGC bandwidths, the AGC loop would be stable even with scintillation, but would present a varying signal voltage (and hence loop bandwidth) to the AFC loop, thus increasing the error rate. For quite large AGC bandwidths the AGC loop would be noisy, and both scintillation and nonscintillation cases would have higher error rates. At some intermediate AGC loop bandwidth it would be anticipated that, although the nonscintillation case would suffer somewhat, the scintillation case would improve. Figure 24 illustrates this hypothesis. The voltage from a coherent amplitude detector in an AGC loop is proportional to the logarithm of the power of the signal, Reference 7. Figure 25 illustrates this voltage relationship for the parameters finally selected in this section. In the previous study this relationship was approximated as a constant (18.7) divided by the AGC voltage. In this study, the more exact form (exp(-AKAGC(abs(V)-AKEG))) is used. The simulation AKAGC and AKEG symbols correspond to the $K_A/(20 \log(e))$ and e_g symbols of Reference 7. The equivalent constants for the earlier study (from fitting the 7 and 11 dB points) were AKAGC of .0467 and AKEG of 18.7. This is an AGC loop bandwidth of 5.88 Hertz, WC/2 = (AKEG*AKAGC + 1)/(4*TAU3). Figure 26 illustrates the effect of the TAU3 parameter. As expected, as the bandwidths are decreased without scintillation the error rate drops. However, an error "peaking" occurs near 1 Hertz. This is probably due to beat effects with the 1 Hertz bit synchronizer tracking loop bandwidth. The effect is less apparent with scintillation. The variation of

constant AKAGC shifts the curve somewhat in frequency, and more noteably in error rate. The best compromise (in minimizing the mean error rate) between the scintillation and nonscintillation cases appears to be a gain constant AKAGC of .016 with an AGC filter corner frequency (FBTAU3) of 1.3 Hertz. This corresponds to a 3 Hertz AGC loop bandwidth. In a nonscintillation design the conventional approach would have the AGC loop bandwidth below the bit synchronizer bandwidth. With the nominal model of scintillation, herein a 2 Hertz bandwidth, the reverse appears preferable. This parameter should be adjusted to match the best current scintillation model.

Figure 27 illustrates the performance of the AFC loop with the selected AGC loop parameters. To generate this plot the data was removed so that the phase error could be directly measured, that is, without data or scintillation modulation, the loop phase error is due only to the additive noise. From linear theory the loop phase error is just the root of the reciprocal of the signal to noise ratio, 1/(ENODB/(B_L*T)). At low signal levels (below 5 dB) the phase error increases as expected since the linear theory no longer holds. In the median signal level range (7 to 9 dB) the phase error is less than expected because imperfect gain control reduces the actual noise bandwidth, $2B_L$. From the measured phase error, the double sided AFC loop noise bandwidth is between 240 and 260 Hertz with the corresponding damping ratios of .6 and .64. Recall from Figure 26, that these parameters minimize the mean error rate. At high signal levels the phase error decreases less than the linear model since the steady state gain error of the AGC loop, A/(AKEG*AKAGC), increases with A, the signal level thus increasing $2B_L$.

The frequency break point of the baseline correction filter (see Figures 3 and 4c) was investigated for various Doppler rates. The data is given in Table V. The mean error rate is independent of the baseline correction filter over the range of parameters investigated.

TABLE V

PARAMETRIC PERFORMANCE WITH
BASELINE FILTER BANDWIDTH AND DOPPLER RATE

FBTAU6 = 1.5

FBTAU5 (Hz)	Mean Error Rate FQDPRT=5.4	FQDPRT=10.8	FQDPRT=21.6
17.6	.036210	.036210	.062996
8.8	.037202	.035714	.061012
4.4	.036706	.035714	.061508

The frequency break point of the level restoring filter (see Figures 2 and 4b) was also investigated for various Doppler rates. The data is given in Figure 28. As expected, extending the low frequency response lowers the error rate since less energy is subtracted from the signal. At the design Doppler rate of 10.8 Hertz/second or less, extension of the response below 1.5 Hertz is not dramatic. At twice the Doppler rate, however, a frequency response down to 0.75 Hertz is quite advantageous.

To complete the mean error rate performance data, 4032 symbol simulations were run for a range of E/N_0's, both with and without the nominal scintillation. The results are given in Figure 29. These performance curves are for the optimized parameters set as indicated above, namely, a 62 Hertz (0.7 R_s) tone separation, a 2 pole premodulation filter with a bandwidth of .7 R_s, and a loop bandwidth ($2B_L$) of 294 Hertz ($3.3R_s$). The complete run conditions are listed in Appendix VIII, pp 100-107. If the decoding analyses does indeed show a threshold at a mean rate of .05, the system E/N_0 threshold is 6.7 to 8.0 dB, dependent upon the degree of scintillation.

The final step was to define the acquisition characteristics at low signal levels. As the AGC circuitry has been changed from the previous study the distribution of signal levels was remeasured, and is shown in Figure 30. The figure shows cumulative function with the noise only (ENODB = -20) case being the probability of exceeding the value, while with the signal cases it is the probability of not exceeding the value. From these distributions, time constants, sweep rates, etc., one can predict the probabilities of acquisition fairly accurately. Measurements of these probabilities from the acquisition program are illustrated in Figure 31 as a function of threshold settings. In this test,

the receiver VCO is set 1000 Hertz low, and sweeps toward the carrier. Obviously for low thresholds it is more probable that the receiver would indicate lock on noise, while for high thresholds the machine would sweep through the signal without exceeding threshold. At an ENODB of 7, a -17 volt threshold maximizes the probability of true acquisition. Figure 32 shows the effect of variable signal levels for a -17 volt threshold and a -21 volt threshold. At higher signal levels the higher threshold magnitude (the sign is a convention of the mathematics, the magnitude is the threshold) improves the probability of true acquisition, hence there is an optimal threshold for the design point signal level, which is suboptimal elsewhere.

SCINTILLATION MODELS

An important aspect of these simulations is their use to explore the impact of various types of scintillation on the Modem. As seen from the background section, the atmospheric scintillation was assumed to be a filtered normal or Gaussian process: the amplitude having a standard deviation of .23 with a roll off at 4/3 the frequency and a 3 dB bandwidth or corner frequency of 2 Hertz, the phase having a standard deviation of .47 with a roll off at 4/3 the frequency and a 3 dB bandwidth of 0.2 Hertz. This section looks at (a) the effects of varying the magnitudes and bandwidths of the model, (b) looking at a less sophisticated and thus more analytically tractable RC filtered scintillation and, (c) a more sophisticated and probably more realistic log normal model of the amplitude scintillation.

The computer runs for this section are given in Appendix IX. The receiver is the nominal receiver as optimized in the preceeding section, namely, DELF of 62, PMFILT of .7, BL2 of 294, AKAGC of .016, AKEG of 26.44, and TAU3 of .1187.

The effect of the amplitude of the scintillation is shown in Figure 33. As expected, increasing the magnitude of the scintillation above the nominal value of .23, increases the mean error rate. For magnitudes of scintillation below the nominal .23 value, the error rate decreases, but less dramatically than the increase above .23. The slight increase in error rate at a scintillation magnitude of .1626 is probably data scatter. Also shown on the figure is the RC filter approximation at the extremes of amplitude scintillation, as well as at the nominal amplitude scintillation. Simulations of the effect of a range of phase scintillation parameters are not plotted because it was quickly determined that they have negligible effect, and are readily tracked by the receiver. At nominal scintillation the RC and taped delay line filter models show nearly equivalent results, but at the extremes the RC model has a slightly greater error rate. It would be expected that the single pole RC, which has slightly more energy beyond the corner frequency, would result in slightly greater error rates.

The effect of the bandwidth of the scintillation is shown in Figure 34. The curve generally shows an increasing error rate with increasing scintillation bandwidth. However, there is a local minima at the design scintillation band-

width of 2 Hertz. In retrospect, it appears that the receiver optimizations of the preceeding section optimized the design for that scintillation bandwidth. This rather infers that the receiver optimizations are moderately sensitive to the bandwidth of the amplitude scintillation. Also shown on the curve is the RC filter approximation at the extremes. At the large bandwidth extreme, the effects are identical (within the measurement standard deviations), indicating that in both filters significant scintillation power exists at frequencies beyond the receivers tracking capability. At the small bandwidth extreme it appears that the larger degree of scintillation at higher frequencies in the RC filter is causing additional errors.

A comparison of Gaussian amplitude scintillation, (unity amplitude plus a zero mean Gaussian variable) and log normal amplitude scintillation (expodential amplitude with a zero mean Gaussian argument) is shown in Figure 35. From the data it appears that the log normal amplitude scintillation has a greater error rate to signal level slope than Gaussian amplitude scintillation. In the extremes investigated however, the measurement standard deviations nearly overlap meaning that the apparent error rate to signal level slope variation may only be due to experiment scatter. In any case, in the vicinity of .05 mean error rate, a typical target for coded systems, there is little difference between the models.

PRELIMINARY DECODING RESULTS

The objective of the total simulation effort is to define and minimize the required signal-to-noise ratio (E_b/N_o) for a PCM-FM modem under a probable model of the propagation effects. Since error correction coding is postulated to optimize this modem, some decoding performance information is needed to complete the definition of the required E_b/N_o. A direct measure of the decoding performance using the simulated received symbol sequence has been possible via a second program which simulates the decoding.

The decoding program operates on a digital magnetic tape of the detected symbol sequence. It consists of converting the symbol sequence into an equivalent coded sequence, applying two decoding algorithms to the data, and tabulating the results. It also analyzes the symbol sequence in various ways to provide error statistics on the simulated channel.

The program used is a modification of a decoding simulation program previously developed at Ames Research Center for studies with other telmetry channels. It was written in an assembler language and run on an SEL 840 minicomputer. Some preliminary results on a limited set of data tapes are presented here.

The two codes simulated are short- and long-constraint-length convolutional codes, nonsystematic, and of rate one-half. They are decoded via Viterbj/ Maximum Likelihood, and Sequential decoding algorithms, respectively. The Viterby decoder operates on constraint length (K) of 7, rate (R) 1/2 code and the Sequential decoder on a K = 24, R = 1/2 code. Figure 36 delineates the functional capabilities and the processing techniques of the program.

The first step in processing the data is to transform the pseudo-noise (PN) sequence of 63 symbols which were used as a data source for the modem simulation. A correct 63 symbol sequence is half-added to the sign bits of the data, thus forming it into a coded "all zero" sequence without changing the data magnitudes or the errors in the data output. The all zero sequence is unique because it represents almost any convolutional encoding of a data stream of zeros and thus eases the simulation of different decoders and interleavers on the same data. Since the error-correcting properties of the codes

are independent of the data, the all zero sequence is as valid as any other for decoding simulation.

The next step in processing the data is to block it into frames. The program allows selection of one of four frame lengths in multiples of 504 symbols (equivalent to 252 bits for rate 1/2 codes). However, because the data sets processed were only 100 K symbols long, only frames of 504 and 1008 symbols were simulated. The data block or frame size is mainly important to sequential decoding where the probability of error is very low. The critical parameter is a measure of its inability to decode a data segment and is usually expressed as the probability of deleting a frame of data. For Viterbi decoding of the K = 7 code, no deletions occur and a simple measure of the decoded error probability is the key parameter.

The next data processing step is to select the interleaving matrix. Interleaving is used to make symbol errors independent and is a big aid in decoding, as we shall see. In this program the interleaver matrix size is constrained to be a factor of the frame length (e.g., if the frame is 504 = 2·2·2·7·3·3 symbols long, some possible interleavers are: 7x9, 7x18, 21x24, 63x8). However, one might argue that an actual design might be similarly constrained for hardware and operational reasons.

An MxN symbol interleaving process is defined as shown in Figure 37. Code symbols are stuffed into a buffer, M symbols per row and read out, N symbols per column, to the modulator. Then the demodulator/bit synchronizer output is reconstructed into the code via a similar interleaving buffer, and finally decoded. Since an "all zeros" code is used, only the reconstruction interleaver is needed to simulate the interleaving.

The next data processing step is to initialize the decoding decision metric based on the number of quantization levels assigned to each code symbol and their a priori transition probabilities. The symbol quantization levels and transition probabilities are essentially set at the point of generating the data tape. Only three bits (corresponding to 8 levels) per symbol are recorded on the tape and the transition probabilities for these levels are a function of the modem itself, the signal-to-noise ratio, and the quantization constant (or A-D converter gain). However, the quantization levels can be combined by the

decoding program to simulate decoding based on 1, 2, or 3 bits per symbol. Furthermore, the assumed transition probabilities can be set to simulate decoding performance with either good or poor probability estimates.

These preliminary decoding simulations have shown, among other things, that the transition probabilities are much flatter than for a Gaussian channel. (This was of course expected because of the close analogy between the simulated receiver and an FM discriminator). Figure 28 shows by comparison how the transition probabilities, as simulated with different quantization constants, differ from an ideal quantized Gaussian channel. The best quantization is postulated to be with ASOFT = 0.37 (corresponding to 1.3 σ_x quantizing steps) but verification will require further work. This hypothesis is in contra-distinction to the quantization constant recommended in Appendix III, which assumed a Gaussian noise channel. In any case, it appears that decoding performance is <u>not</u> strongly affected by the quantization constant.

The results of these decoding simulations are graphically presented in Figures 39 through 47 and are further described below. Most of the results show Sequential and Viterbi decoding performance in the same format as Figure 39.

The scintillation model used for all the results was a log normal amplitude process with a two Hertz bandwidth and a filter roll off of $f^{-4/3}$. The standard deviation of the amplitude (σ_A) was varied on some data sets. A bandwidth change was also simulated, but the preliminary results are inconclusive. The phase scintillation was modeled as a filtered Gaussian process with σ_ϕ = 0.47, a bandwidth less than or equal to one Hertz, and a filter roll off frequency of $f^{-4/3}$.

Figure 39 shows the conditional Sequential decoding performance as a plot of the probability of deleting (not decoding) a data frame after L trials (after L bit sequences have been tried), with L as an independent parameter. It also shows the Viterbi decoding performance for the same conditions via a table of the decoded error probability per bit and per frame. The variable condition of interest here is the normalized signal-to-noise ratio (E_b/N_0). Other pertinent conditions for these simulations are: the interleaver size of 63 x 16 (1008 symbols per frame were used), the symbol quantization of 3 bits, and the standard deviation of the amplitude scintillation, σ_A = 0.16, except for the

12 db E_b/N_o case where σ_A = 0.23.

Figures 40, 41, and 42 deal with the effects of interleaving. Figure 40 compares the decoding performance for E_b/N_o = 12 dB, and no interleaving (1x1), to an E_b/N_o of 10 dB with a 63x8 symbol interleaver. (The σ_A is worse at 12 dB because equivalent data was not available.) The probability of frame deletion for Sequential decoding appears to be almost identical for deletion rates of 1% or more,* but because of the difference in σ_A, one must conclude that less than 2 dB improvement is achieved. The decoded error rate for the Viterbi decoding shows a degradation for the 10 dB case even with interleaving. Therefore, it appears that the improvement with interleaving is not as great for the shorter convolutional code.

Figure 41 compares decoding performance on the same data set where only the interleaving matrix size is changed. Notice that small matrices given some improvement, but when the full frame is interleaved (63x8, 56x9, and 21x24), a dramatic improvement is achieved.

Two effects are hinted at here which might be worth further consideration: (1) the deletion rate function appears to break away or change slope at lower probabilities as the interleaving matrix becomes larger. (2) The symmetry of the interleaver matrix seems to be unimportant for the long convolutional code with Sequential decoding, but possibility is more important for the short code.

It appears from a more detailed look at the data that error bursts dominate as the cause of frame deletions and Viterbi decoding errors, and therefore an attempt was made to quantify these bursts and correlate them with the decoding performance. A simple measure of the "burstiness" of the symbol errors can be derived from a histogram of the number of errors in a group of symbols.

Figure 42 compares three Group Error Histograms with the expected binominal function for the ideal case of independent errors. The same data set of 100 K symbols was used for each case with the program simulating different interleaver matrices and generating the histograms. The group size of 42 symbols was

*Notice the "D" symbols on the plot near the 500 K trial point. This symbolizes the fact that for the maximum number of trials simulated (in this case, 500 K) there were still some frames undecoded.

selected somewhat arbitrarily; it represents a long-trial sequence for the Sequential decoding, and yet it still provides a significant number of groups (2400/data set) for generating a histogram. The maximum P_e per group is just the maximum number of errors divided by the number of symbols per group (42).

The three cases in this example show the great reduction in bursts obtained with large interleaving: (1) The non-interleaved case had as many as 26 errors in a 42 symbol group and four groups had more than 15 errors. (2) With a 21x8 interleaver only one group had more than 15 errors. (3) With a 63x16 interleaver no groups had more than 6 errors. The results correspond very well with the decoding performance where the non-interleaved case (1) had 3 deleted frames after 500 K trials and Viterbi decoding $P_e = 0.002$, while the fully interleaved case (3) had no deletions and Viterbi decoding $P_e = 0.0002$. A simple measure of decoding performance based on this technique looks promising, but further work is needed to develop it.

Figures 43 and 44 show the effect of quantization on decoding performance. In Figure 43, for $E_b/N_o = 11$ dB and maximum interleaving no difference can be seen in sequential decoding deletion probability for 1 bit versus 3 bit quantization. On the other hand, the Viterbi decoding errors are significantly affected. It should also be noted that for these conditions both decoders can meet the assumed operating requirements (probability of deletion, $P_D \leq 1\%$; probability of error, $P_e \leq 0.1\%$) with either 1 or 3 bit quantization.

In Figure 44, the signal-to-noise ratio is 1 dB lower and now a 1 bit quantization creates a noticeable degradation in the performance of both decoders. In this case the 3 bit quantization is required by both decoders to achieve the assumed operating requirements of $P_D \leq 1\%$, $P_e \leq 0.1\%$. By comparing Figures 43 and 44, it appears that approximately 1 dB of performance improvement is achieved by 3 bit quantization for the Viterbi decoding and somewhat less than 1 dB improvement is achieved by 3 bit quantization with Sequential decoding. Further simulations are required to verify this estimate.

Figures 45 and 46 show the effects of amplitude scintillation on the decoding performance. Figure 45 shows the effect at $E_b/N_o = 11$ dB for maximum interleaving and 3 bit quantization, and Figure 46 shows the effect at $E_b/N_o = 10$ dB for maximum interleaving and 1 bit quantization. (Limited data at 10 dB forced

the use of hard decision decoding for comparisons.) Although the effects are quite noticeable in both comparisons, in Figure 45 the decoders perform better than the operating requirements in all cases, whereas in Figure 46 the decoding performance is marginal without amplitude scintillation and very poor with a standard deviation of 0.23 on the log amplitude. It appears that this magnitude of scintillation represents less than 1 dB of performance loss.

The problem appears to be mainly one of properly estimating the scintillation model, although more simulations are required to extend our knowledge of the effects of more extreme models. It is postulated, for example, that amplitude fading with narrower bandwidths will cause more degradation because the maximum interleaver will not cover slower fades and the receiver will have more time to lose phase lock. The preliminary simulations have not provided conclusive results in this area.

Figure 47 shows the combined performance of the modem with coding in the traditional manner, plotting the mean error rate versus E_b/N_o. The total power-to-noise density (P_T/N_o) is also shown on the x-axis, assuming a 44 bps rate. The figure shows the Sequential decoding threshold for a required deletion rate of 1% (assuming less than 10^6 trials) both for the no interleaving and the maximum interleaving condition. It also shows the Viterbi decoding output bit error rate for the conditions of no interleaving, maximum interleaving, and half the maximum. The uncoded error rate is added as a reference. These results are preliminary but should be sufficient at this time because our present model of the signal scintillation is quite tentative.

CONCLUSION

A digital simulation of a candidate FSK modulator/demodulator in an outer planet relay link environment has optimized the hardware characteristics and investigated the performance for a variety of atmospheric scintillation models. It has been seen that a simplified and linearized expression of the hardware can give significant insight (although not quantitative results) to the performance of the link. Detailed parametric studies of the hardware via simulation have shown that a) a premodulation filter at 0.7 the symbol rate minimize the mean error rate, b) a loop bandwidth of 294 Hertz minimizes the mean error rate with a modulation deviation ratio of 0.7. Detailed analysis of the phase error has shown that the true loop noise bandwidth is between 240 and 260 Hertz near threshold due to imperfect AGC operation. This infers that a hard limiter prior to the phase detector, as recommended in Reference 7, may be an advantageous addition to the receiver. The acquisition studies have shown that the signal can reliably be acquired at signal energy to noise density ratios above 7 dB. The threshold setting is critical however. Based on the distributions of the AGC voltage an optimum search/lock procedure may be formulated for the range of Doppler uncertainties.

Detailed studies of various scintillation models has shown that the link is "relatively" insensitive to the range of bandwidths of the scintillation investigated. It appears that the design was tacitly optimized for the nominal amplitude scintillation bandwidth, and that a slightly different design would result if another nominal scintillation bandwidth were selected. The magnitude of the amplitude scintillation appears to be directly additive to the thermal noise. From a mean error rate viewpoint the more realistic, and also complex, log normal scintillation model is not significantly different than the Gaussian model. The qualifier "from a mean error rate viewpoint" is important here as this link is designed for use with coding and the non-mean characteristics are significant with codes. With similar qualifications, the simpler and less realistic - RC type of scintillation bandwidth model is essentially identical with the previous models.

The preliminary results of the decoding simulations indicate that the telemetry threshold E_s/N_o can be as low as 7 dB if the codes include sufficient interleaving. These results further imply that the accuracy of the estimated threshold is no better than the accuracy of the scintillation model.

Finally, it is seen in Appendix XIV that this link can be adequately described, again from the mean error rate viewpoint, by a theoretical description - both with and without scintillation. This technique can be useful to postulate performance over ranges not specifically simulated (such as more severe scintillation), or in ranges not amenable to detailed simulation (such as higher signal levels).

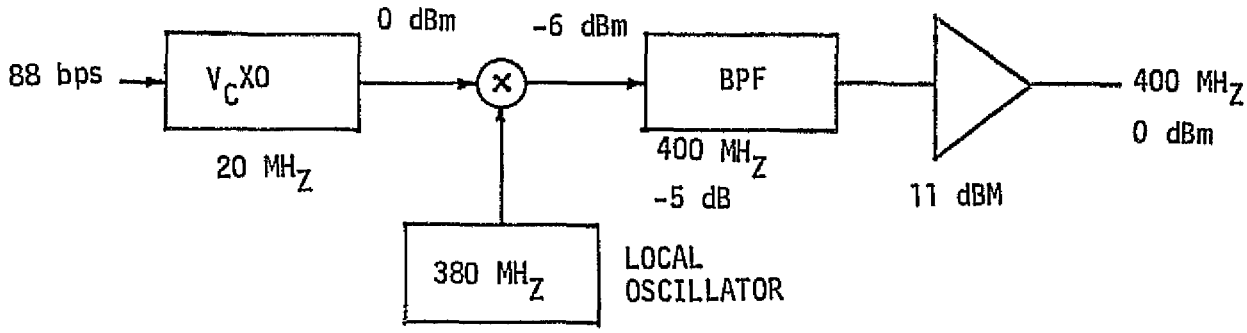

FIGURE 1

SINGLE CONVERSION DIRECT FM MODULATOR

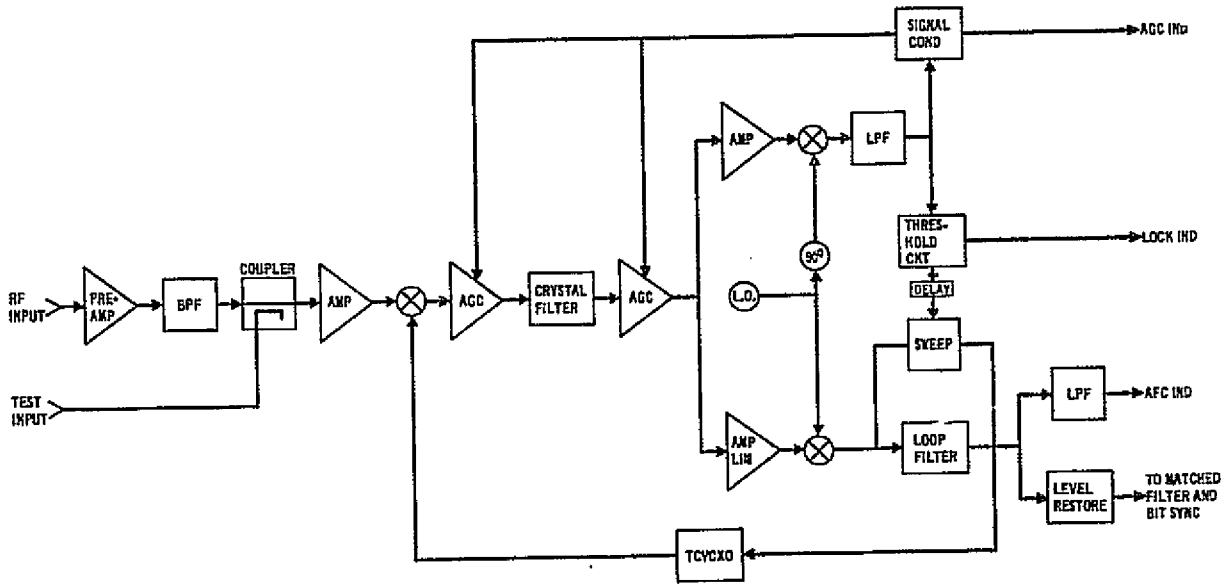

FIGURE 2 RECEIVER DETAILED BLOCK DIAGRAM

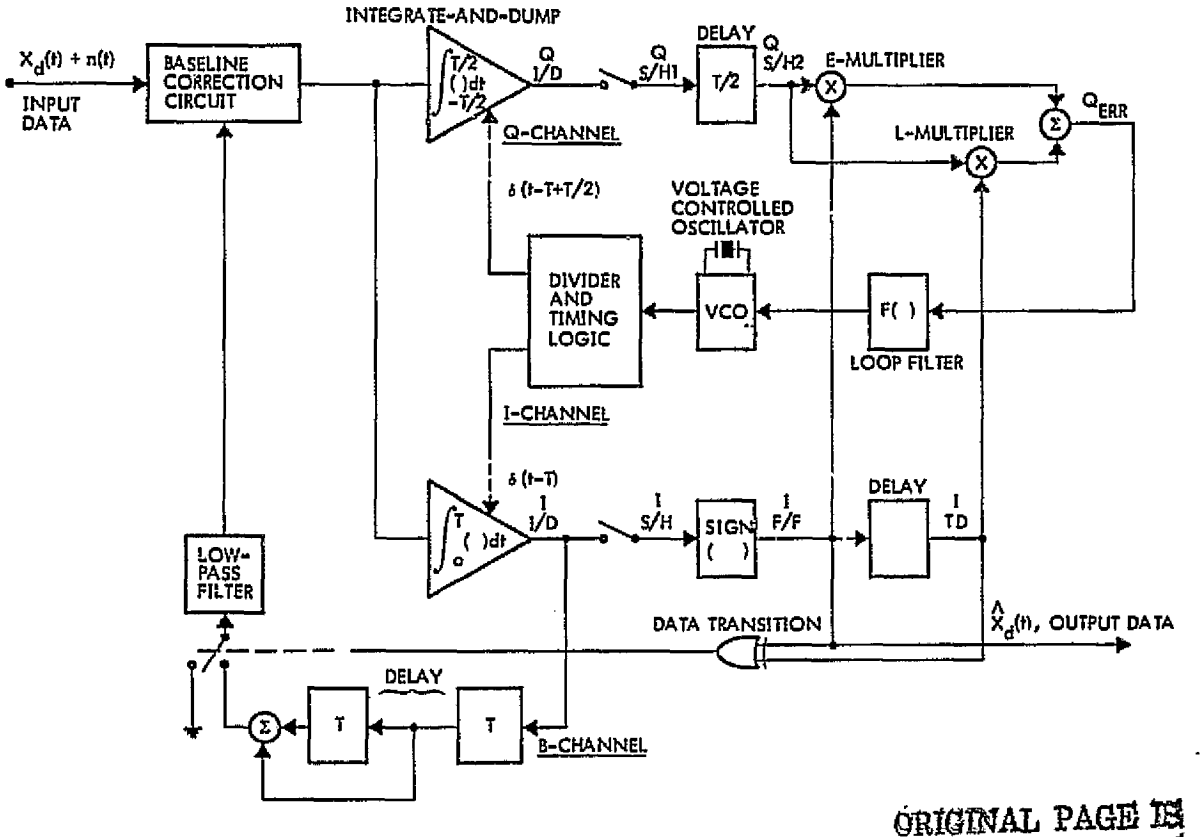

FIGURE 3

BIT SYNCHRONIZER

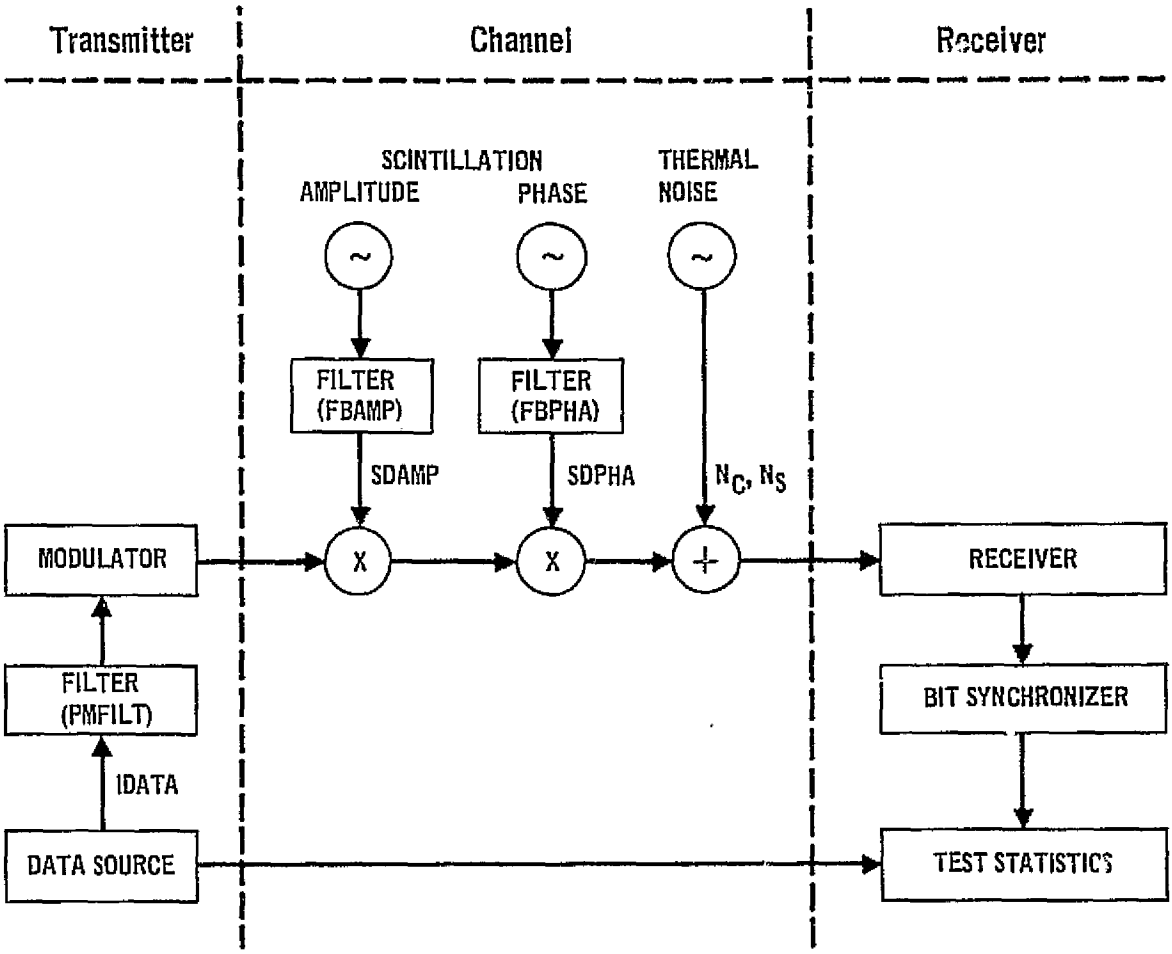

FIGURE 4a SIMULATION BLOCK DIAGRAM

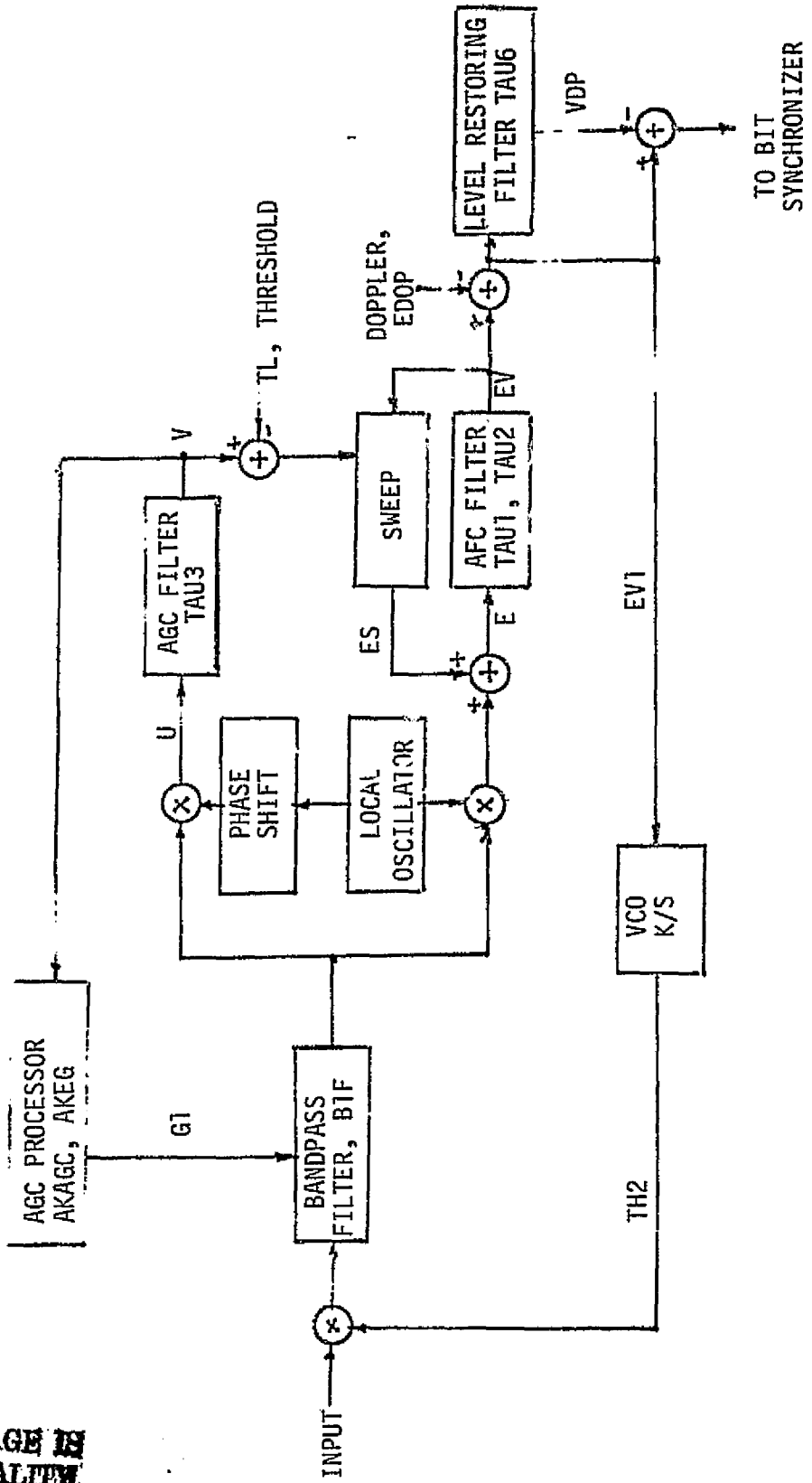

FIGURE 4b
RECEIVER SIMULATION

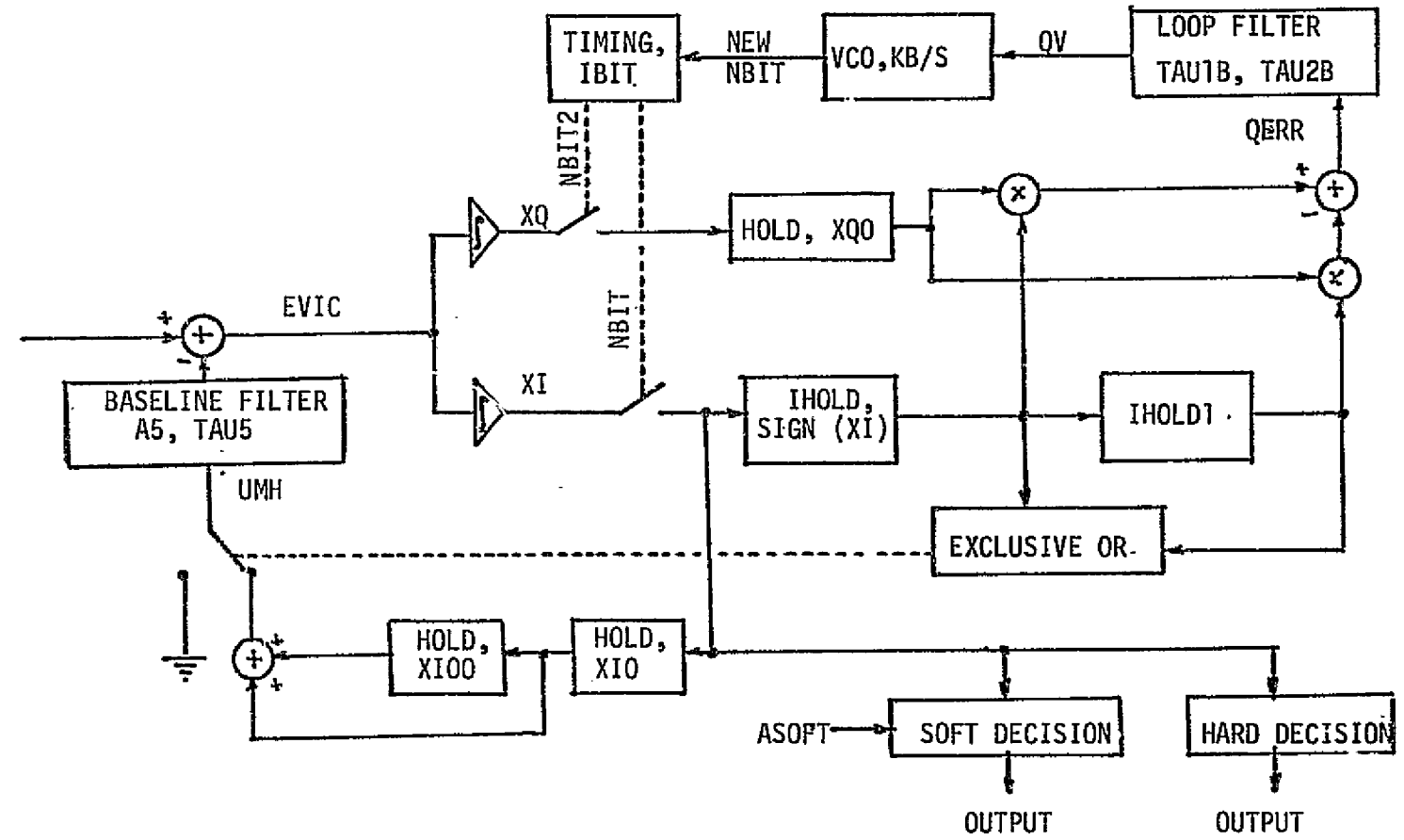

FIGURE 4c
BIT SYNCHRONIZER SIMULATION

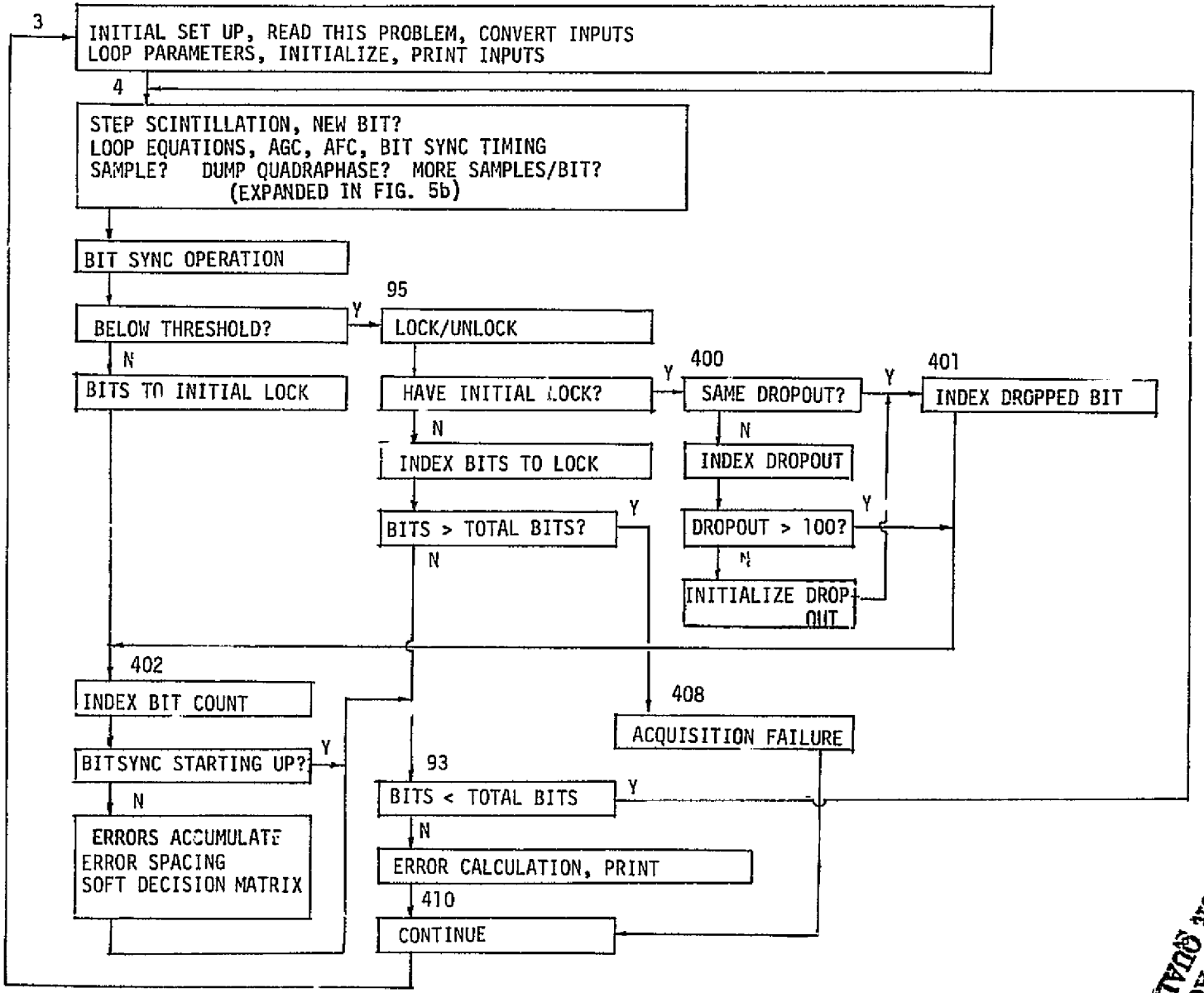

FIGURE 5a
ABBREVIATED ERROR RATE FLOW CHART

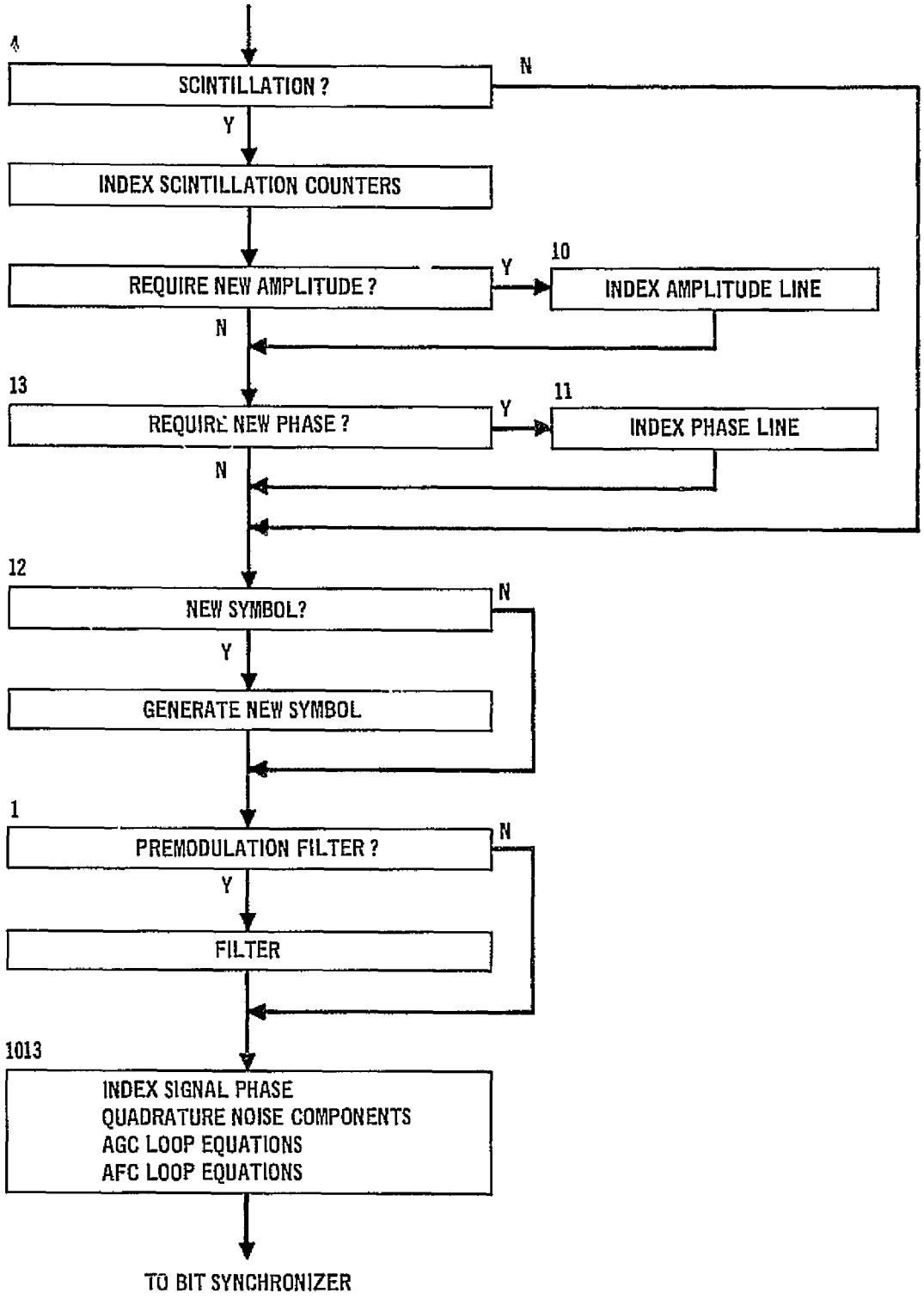

FIGURE 5b. DETAIL OF FIGURE 5a

```
ENJOG=   7.0 ,DELF=  62.5 ,DIF=   1500 ,BL2=    294 ,ASOFT= .3700
FOOPRT=   1.7800E+01 TL=   -6.5000E+00 OYNR=    6.0010E+00
SDAMP=    0.          FRAMP=    2.0002E+00 SDPHA=    0.          FBPHA=    2.0002E-01
WN= 277.2 ,K= 460.6 ,TAU1=  1.8127E-01 ,TAU2=  5.0213E-03 ,WNB=    .9 ,K9= 614.9 ,TAUB1=  2.8353E+02 ,TAUB2=  1.4945E+00
PMFILT=   7.0002E-1
LOG NORMAL SCINTILLATION
FBTAU3=   1.3479E+00 FBTAU5=    4.4028E+00 FBTAU6=    1.5010E+00 ①
PEI=    3.5714E-02 STDEV=    4.1331E-03 BITS=    2816
XISUM=    3.6890E-01 XISIG=    1.8610E-01
LOCKIN=     10 ,DROPOUTS=     16 ,AVE=  1.7500E+00 ,STD DEV=  1.9308E+00 ②
ERRM
  1.1000E+01  0.          3.0000E+00  1.0000E+00  1.0000E+00  2.0000E+00  1.0000E+00  3.0000E+00  1.0000E+00  1.0000E+00
  0.          6.0000E+00  1.0000E+00  1.0000E+00  1.0000E+00  1.0000E+00  1.0000E+00  0.          0.          2.0000E+00
  1.0000E+00  1.0000E+00  1.0000E+00  3.0000E+00  1.0000E+00  1.0000E+00  2.0000E+00  1.0000E+00  1.0000E+00  1.0000E+00
  0.          0.          1.0000E+00  1.0000E+00  0.          2.0000E+00  2.0000E+00  1.0000E+00  1.0000E+00  0.          ③
  0.          0.          0.          0.          0.          0.          0.          1.0000E+00  0.          0.
  1.0000E+00  0.          0.          2.0000E+00  0.          0.          1.0000E+00  1.0000E+00  0.          0.
  0.          1.0000E+00  0.          1.0000E+00  0.          0.          0.          1.0000E+00  0.          0.
  0.          0.          0.          0.          0.          0.          0.          0.          0.          0.
  1.0000E+00  0.          0.          0.          1.0000E+00  0.          0.          0.          0.          3.0000E+00

-1-1 P(R1.R2/T1.T2)TIMES   440                                  -1+1 P(R1.R2/T1.T2)TIMES   512                    ④
     4     8    18    20     1     0     1     1                1     1     0     1     1     0     0     0     0
    23    55    41     7     2     1     0     0                0     0     1     8     2     0     0     0     1
    37    74    46    21     3     0     0     0                0     1     0     2     2     0     0     1     1
    29    33    25     9     1     0     0     0                2     0     2     2     3     0     0     1     1
    11     4     5     1     0     0     0     0                3    12    27    11     3     0     1     1     0
     1     0     0     0     0     0     0     0               19    62    78    28     4     0     0     1     0
     0     0     0     0     0     0     0     0               24    54    49    21     7     0     0     1     1
     0     0     0     0     1     0     0     0               18    30    25    13     1     1     0     0     0
QUADRENT SUMS...HARD DECISIONS                                      13          6
      446          13                                          474          19
      22           2                                          +1+1 P(R1.R2/T1.T2)TIMES   512
+1-1 P(R1.R2/T1.T2)TIMES   512                                     0     0     0     0     0     0     0     0     0
     1     3     0     1    14    54    35    11                0     0     0     0     0     0     0     0     0
     1     0     2     8    54    86    50     8                0     0     0     0     0     0     0     0     1
     0     0     1     9    41    57    18     9                0     0     0     0     0     0     2     3    10
     0     0     1     3    12    16     6     2                0     0     0     0     2    10    44    33    41
     0     0     0     0     0     4     0     1                0     1     0     1    14    56    76    41    27
     0     0     0     1     0     0     1     0                0     0     0     1     7    60    47    27    11
     0     0     0     1     1     0     0     2                3     0     0     1    11    24    17    11
QUADRENT SUMS...HARD DECISIONS
      26          473                                          0          16
       2           11                                          7          489
    58   1861   1358   1293
     9     10     13     14
    17     18     21     22

252 BIT ERROR INTERVALS                                                                                              ⑤
  1.1000E+01  1.3000E+01  3.0000E+00  3.0000E+00  1.4900E+01  9.0000E+00  9.0000E+00  5.0000E+00  0.          0.       ⑥
```

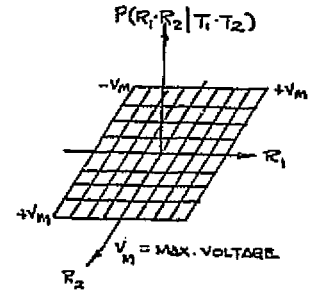

① PROBLEM SET-UP

② ERROR RATE RATE

③ LOCK/UNLOCK, ERROR SPREAD MATRIX

④ CONDITIONAL PROBABILITY MATRIX
(POSITION IN MATRIX DEFINES MAGNITUDE OF RECEIVED SYMBOL PAIR-SEE SKETCH)

⑤ END POINTS OF RANDOM GENERATORS

⑥ TOTAL ERROR AS FUNCTION OF TIME, (252 BIT GROUPING)

FIGURE 6

TYPICAL ERROR RATE PRINTOUT

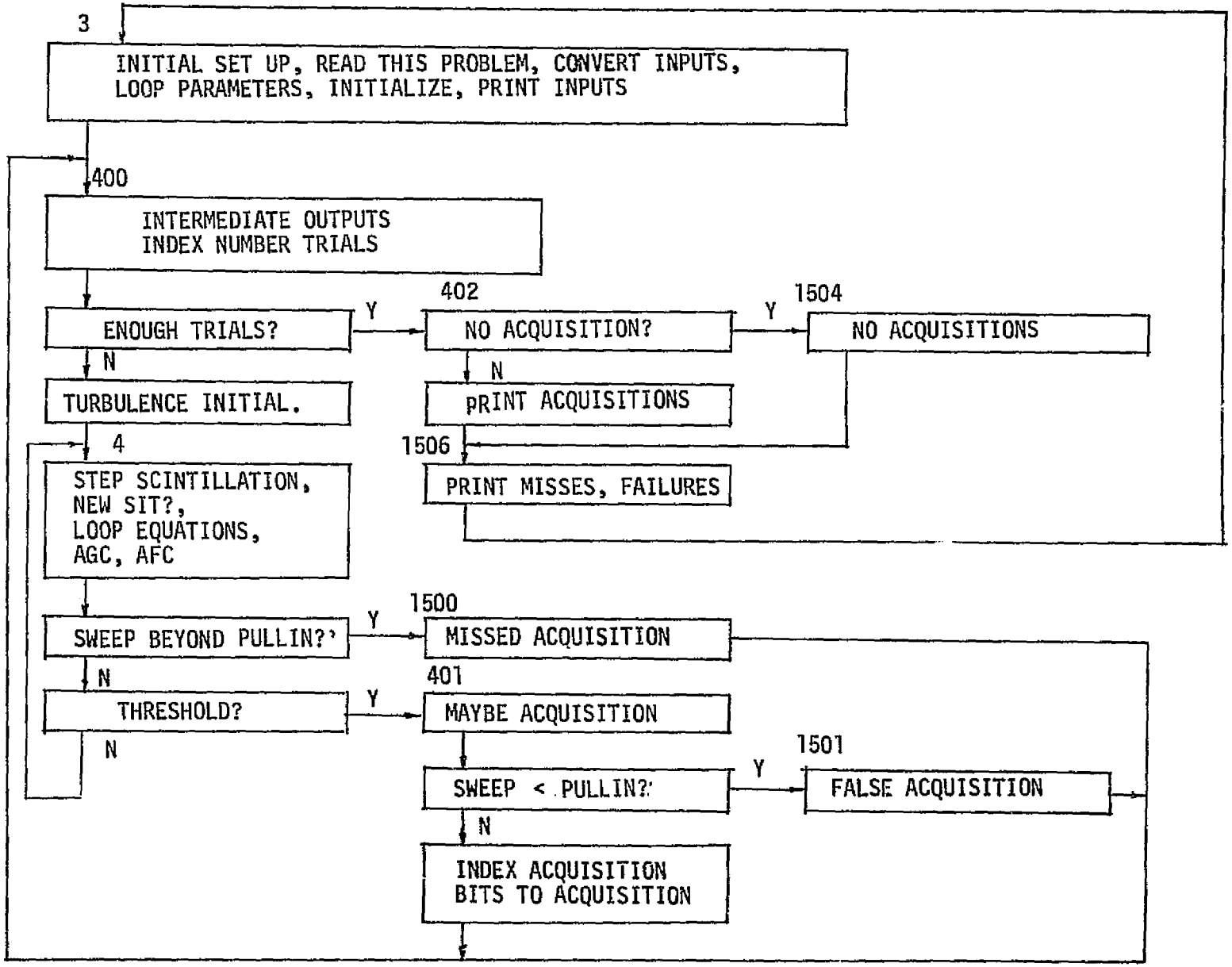

FIGURE 7
ABBREVIATED ACQUISITION FLOW CHART

```
ENGDB=    9.0 ,DELF=   62.5 ,BIF=   1500 ,BL2=    294                                                    (1)
SVRHZ=   2.2000E+03 SWMX=   2.5000E+03 SWMN=   6.8500E+03 FRQDP=   1.0000E+03 FDDPRT=   1.0000E+01
TL= -1.7000E+01 DYNR=   5.0000E+00SCAMP=   2.3000E-01 SDPHA=   4.7000E-01 ____________________
WN= 277.2 ,K= 468.6 ,TAU1=   1.6127E-01 ,TAU2=   5.0213E-03 ____________________________________(2)
PMFILT=   7.0000E-01
LOG NORMAL SCINTILLATION
  NACQ,AMISS          AFAL              ACQ          KDATA,ES            EV             EVI
     1  0.          1.0000E+00   0.                  12  3.7188E+00   9.3874E-01  -1.2553E+01
     2  0.          1.0000E+00   1.0000E+00          58  1.3137E+01   1.3038E+01  -2.7668E-01
     3  0.          2.0000E+00   1.0000E+00           7  2.0429E+00  -5.8016E-01  -1.3965E+01
     4  1.0000E+00  2.0000E+00   1.0000E+00          54  1.7815E+01   1.8810E+01   4.7637E+00
     5  1.0000E+00  2.0000E+00   2.0000E+00          59  1.9472E+01   1.1132E+01  -2.4622E+00
     6  1.0000E+00  2.0000E+00   3.0000E+00          51  1.6791E+01   1.2559E+01  -5.8674E-01
     7  1.0000E+00  2.0000E+00   4.0000E+00          61  2.0143E+01   1.3395E+01  -5.2166E-01
     8  1.0000E+00  2.0000E+00   5.0000E+00          51  1.6791E+01   1.3182E+01  -2.4181E-01
     9  1.0000E+00  2.0000E+00   6.0000E+00          57  1.8802E+01   1.3660E+01   1.6559E-01
    10  1.0000E+00  2.0000E+00   7.0000E+00          51  1.6791E+01   1.3722E+01   6.9340E-02
    11  1.0000E+00  2.0000E+00   8.0000E+00          53  1.7461E+01   1.3091E+01  -3.7729E-01
    12  1.0000E+00  2.0000E+00   9.0000E+00          59  1.9472E+01   1.5108E+01   1.5533E+00
    13  1.0000E+00  2.0000E+00   1.0000E+01          57  1.8802E+01   1.3739E+01   4.5635E-01
    14  1.0000E+00  2.0000E+00   1.1000E+01          55  1.8131E+01   1.2169E+01  -1.7185E-01
    15  1.0000E+00  2.0000E+00   1.2000E+01          73  2.4165E+01   1.4203E+01   8.1451E-01                (3)
    16  1.0000E+00  2.0000E+00   1.3000E+01          53  1.7461E+01   1.3638E+01   9.0269E-03
    17  1.0000E+00  2.0000E+00   1.4000E+01          52  1.7126E+01   1.4842E+01   1.6675E+00
    18  1.0000E+00  2.0000E+00   1.5000E+01          57  1.8802E+01   1.4356E+01   8.2266E-01
    19  1.0000E+00  2.0000E+00   1.6000E+01          55  1.8131E+01   1.4663E+01   1.0965E+00
    20  1.0000E+00  2.0000E+00   1.7000E+01          66  2.1818E+01   1.4587E+01   9.5143E-01
    21  1.0000E+00  2.0000E+00   1.8000E+01          54  1.7796E+01   1.2590E+01  -9.4738E-01
    22  1.0000E+00  2.0000E+00   1.9000E+01          66  2.1818E+01   1.4787E+01   1.4831E+00
    23  1.0000E+00  2.0000E+00   2.0000E+01          57  1.8802E+01   1.3567E+01   1.0297E-01
    24  1.0000E+00  2.0000E+00   2.1000E+01          51  1.6791E+01   1.3483E+01  -2.0832E-02
    25  1.0000E+00  3.0000E+00   2.1000E+01          14  4.3892E+00  -1.2514E+00  -1.2409E+01
    26  1.0000E+00  3.0000E+00   2.2000E+01          76  2.5170E+01   1.4023E+01   5.2532E-01
    27  1.0000E+00  3.0000E+00   2.3000E+01          48  1.5785E+01   1.3281E+01  -2.5610E-01
    28  1.0000E+00  3.0000E+00   2.4000E+01          61  2.0143E+01   1.3444E+01  -4.2479E-02
    29  1.0000E+00  3.0000E+00   2.5000E+01          46  1.5115E+01   1.4047E+01   5.1434E-01
    30  1.0000E+00  3.0000E+00   2.6000E+01          60  1.9837E+01   1.2574E+01  -1.0540E+00 ____________(4)
PACQ=   8.6667E-01 ,STDEV=   6.2063E-02
AVEES=   1.8866E+01 ,STDES=   2.3222E+00
AVEEV=   1.3592E+01 STDEV=   8.6566E-01
AVE KDATA=   5.7192E+01 ,STD DEV=   6.3283E+00
PR MISSED ACQ=   3.3333E-02
PR FALSE ACQ=   1.0000E-01
```

(1) INPUTS

(2) LOOP VALUES

(3) INTERMEDIATE VALUES

(4) ACQUISITION PROBABILITIES

FIGURE 8

TYPICAL ACQUISITION PRINTOUT

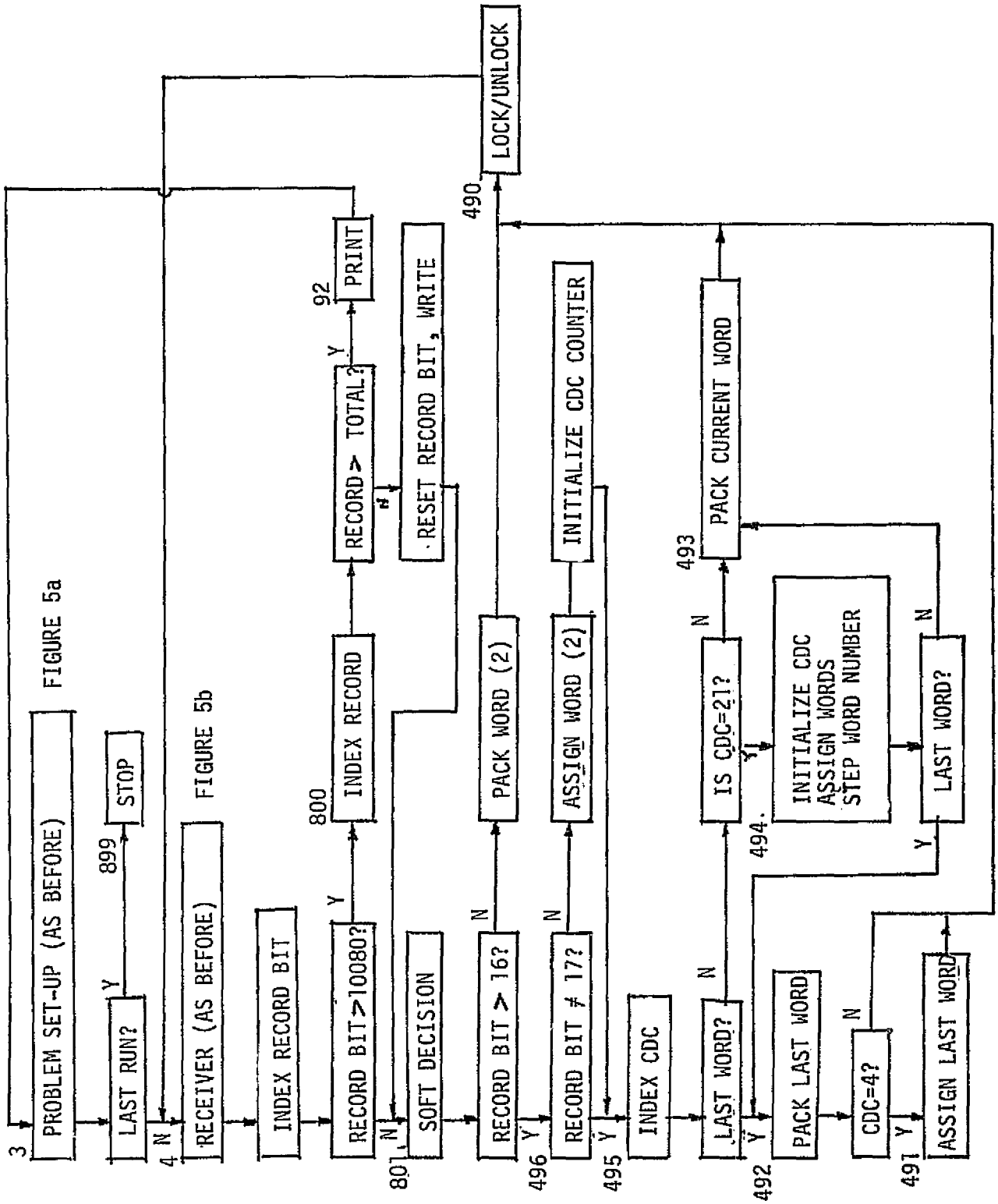

FIGURE 9
ABBREVIATED TAPE GENERATION FLOW CHART

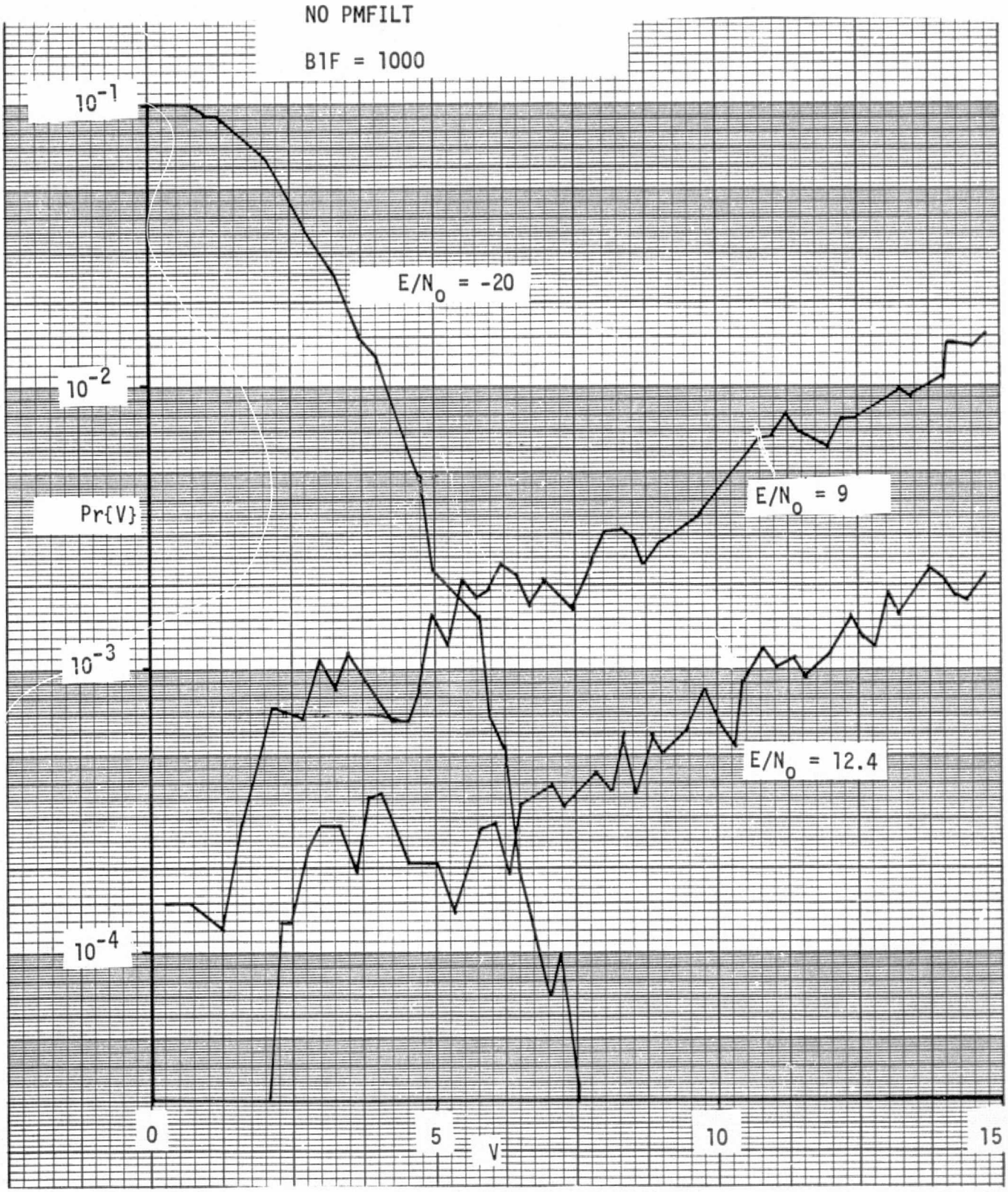

FIGURE 10
AGC VOLTAGE DISTRIBUTION

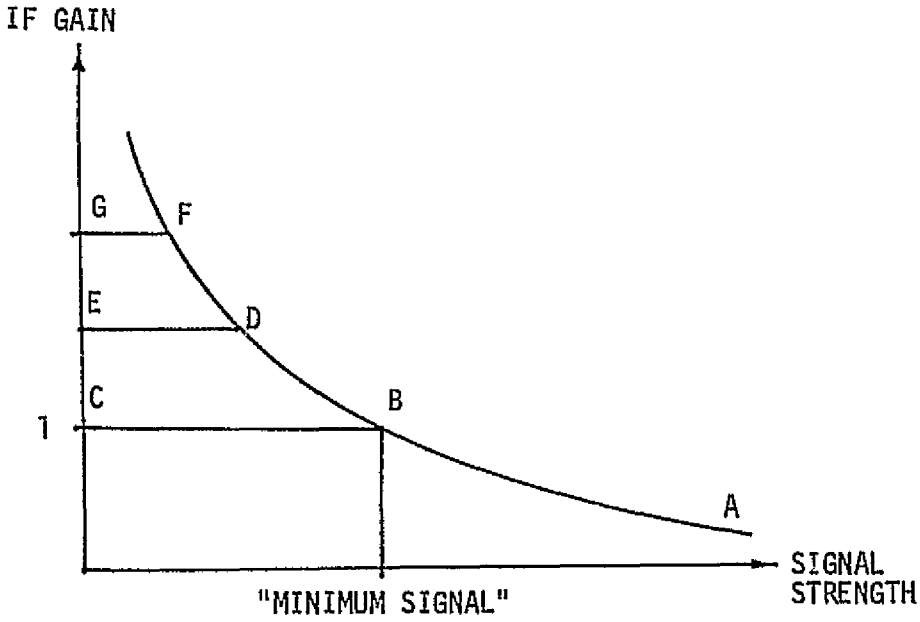

FIGURE 11

AGC GAIN FUNCTION

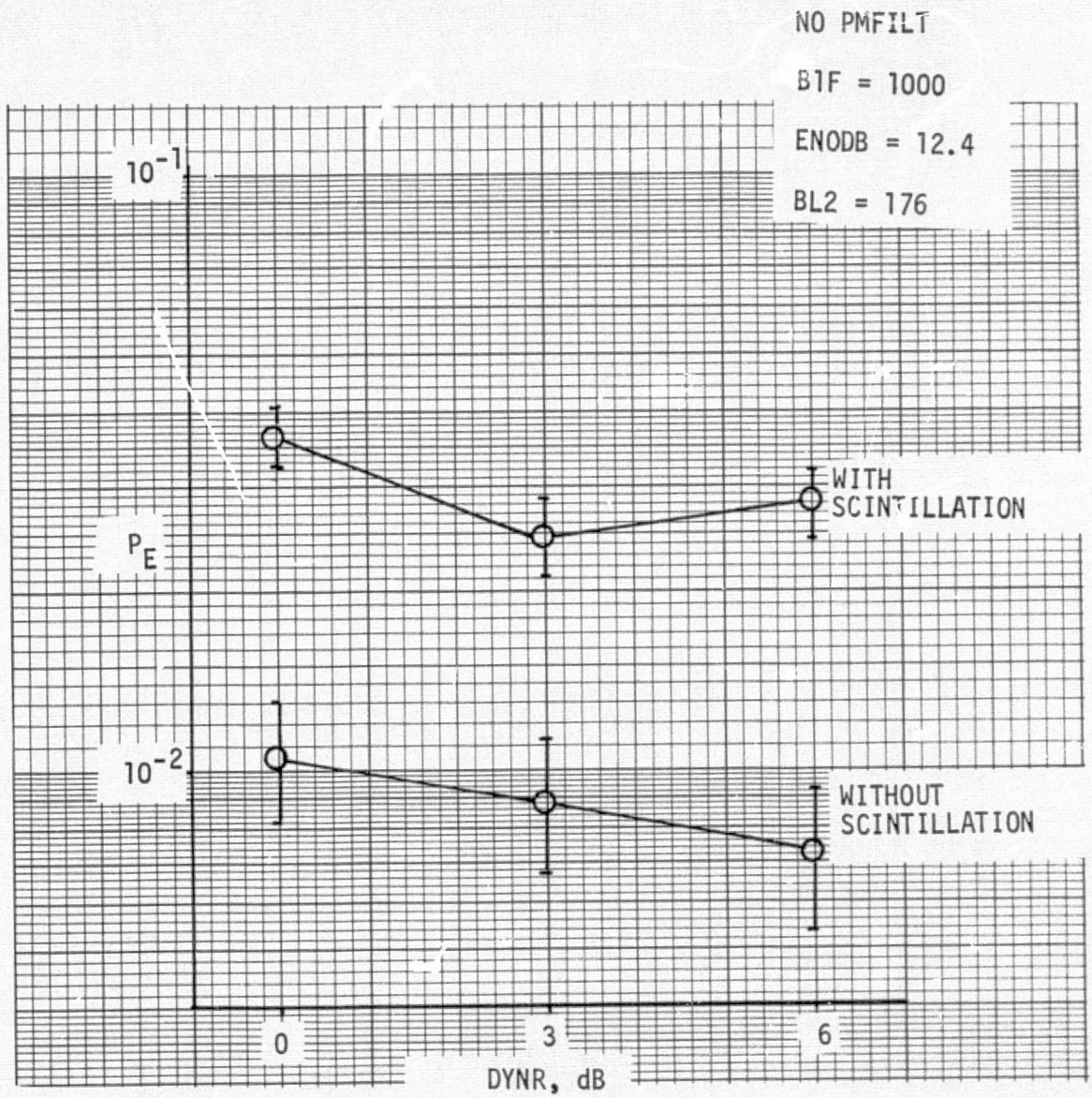

FIGURE 12

MEAN ERROR RATE VERSUS
AGC DYNAMIC RANGE PARAMETER

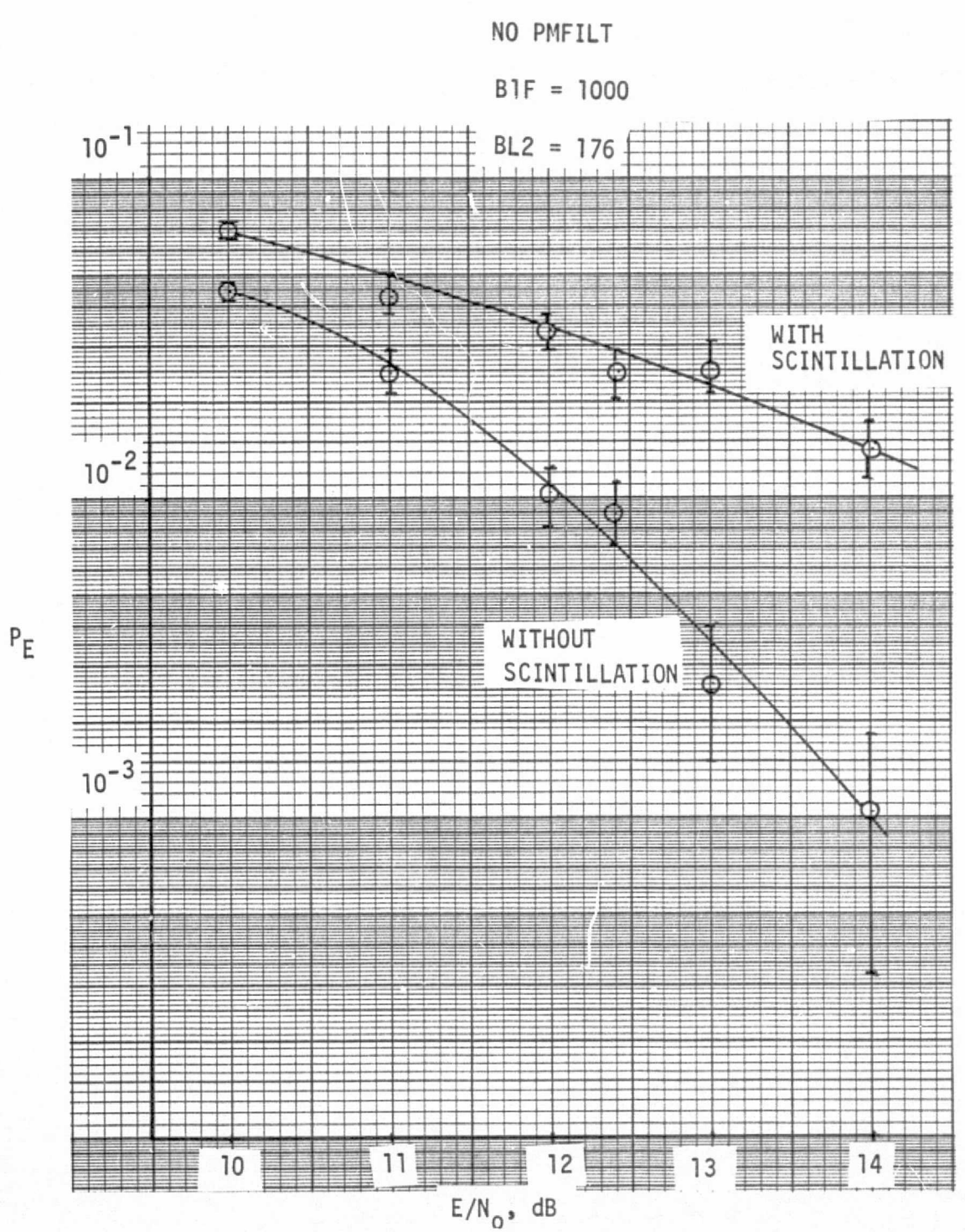

FIGURE 13

MEAN ERROR RATE VERSUS E/N_o
FOR NOMINAL CONDITIONS
(NO PREMODULATION FILTER)
EARLY STUDY

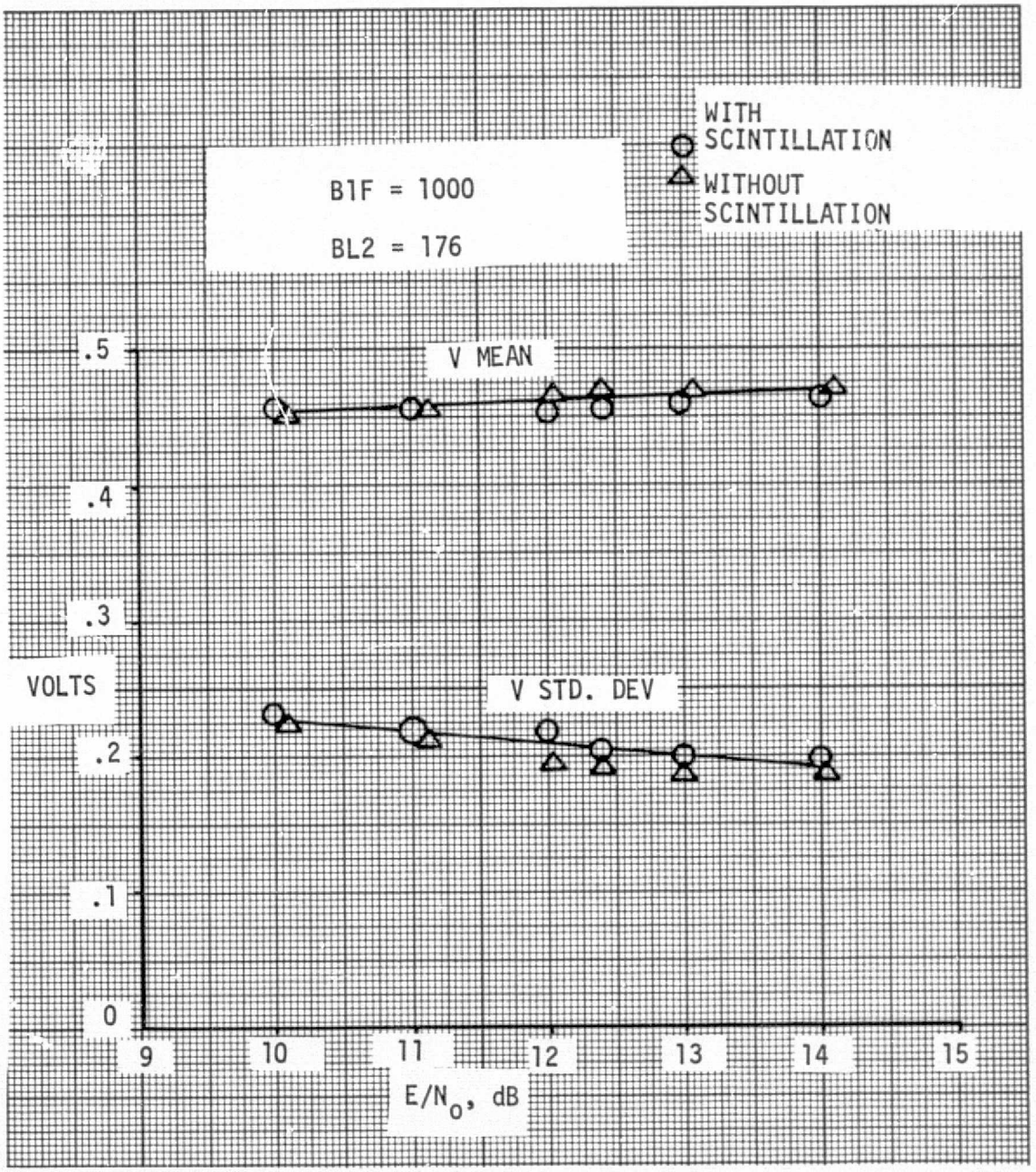

FIGURE 14

FILTER AND SAMPLE OUTPUT
VOLTAGE VERSUS E/N_0
(EARLY STUDY)

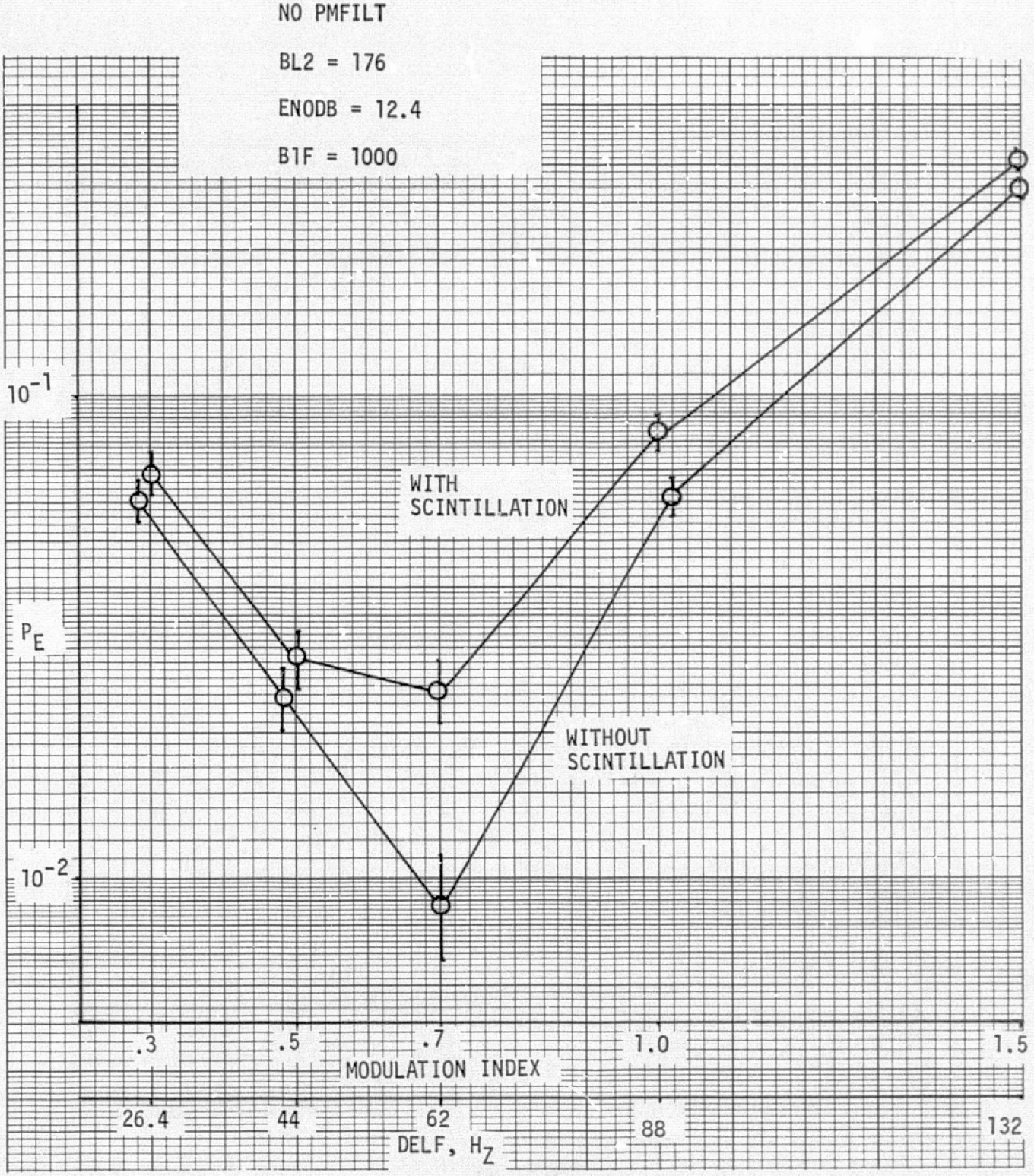

FIGURE 15

MEAN ERROR RATE VERSUS
MODULATION INDEX PARAMETER
(EARLY STUDY)

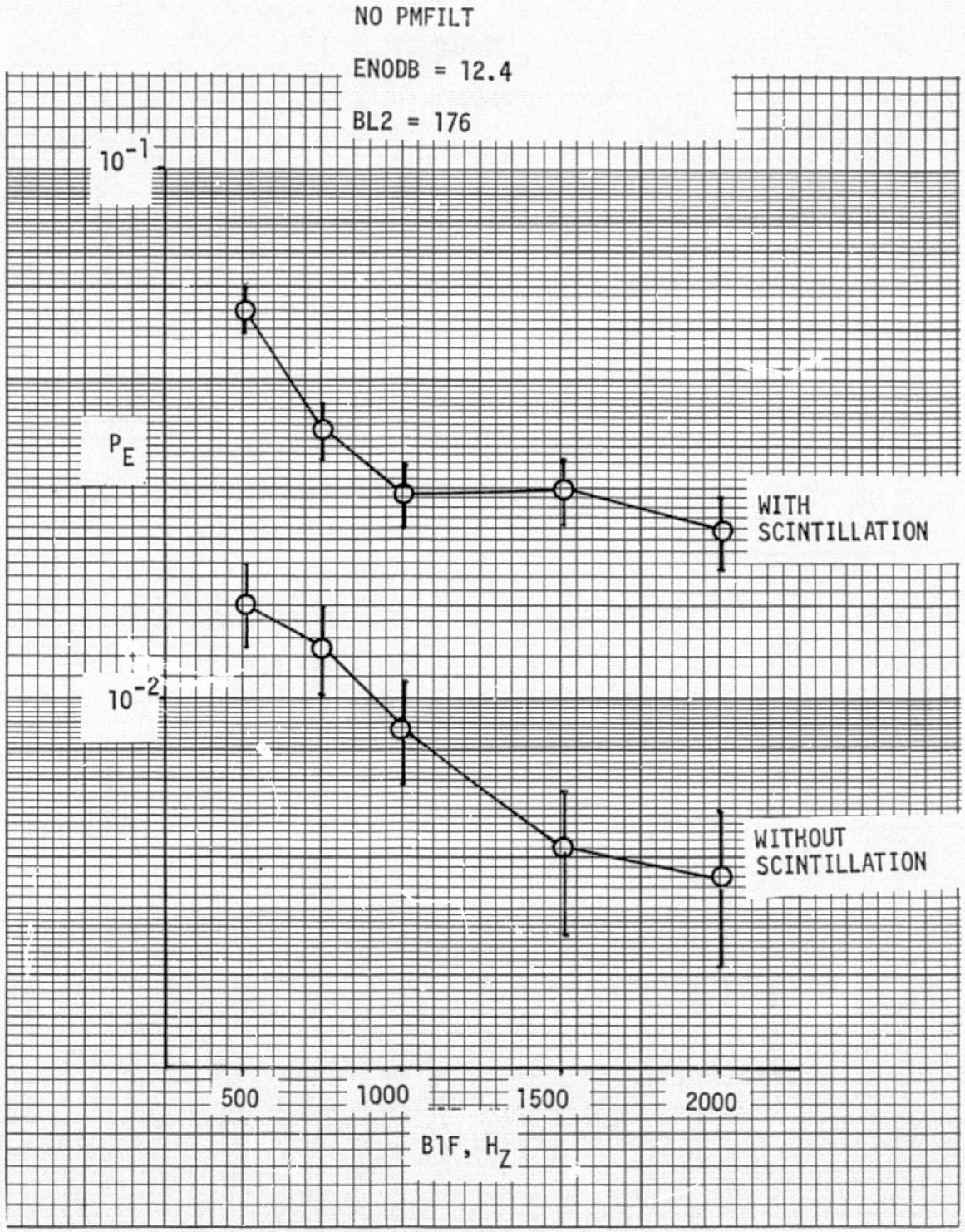

FIGURE 16

MEAN ERROR RATE VERSUS
B1F PARAMETER
(EARLY STUDY)

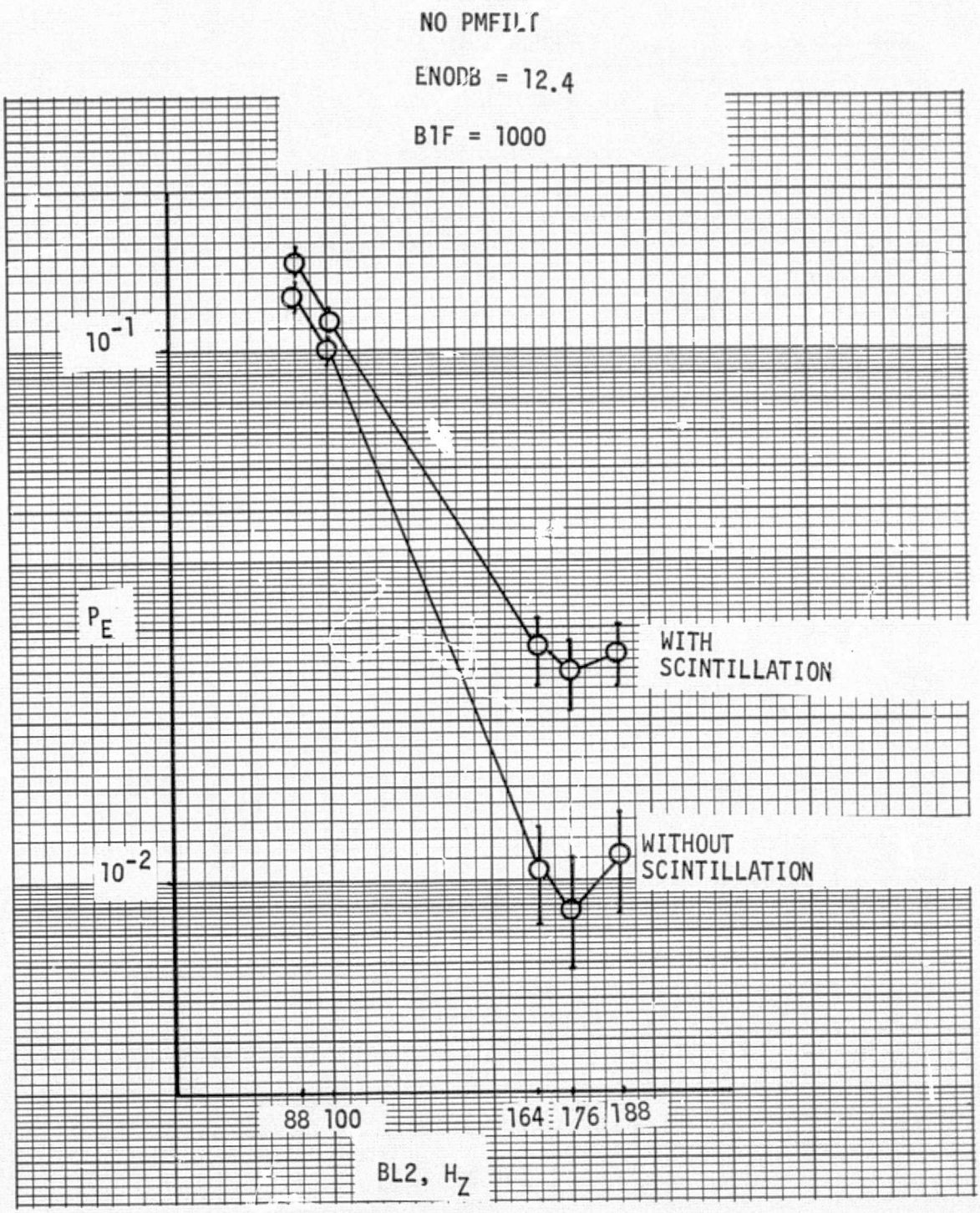

FIGURE 17

MEAN ERROR RATE VERSUS

BL2 PARAMETER
(EARLY STUDY)

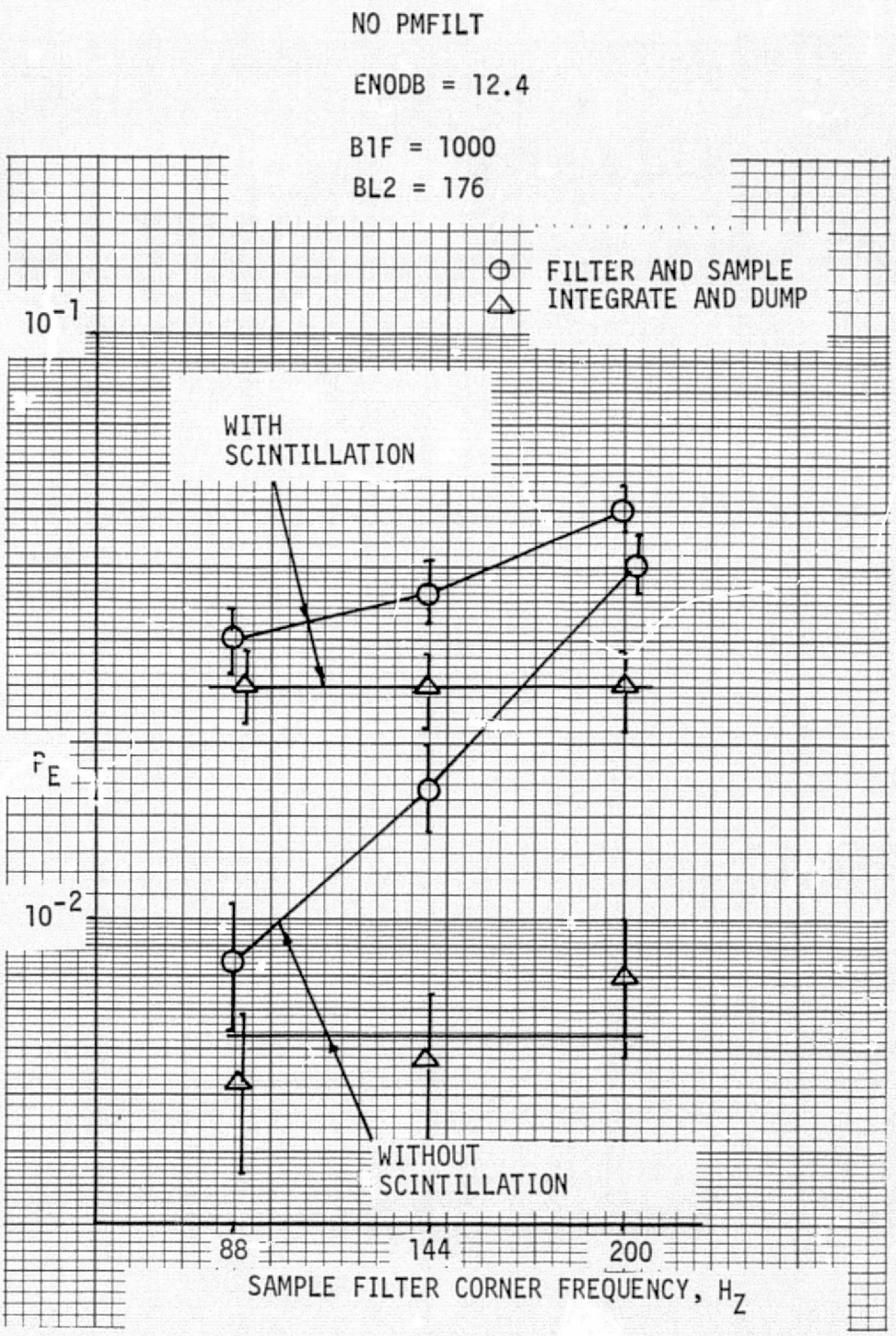

FIGURE 18

MEAN ERROR RATE VERSUS

TAU4 PARAMETER
(EARLY STUDY)

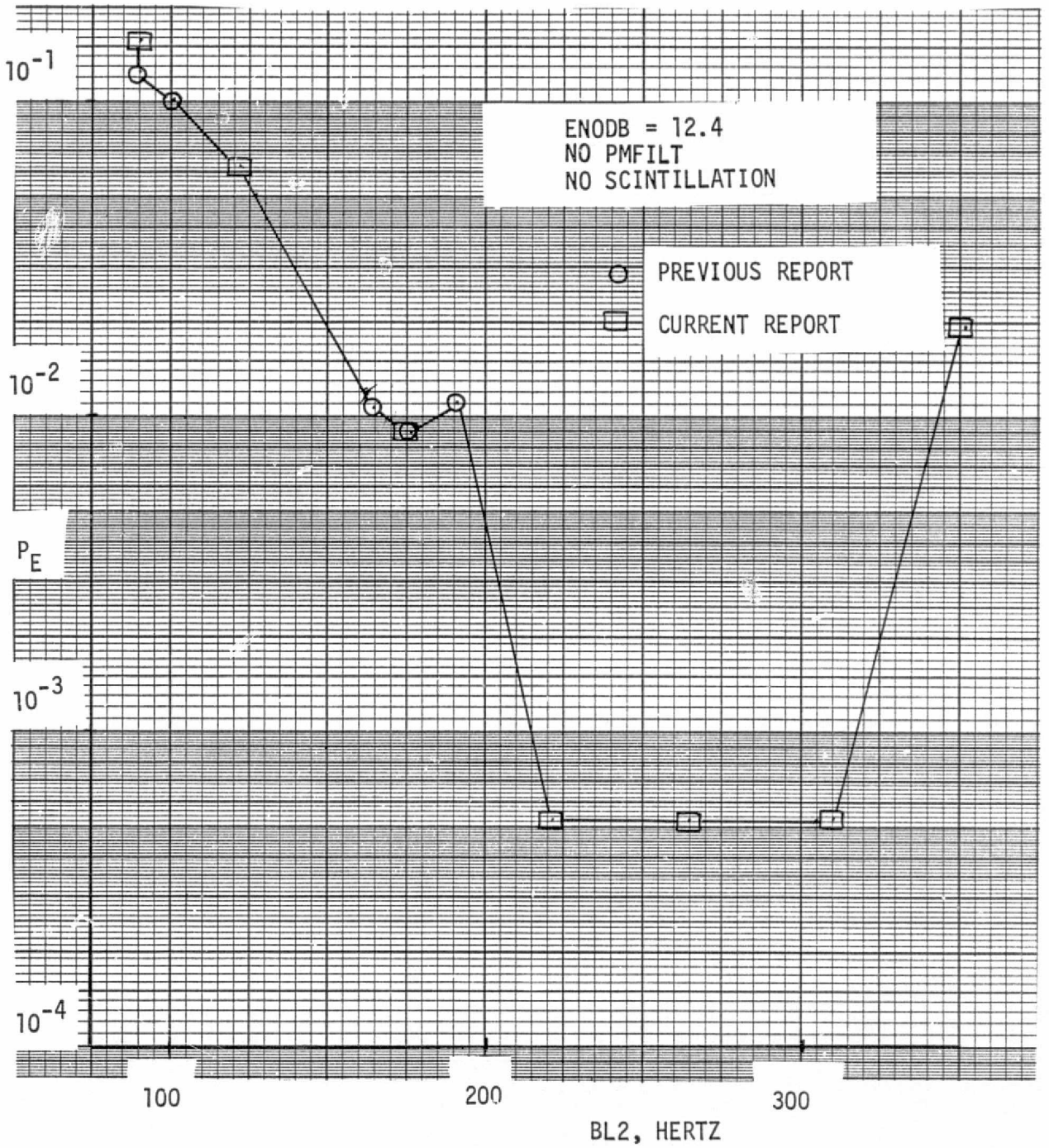

FIGURE 19

MEAN ERROR RATE VERSUS
LOOP BANDWIDTH PARAMETER
(NO PREMODULATION FILTER)

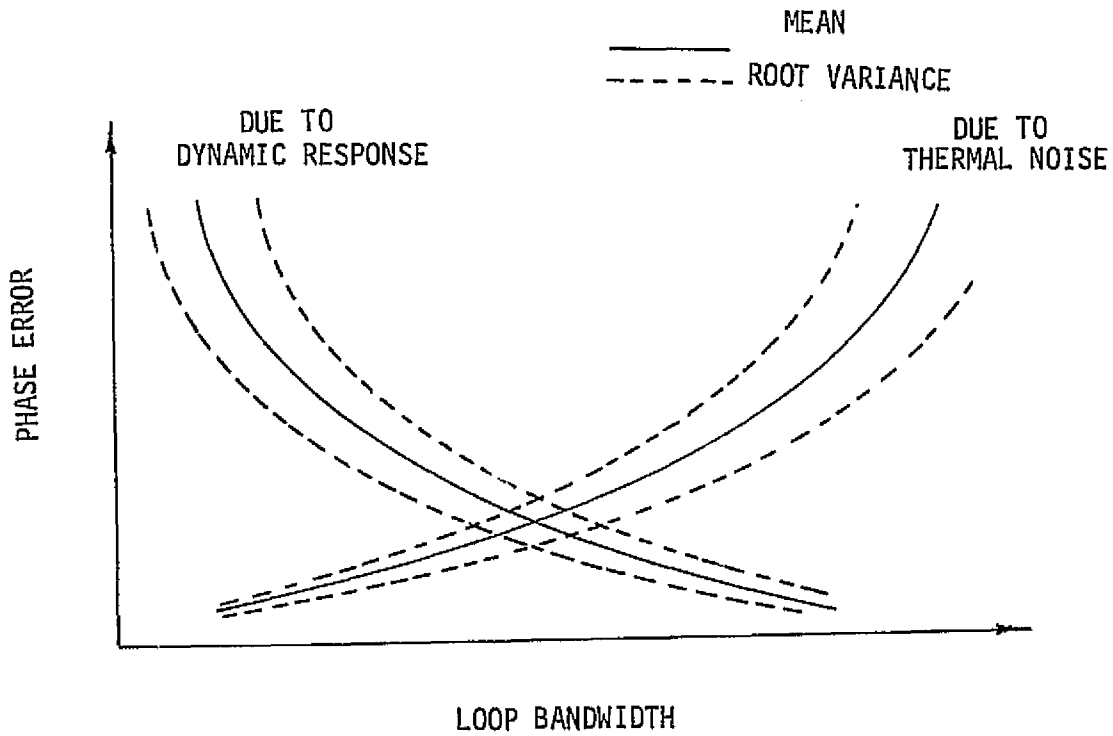

FIGURE 20

GENERIC EFFECT OF NOISE BANDWIDTH

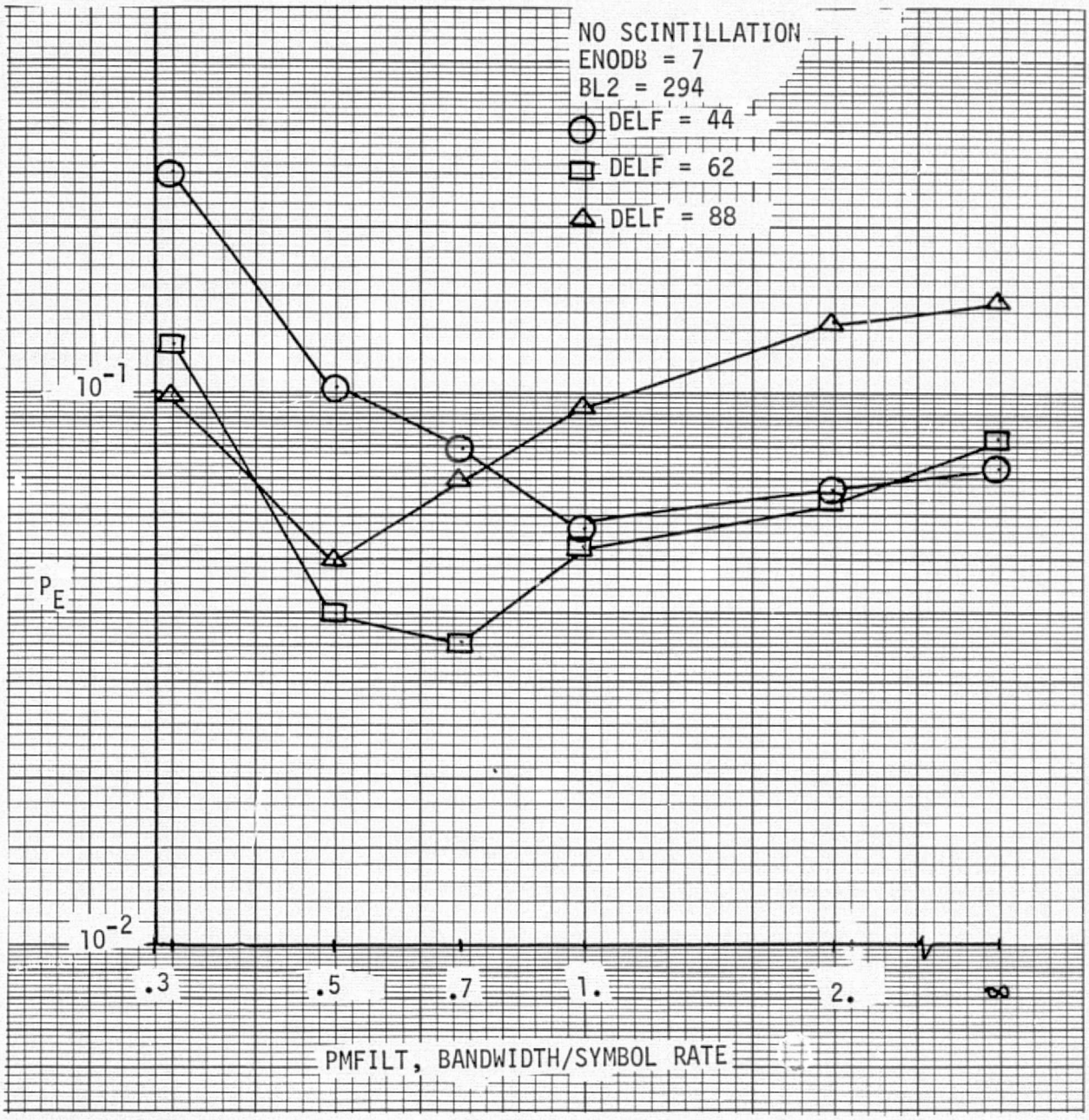

FIGURE 21

MEAN ERROR RATE VERSUS
PREMODULATION FILTER PARAMETERS

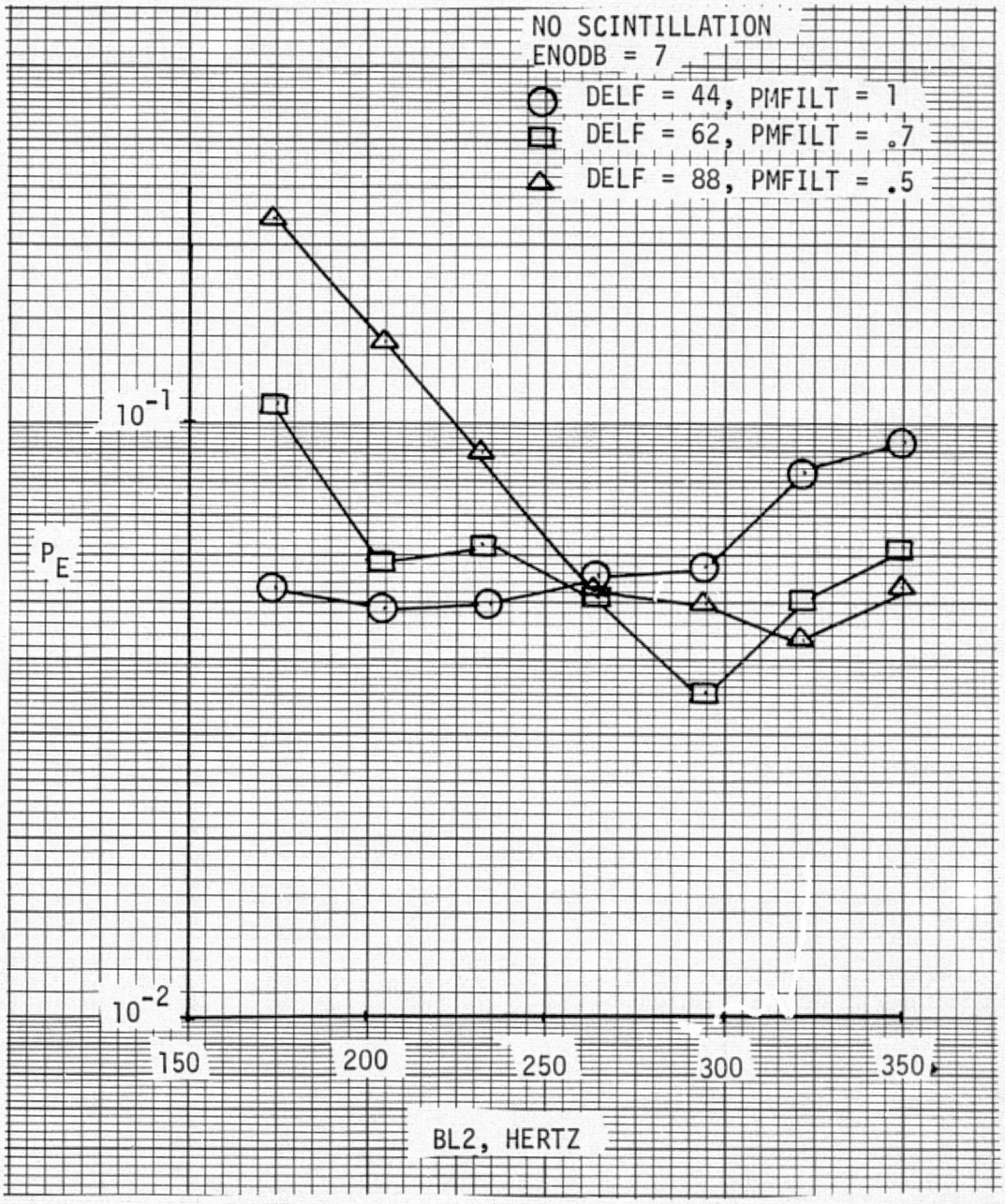

FIGURE 22

MEAN ERROR RATE VERSUS
DEVIATION AND LOOP BANDWIDTH

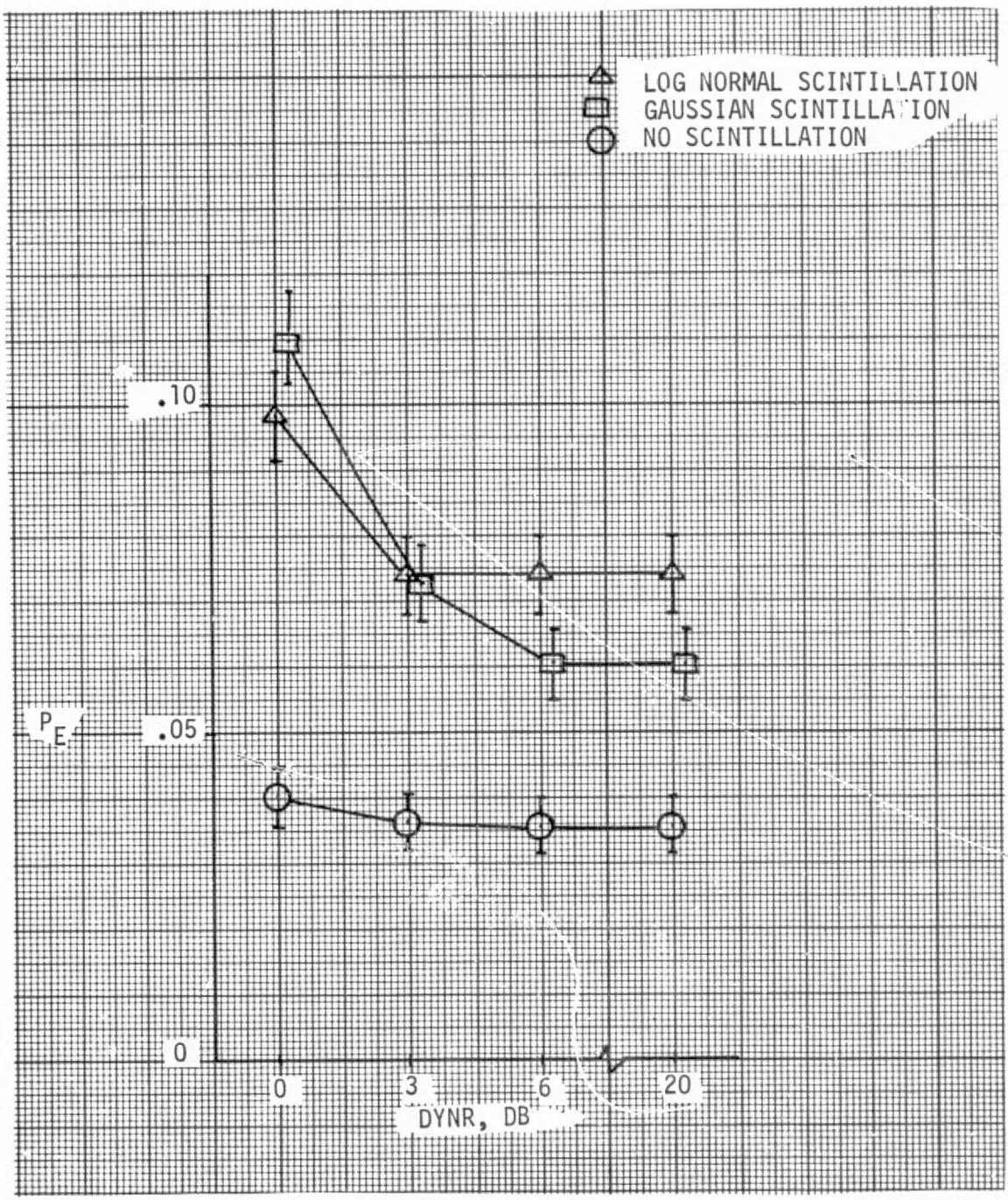

FIGURE 23
MEAN ERROR RATE VERSUS
DYNAMIC RANGE PARAMETER

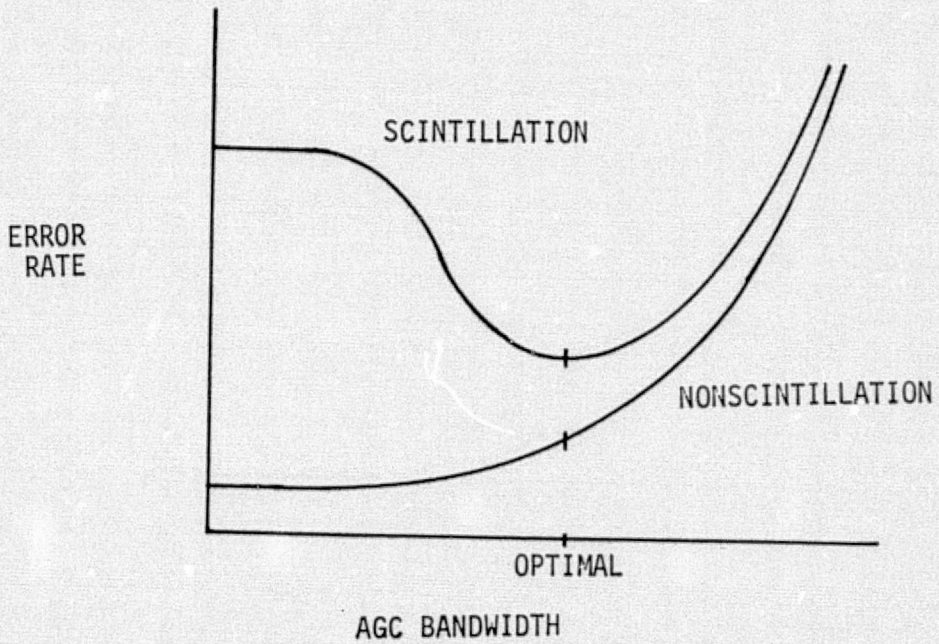

FIGURE 24
ANTICIPATED AGC PERFORMANCE

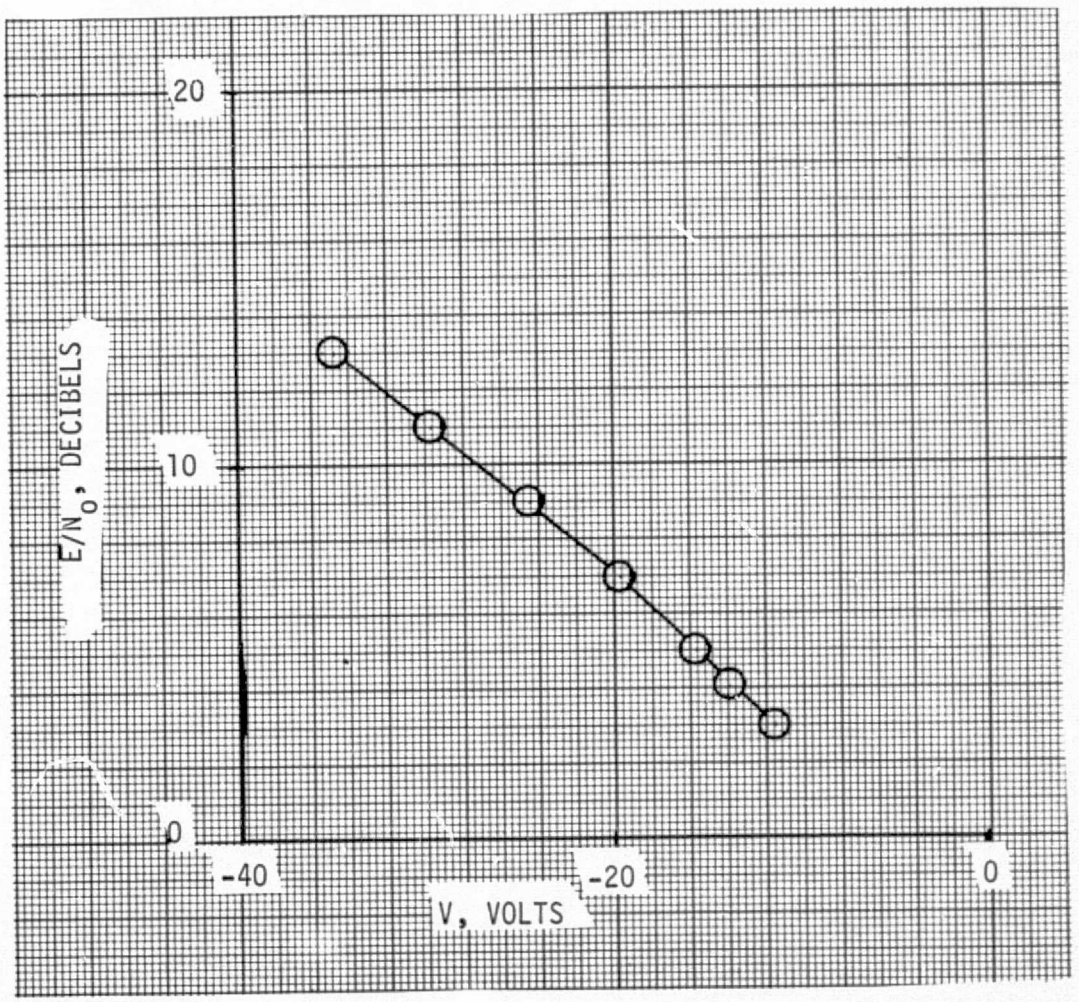

FIGURE 25
E/N$_o$ VERSUS AGC VOLTAGE

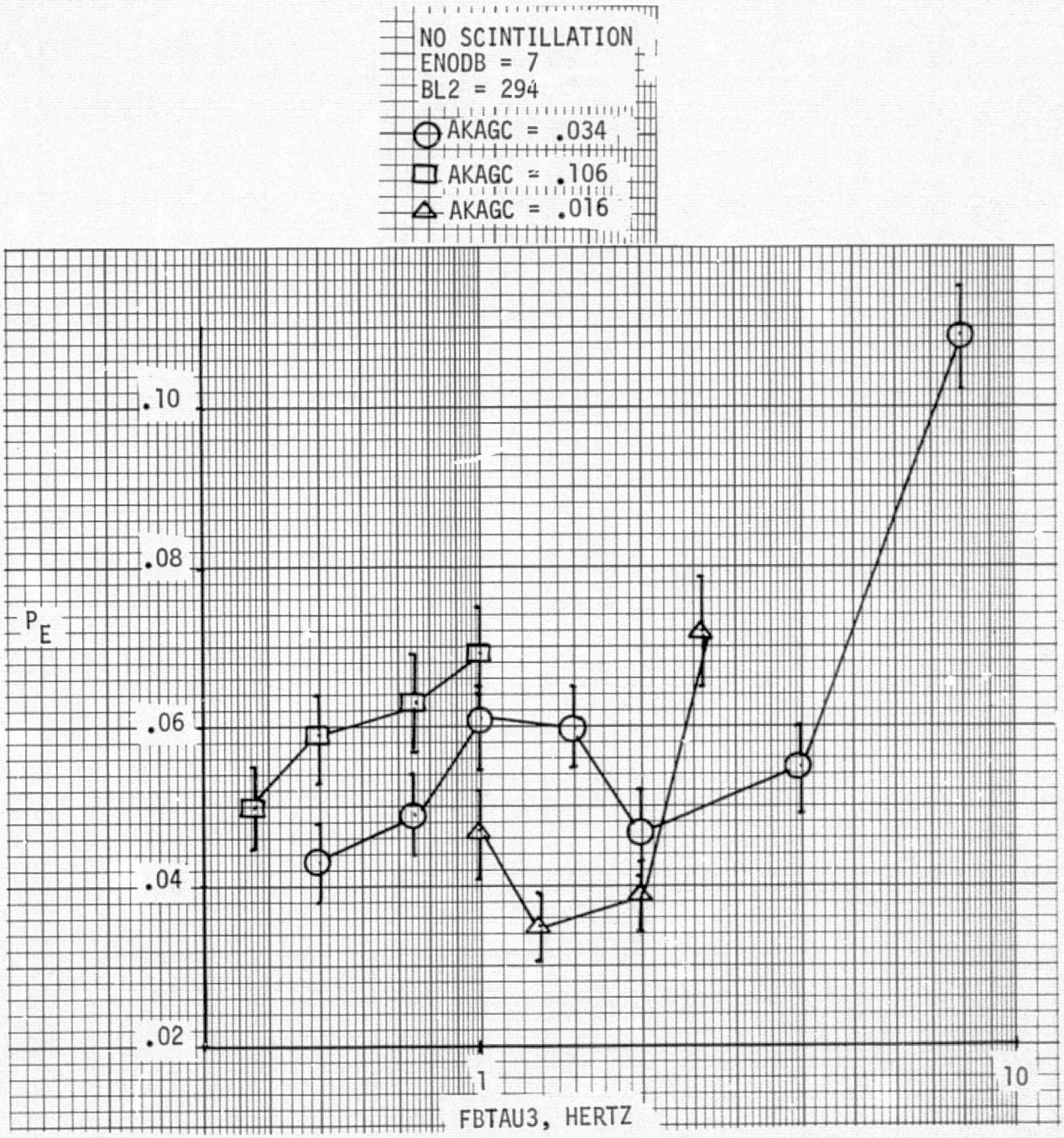

FIGURE 26a

MEAN ERROR RATE VERSUS
AGC PARAMETERS

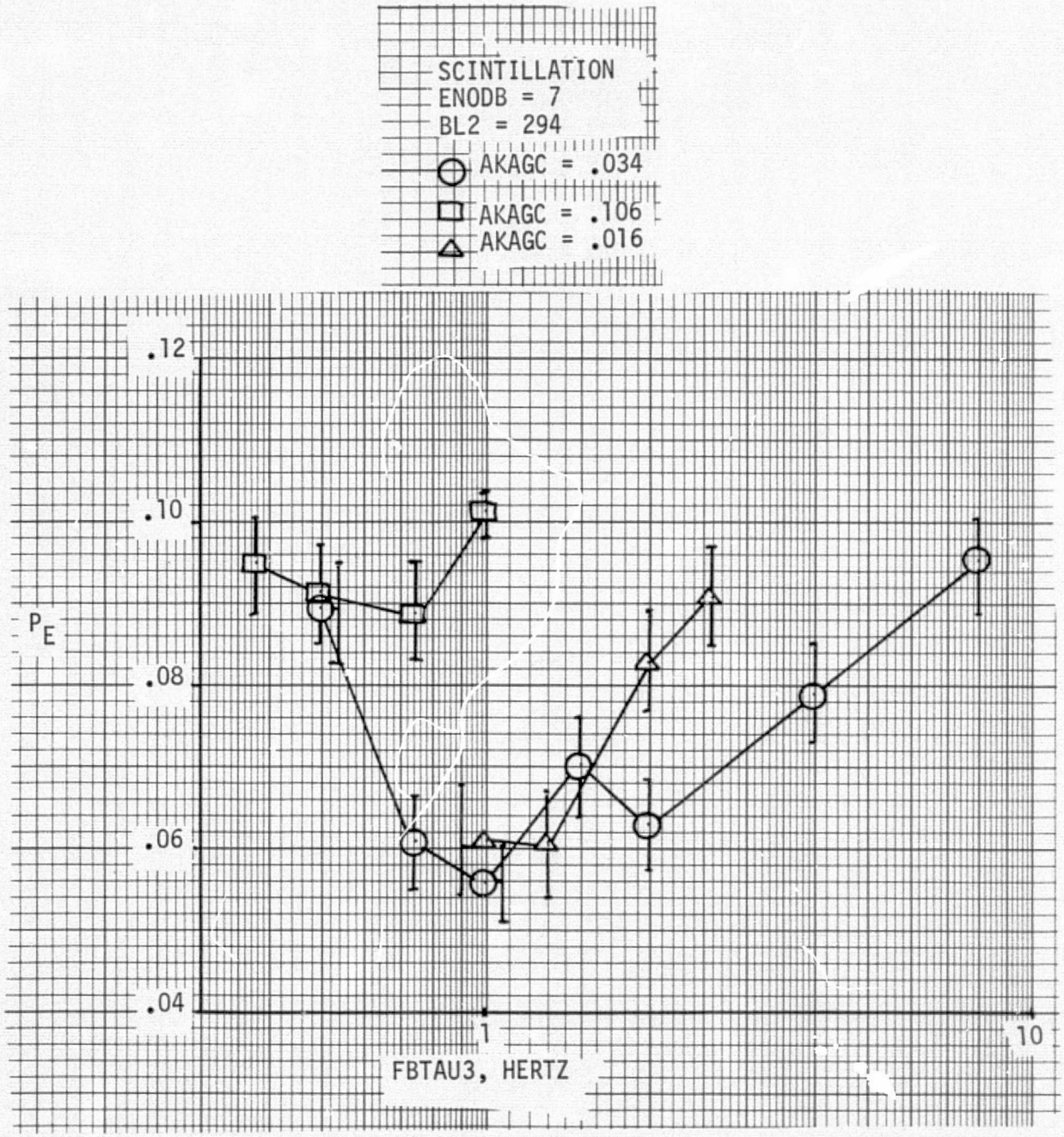

FIGURE 26b

MEAN ERROR RATE VERSUS
AGC PARAMETERS

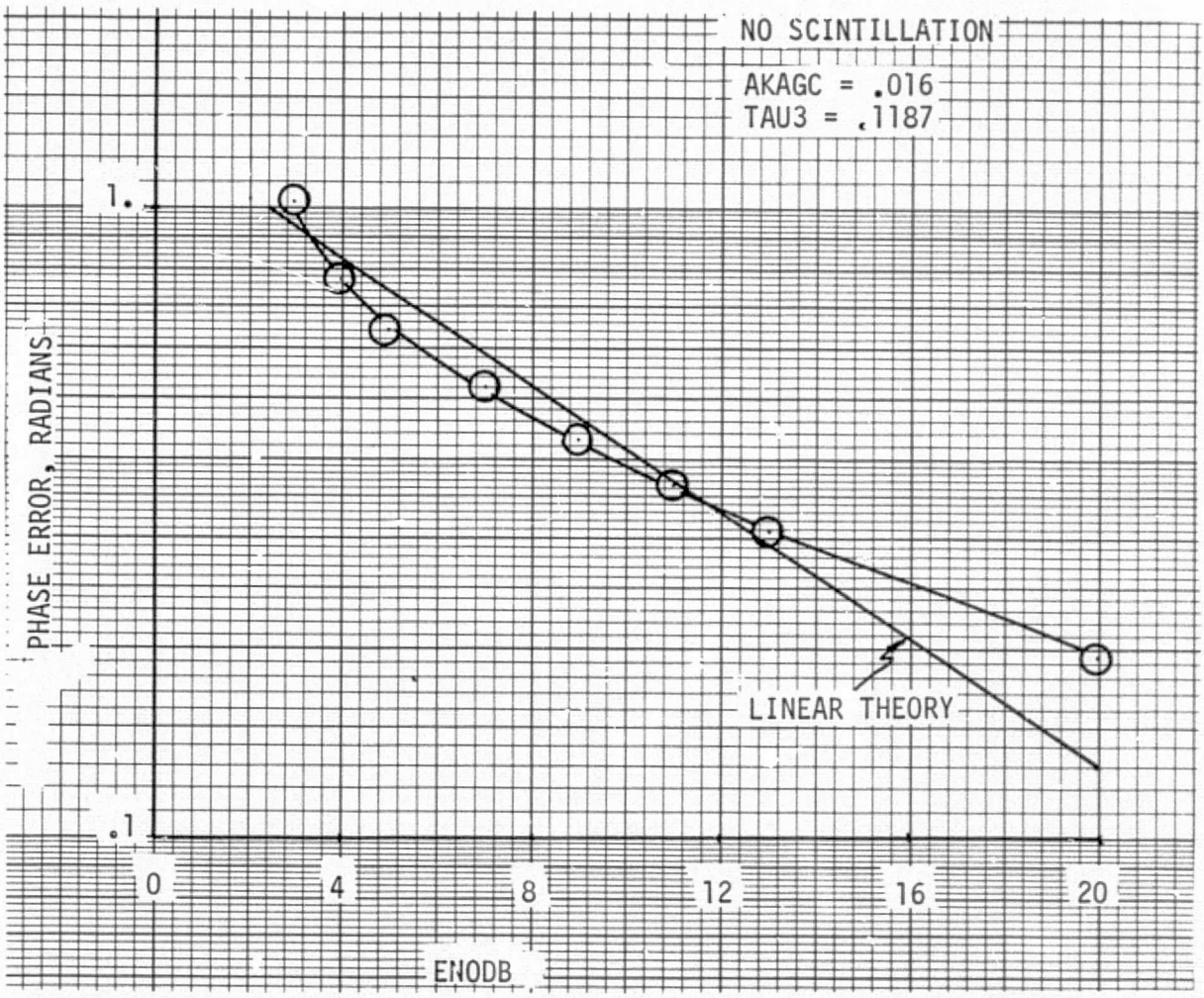

FIGURE 27
AFC LOOP PHASE ERROR VERSUS E/N_o

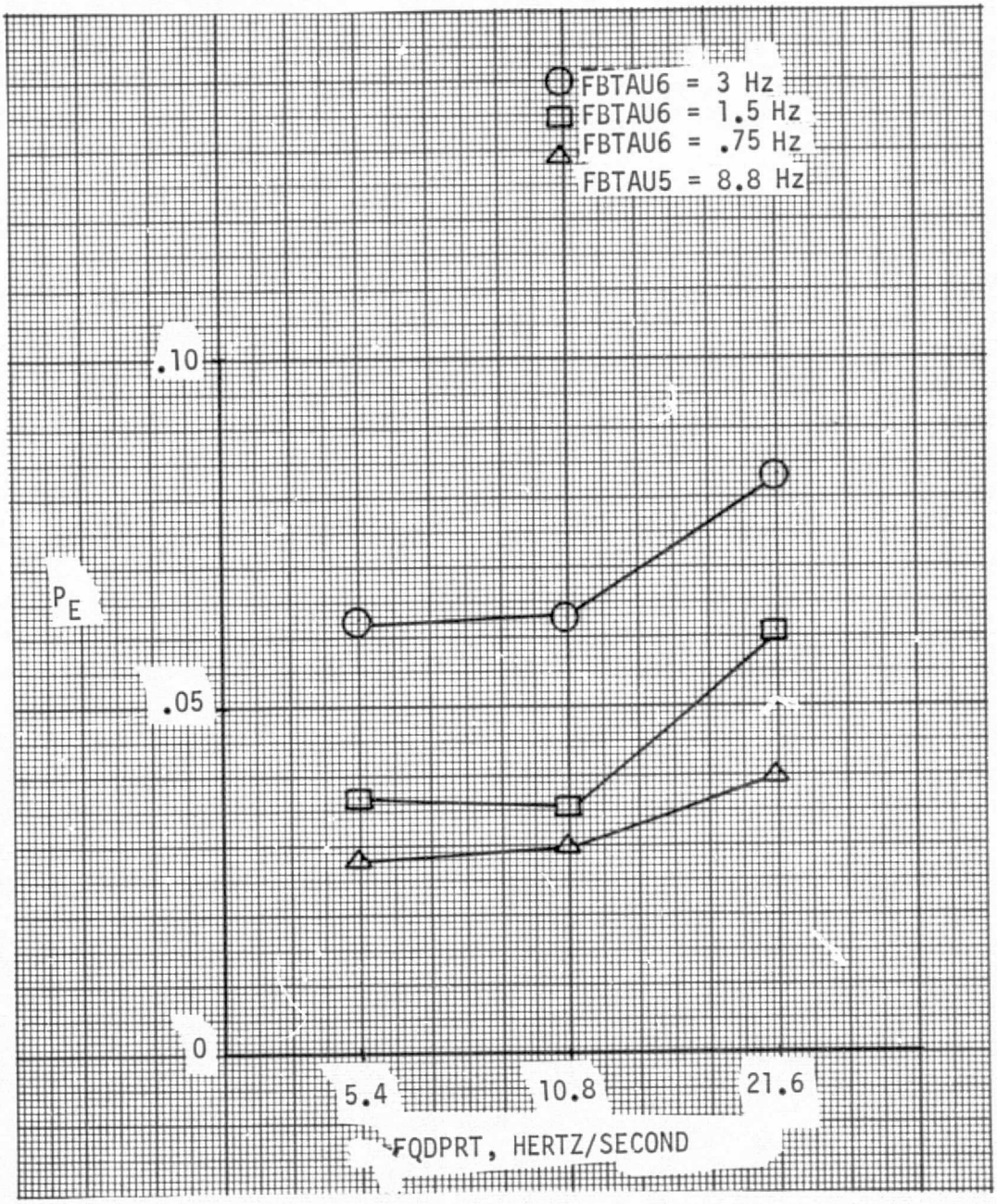

FIGURE 28

MEAN ERROR RATE VERSUS DOPPLER RATE
WITH PARAMETRIC DOPPLER FILTER BANDWIDTHS

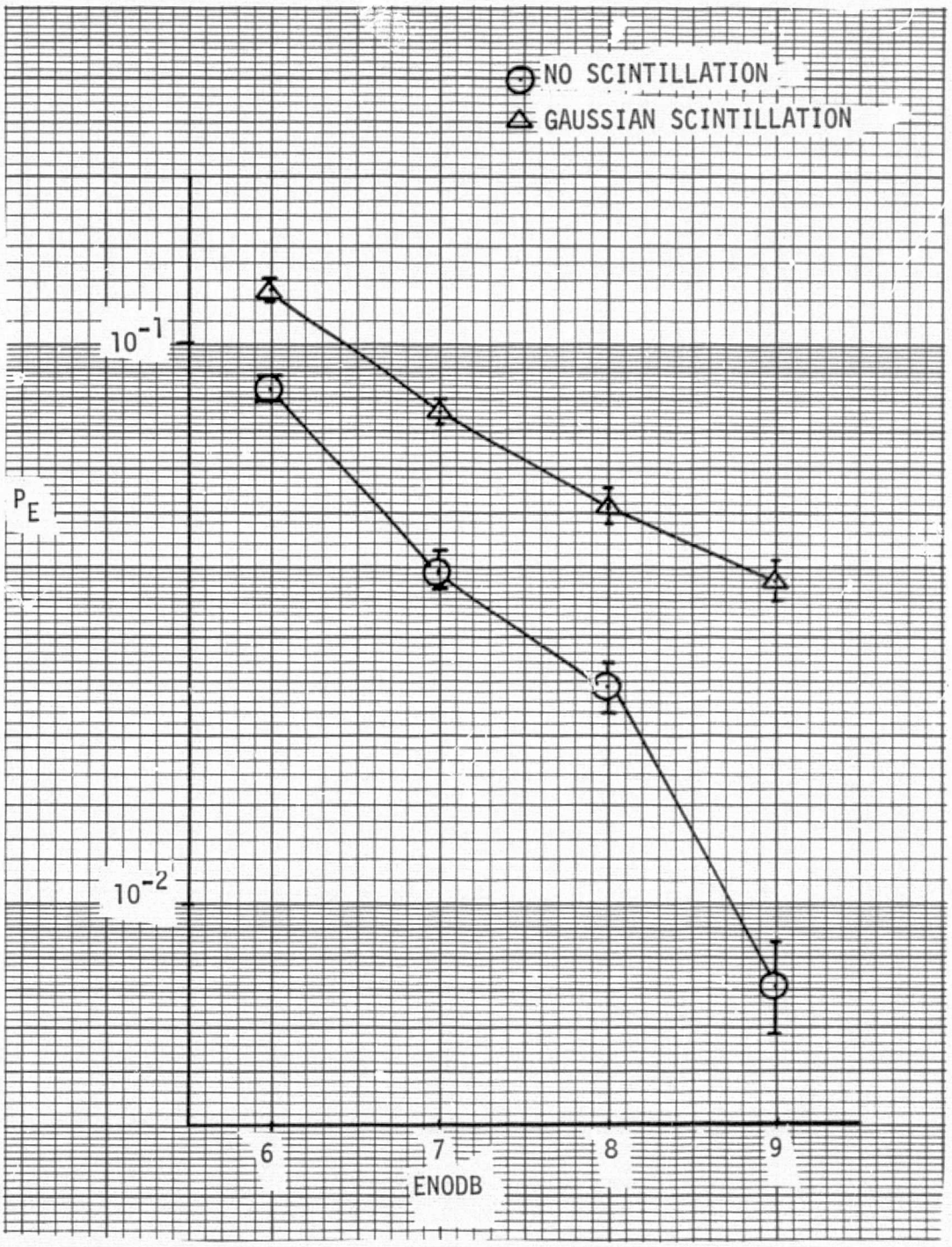

FIGURE 29

MEAN ERROR RATE PERFORMANCE
WITH OPTIMIZED MODEM

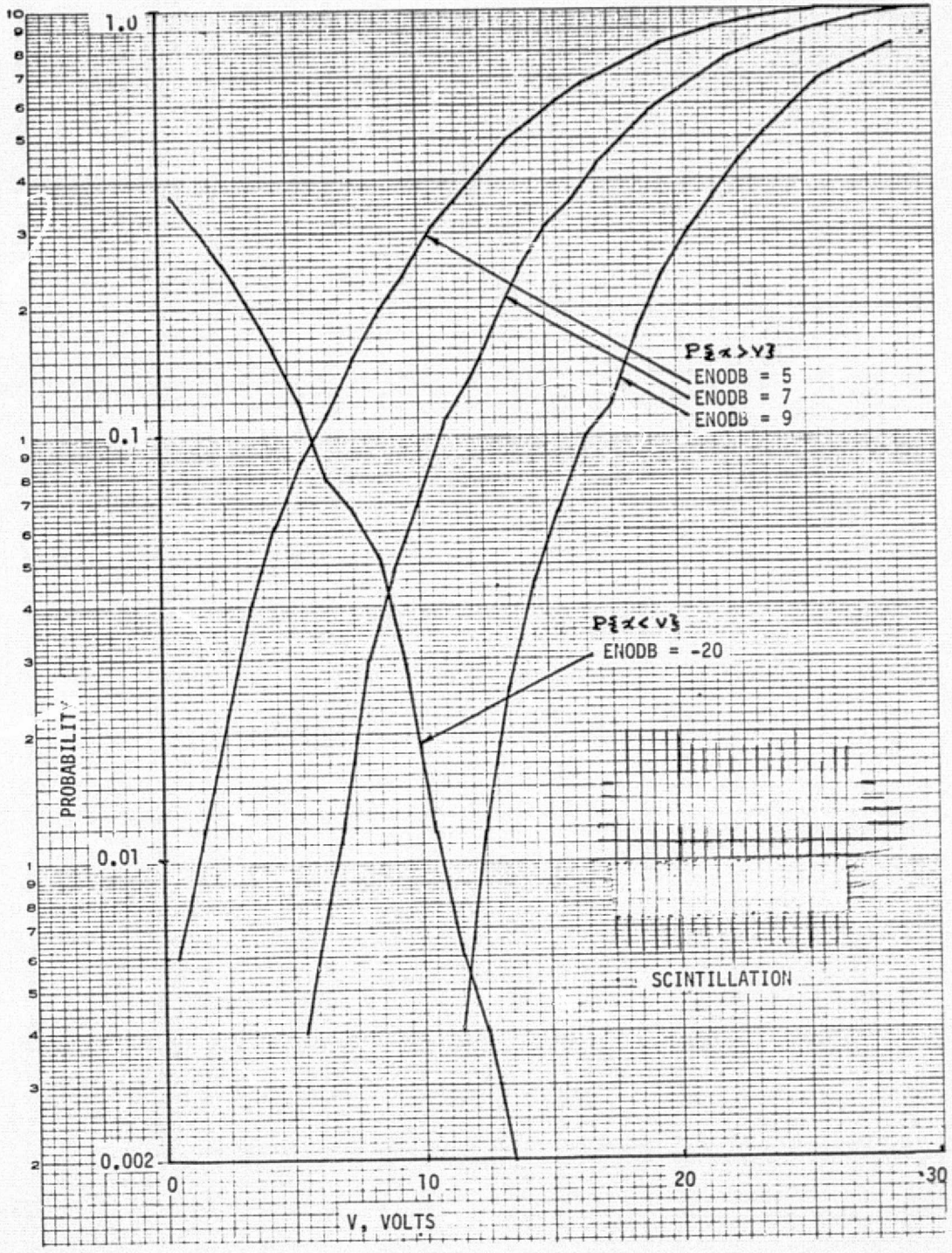

FIGURE 30

THE AGC VOLTAGE DISTRIBUTION

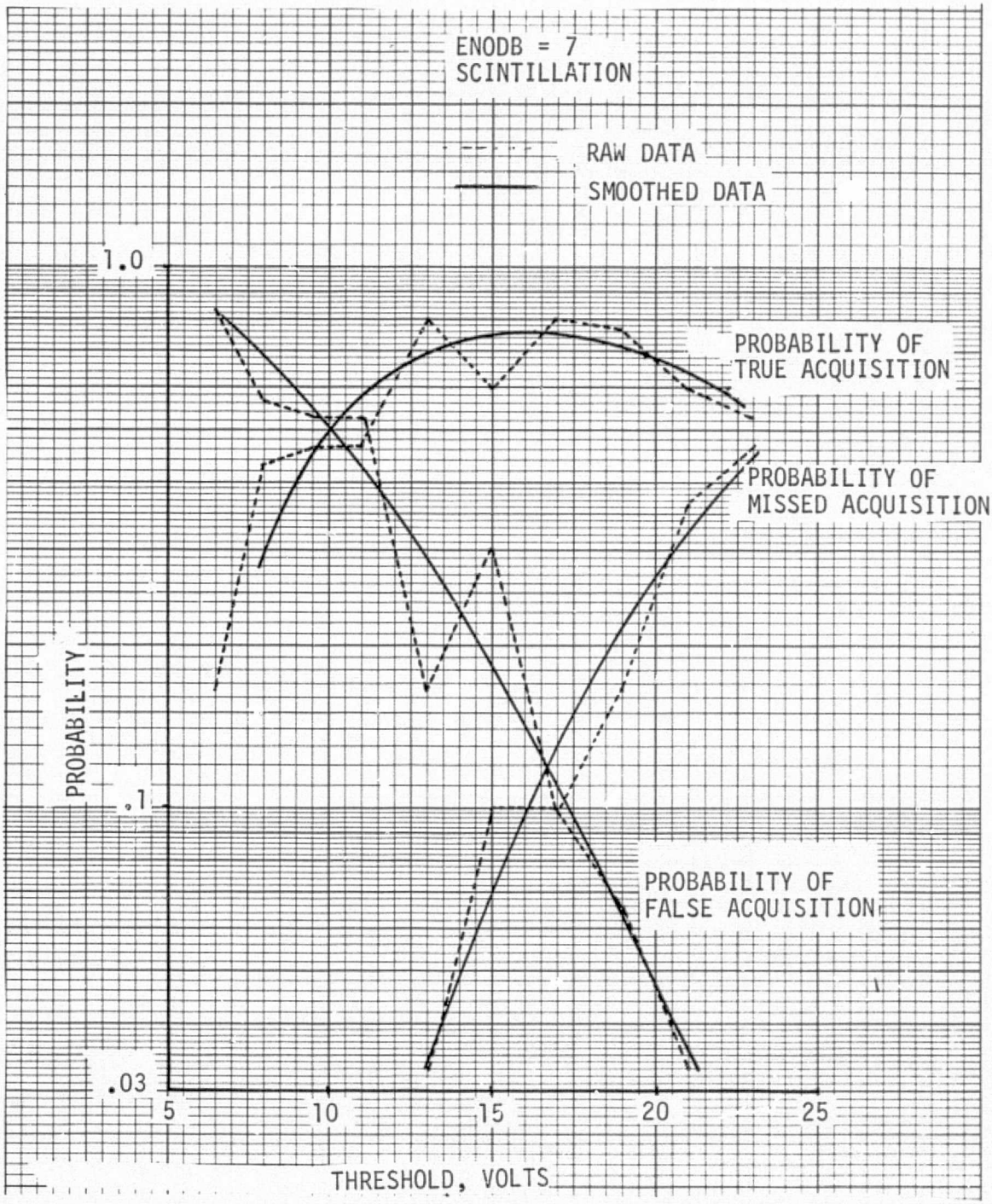

FIGURE 31

ACQUISITION PROBABILITY VERSUS
THRESHOLD VOLTAGE

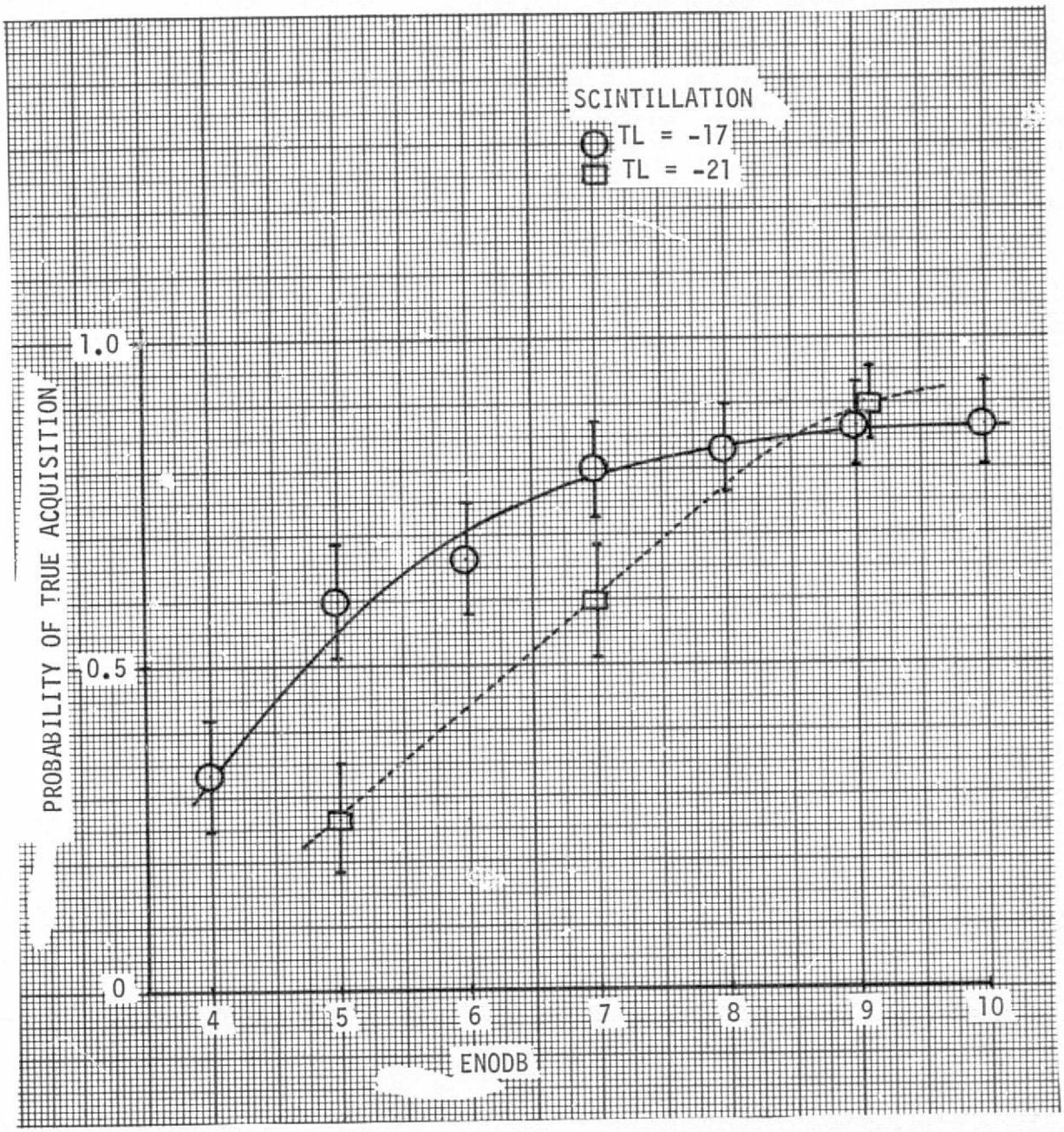

FIGURE 32

ACQUISITION PROBABILITY VERSUS
E/N_o WITH PARAMETRIC THRESHOLD VOLTAGES

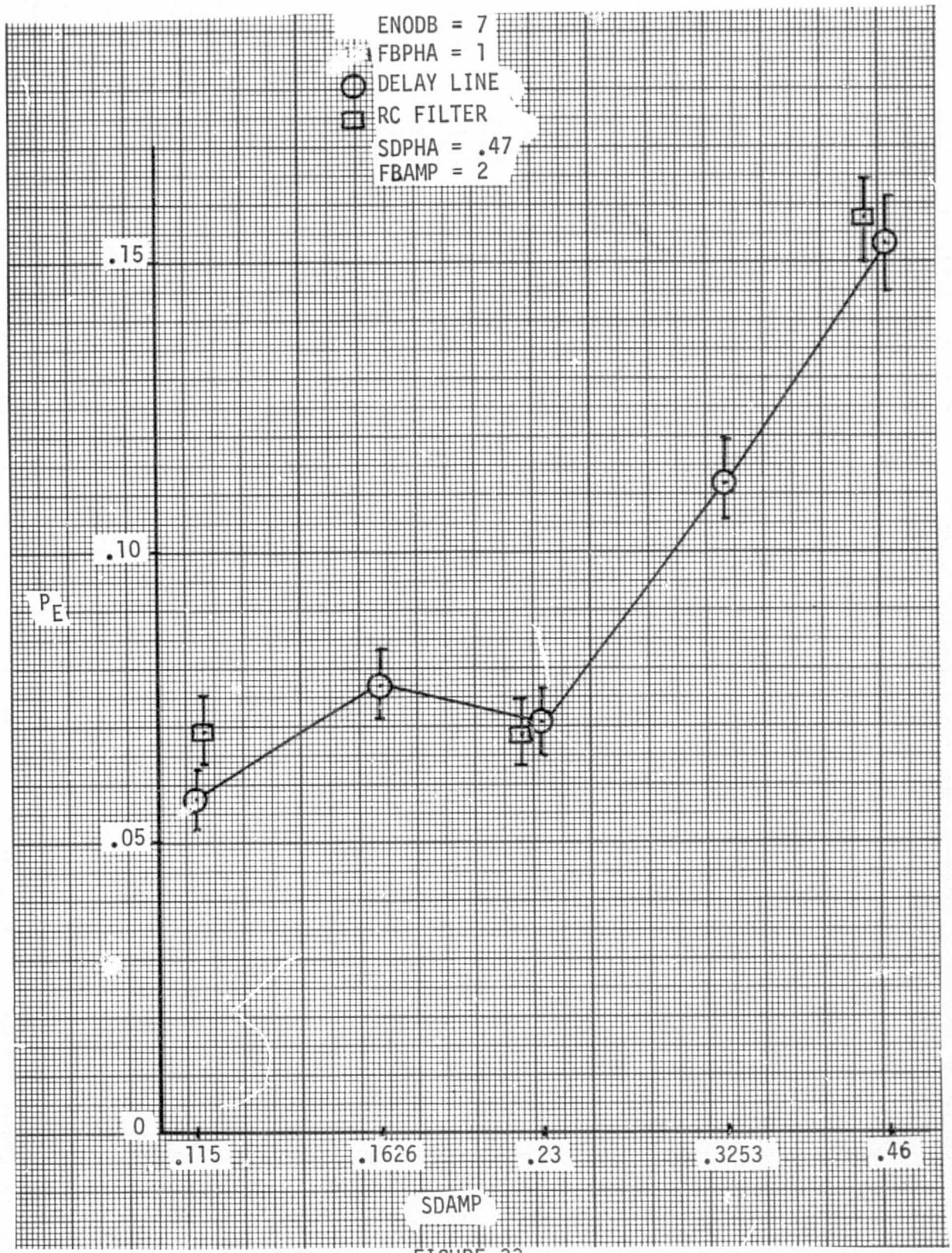

FIGURE 33

AMPLITUDE SCINTILLATION MAGNITUDE EFFECTS
ON MEAN ERROR RATE

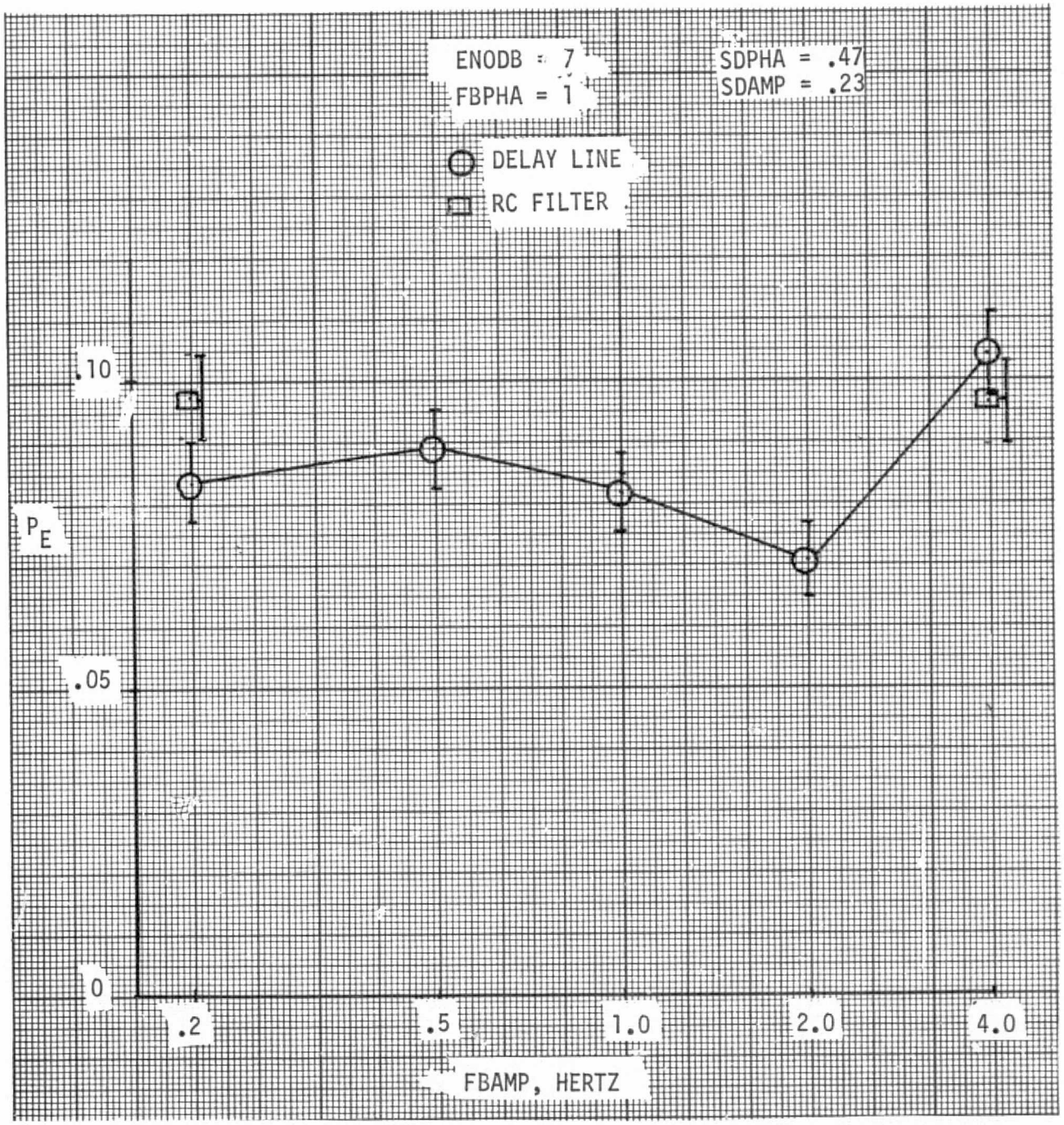

FIGURE 34

AMPLITUDE SCINTILLATION BANDWIDTH EFFECTS
ON MEAN ERROR RATE

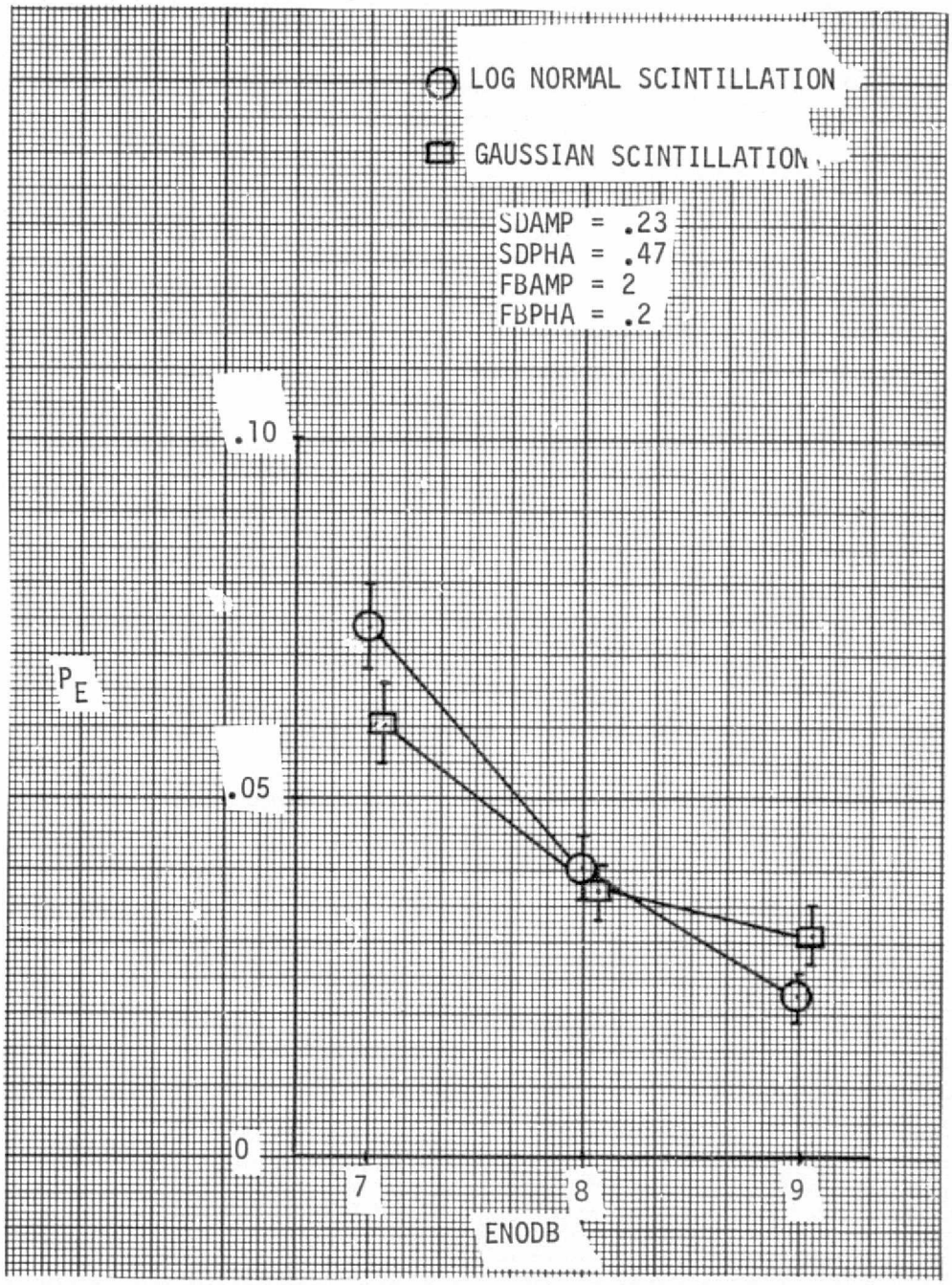

FIGURE 35

COMPARISON OF TYPES OF SCINTILLATION

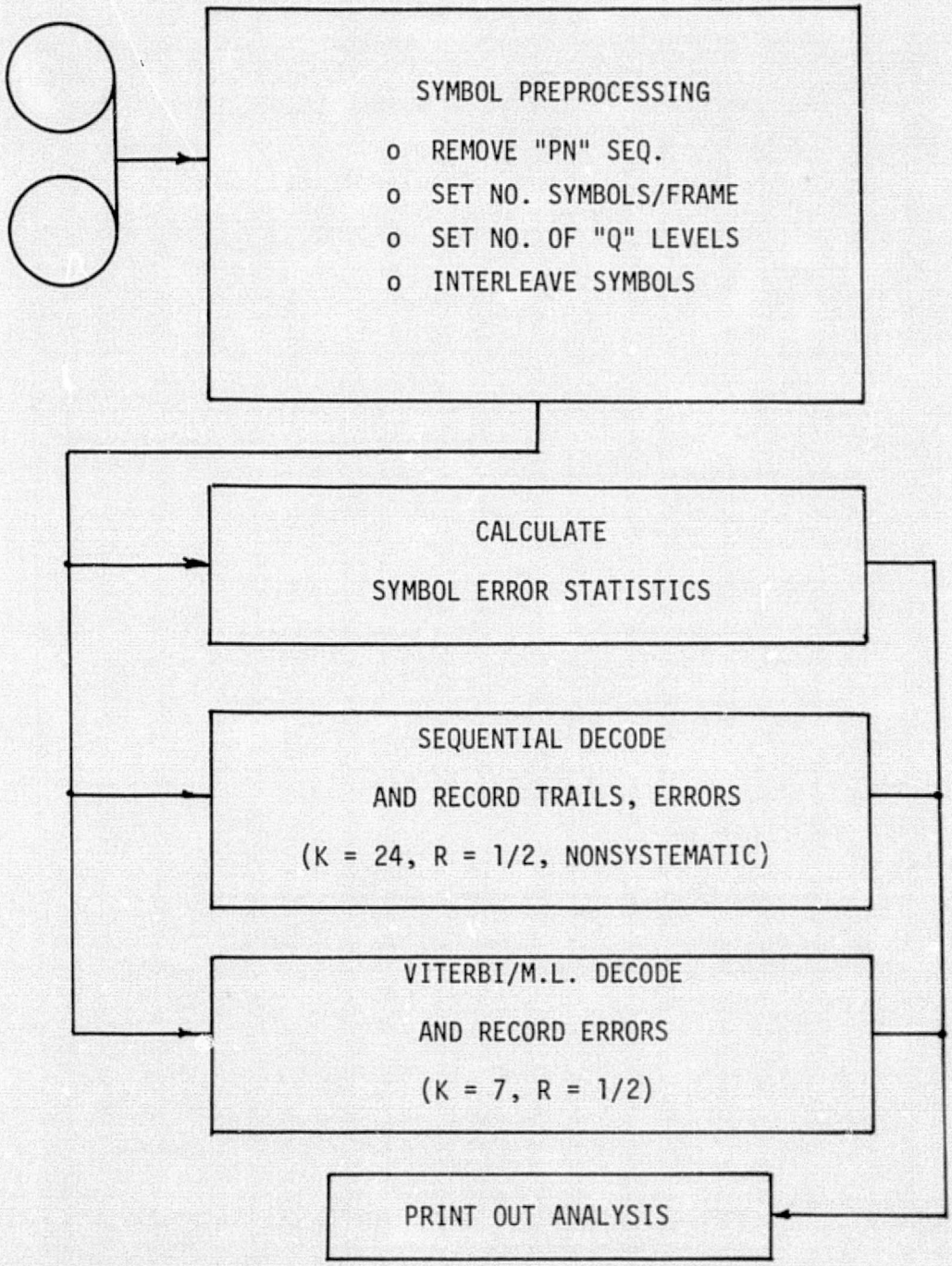

FIGURE 36
DECODING SIMULATION

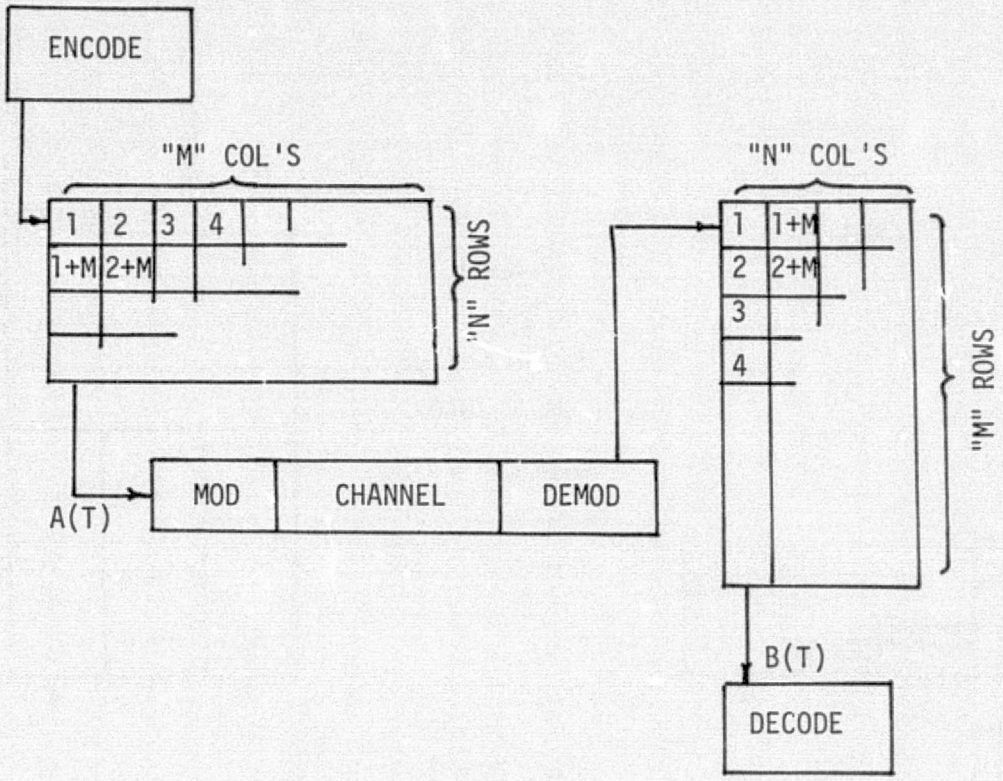

TIME SEQ. A(T): 2, ... 1 + 2M, 1 + M, 1

B(T): 1 + M, ... 3, 2, 1

FIGURE 37

INTERLEAVING DEFINITION

M * N $\leq$ 1 FRAME (504 OR 1008 SYMBOLS)

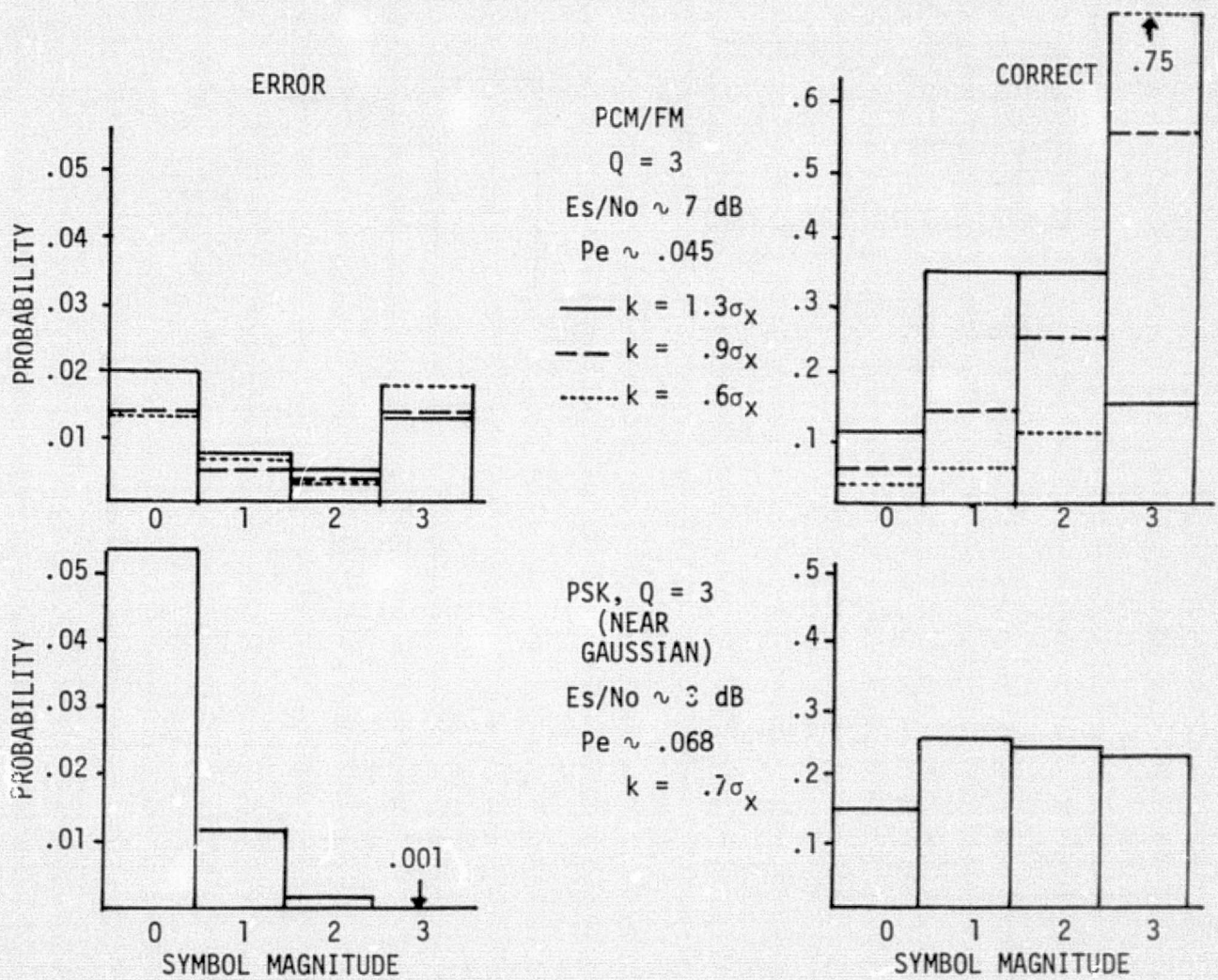

FIGURE 38

TYPICAL PCM/FM VS PSK SYMBOL TRANSITION PROBABILITIES

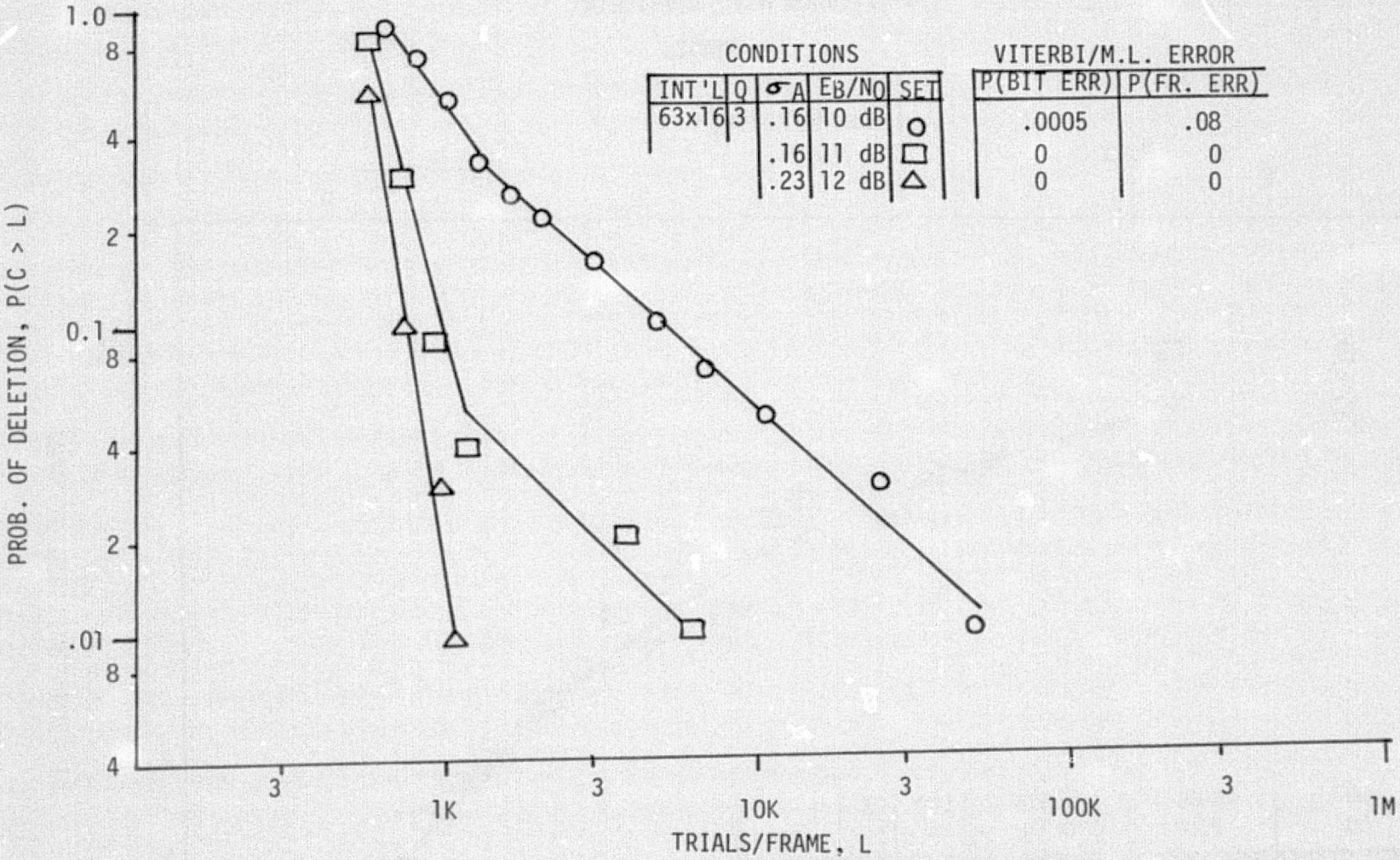

FIGURE 39

DECODING PERFORMANCE VS E_B/N_0

PROBABILITY OF DELETION VS TRIALS/FRAME

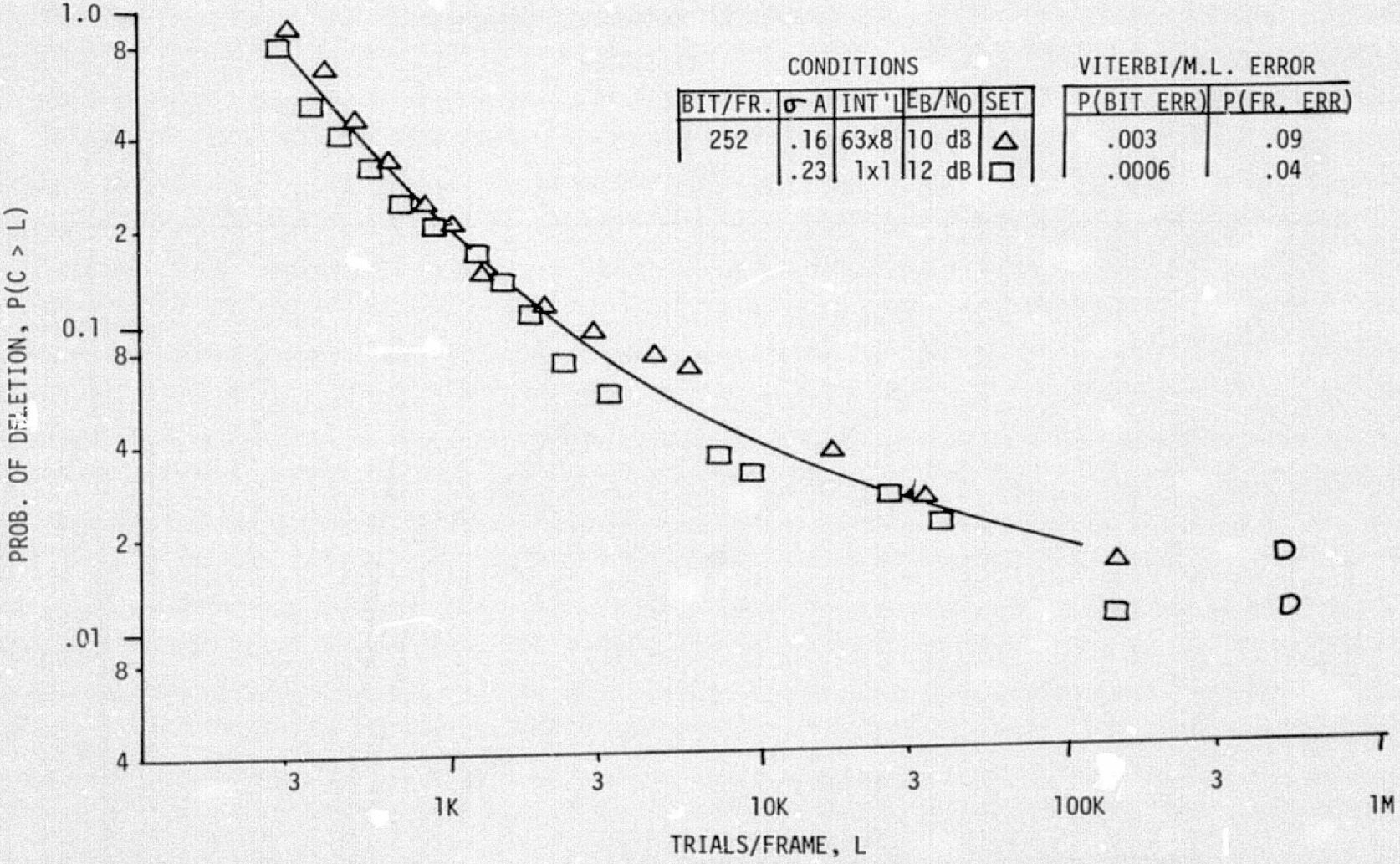

FIGURE 40

INTERLEAVE GAIN COMPARISON

PROBABILITY OF DELETION VS TRIALS/FRAME

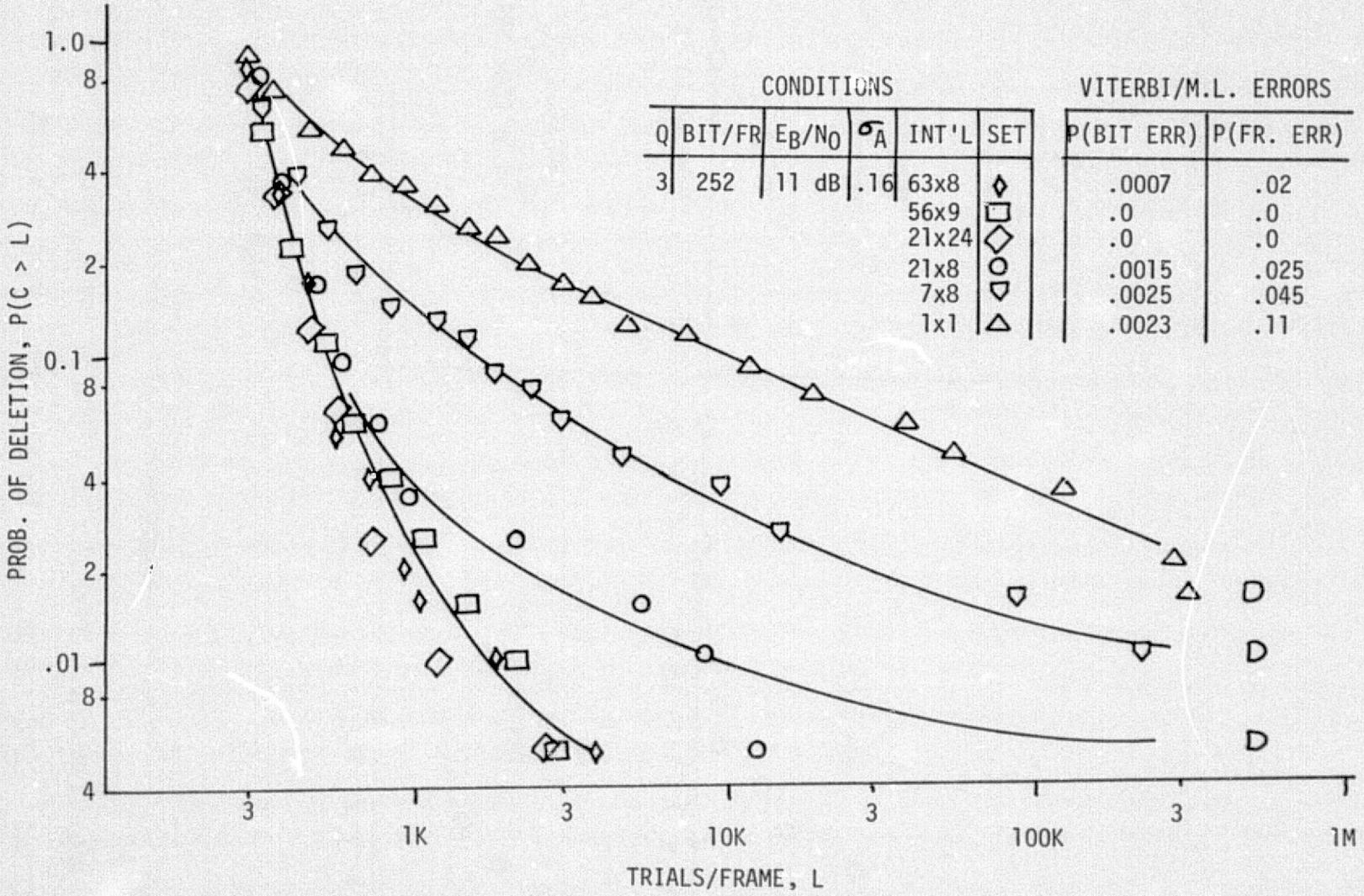

FIGURE 41

THE EFFECT OF INTERLEAVER SIZE ON DECODING PERFORMANCE

PROBABILITY OF DELETION VS TRIALS/FRAME

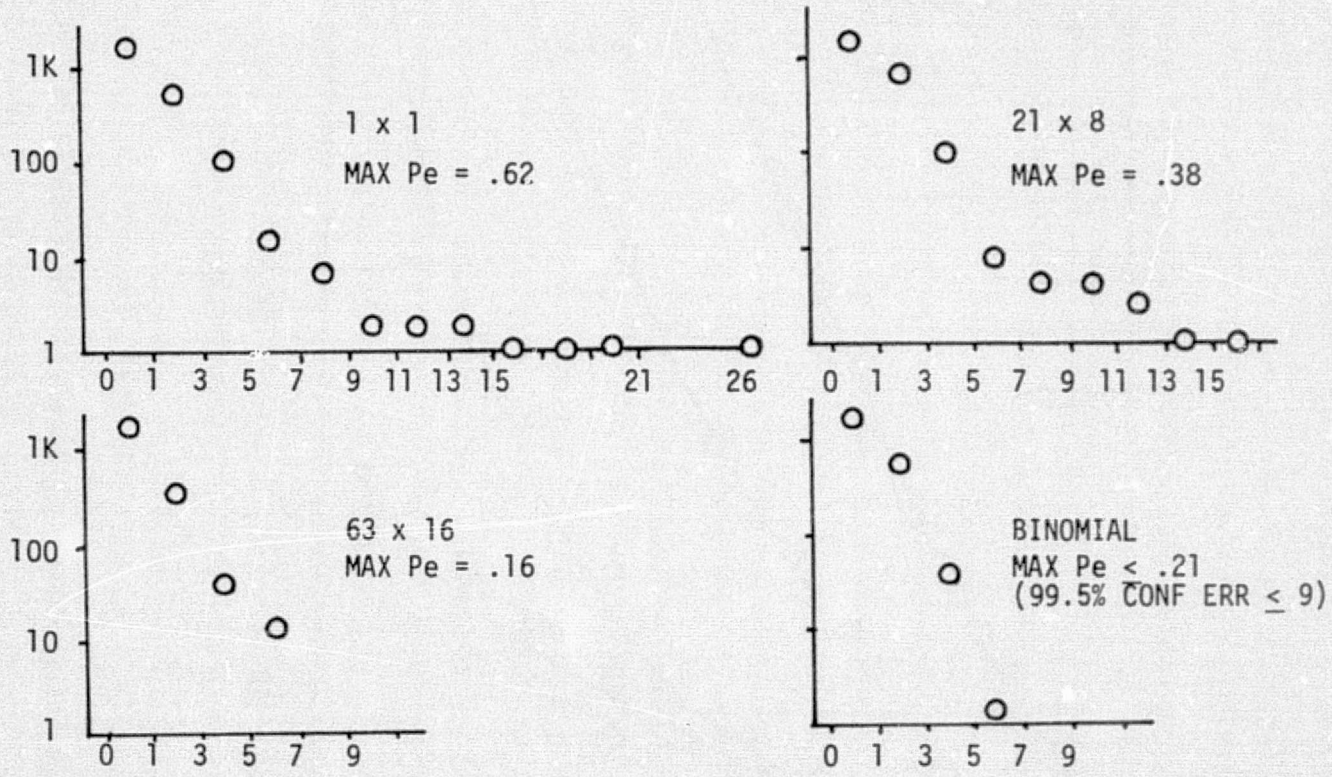

FIGURE 42

FIGURE 42

GROUP ERROR HISTOGRAMS AND THE EFFECT OF INTERLEAVING

CONDITIONS: E_S/N_O = 8 dB, σ_A = .16, 42 SYMBOLS, MEAN Pe = .025

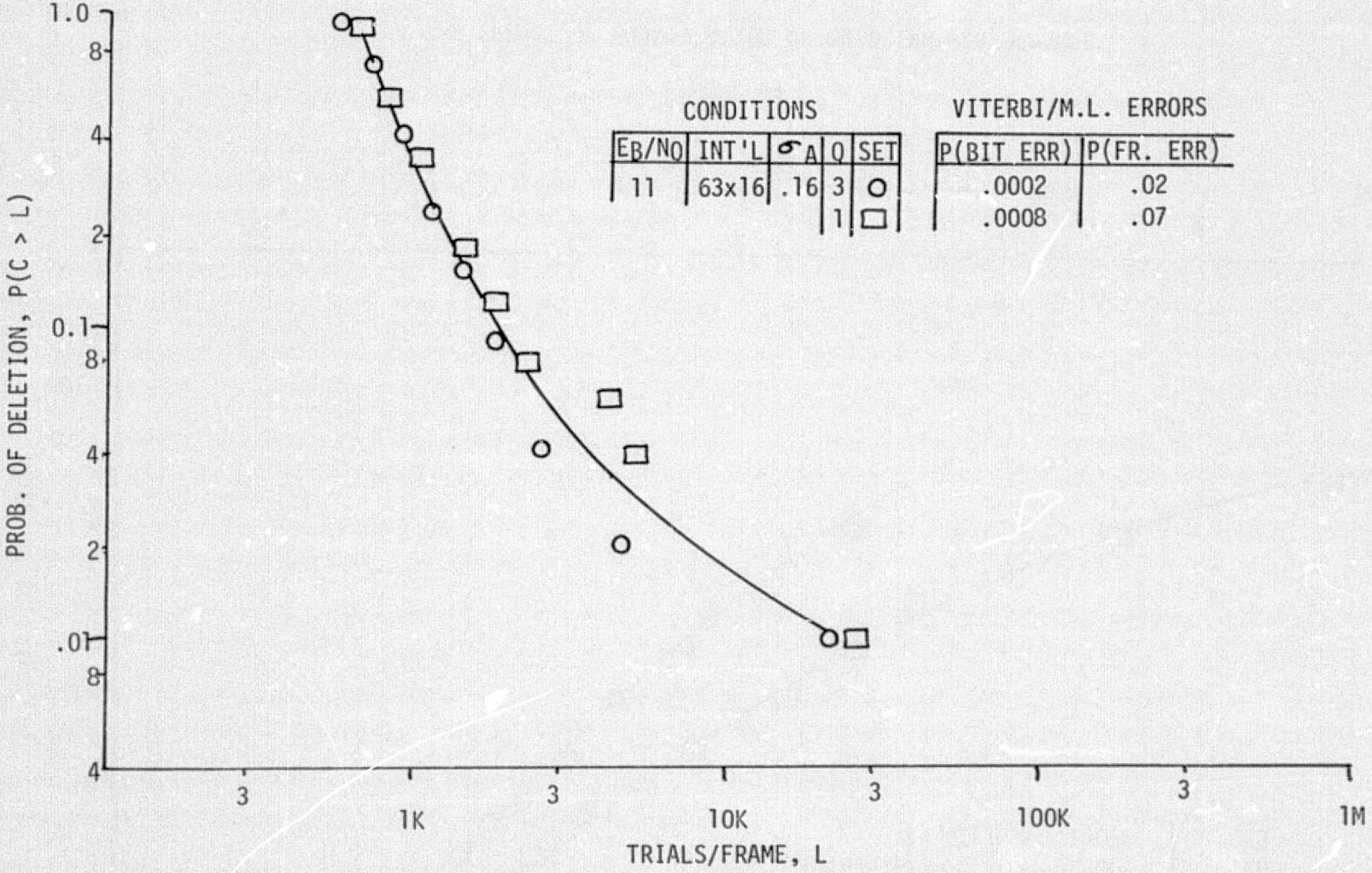

FIGURE 43

THE EFFECT OF QUANTIZATION ON DECODING PERFORMANCE

PROBABILITY OF DELETION VS TRIALS/FRAME

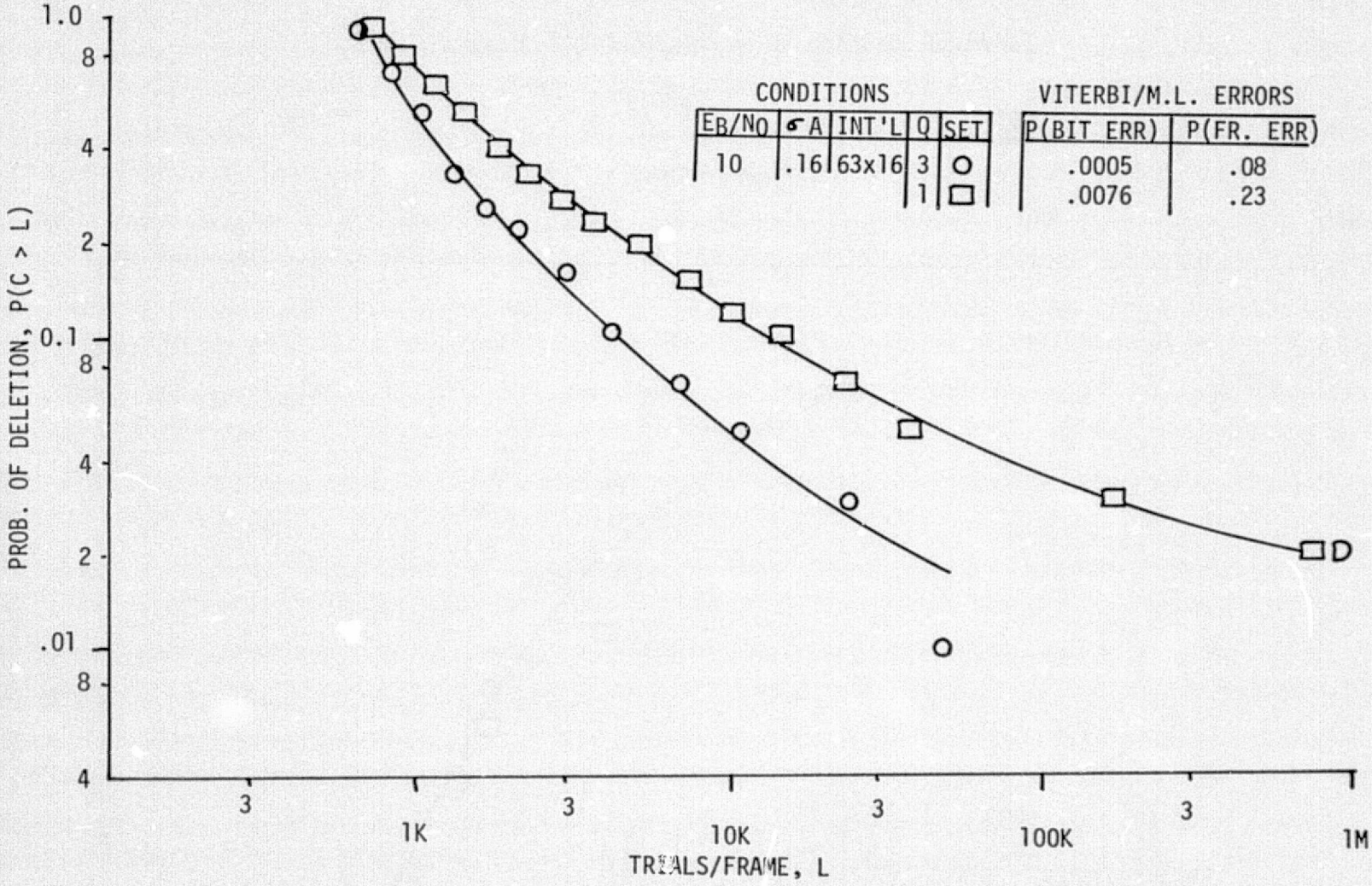

FIGURE 44

THE EFFECT OF QUANTIZATION ON DECODING PERFORMANCE

PROBABILITY OF DELETION VS TRIALS/FRAME

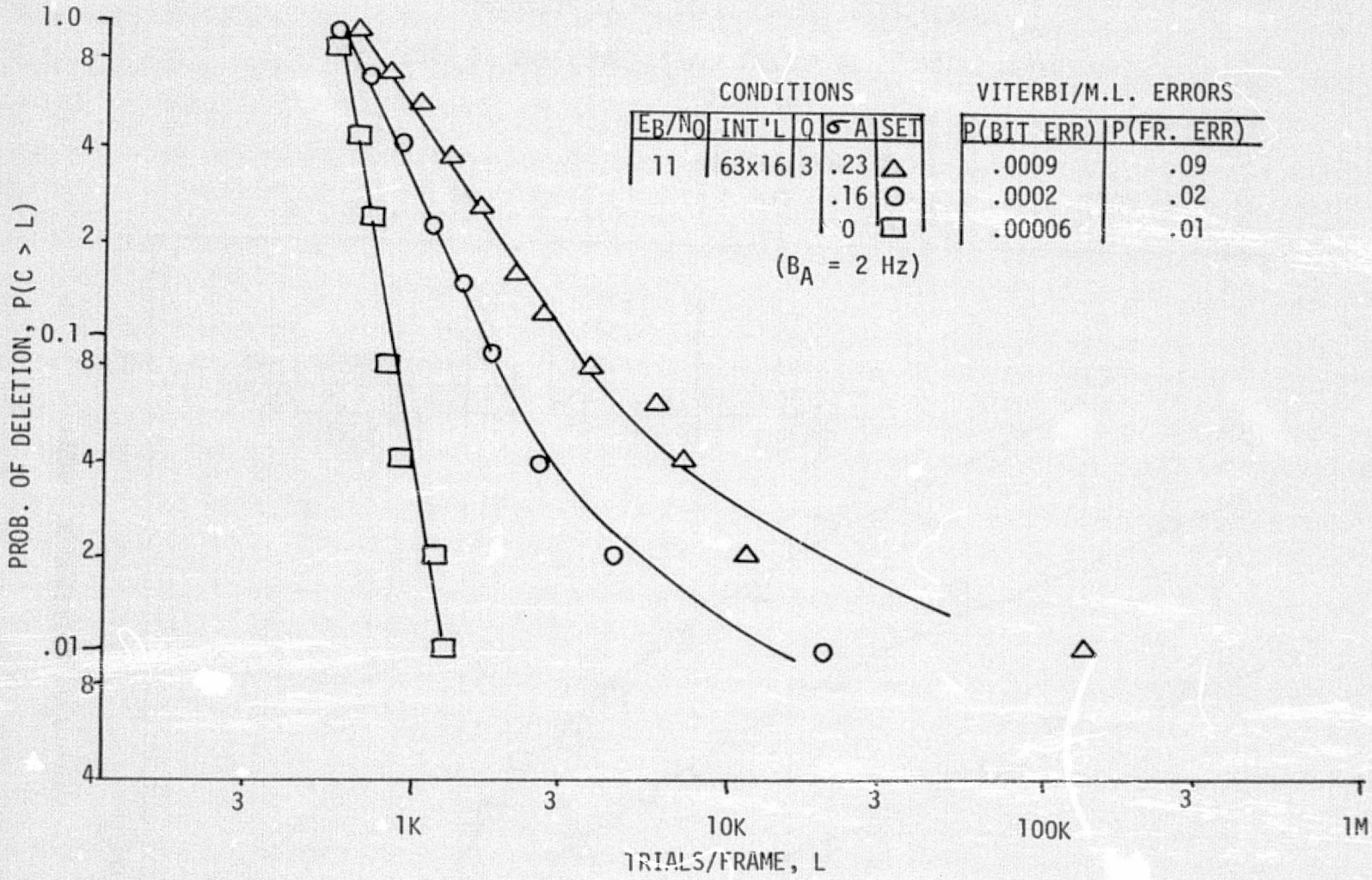

FIGURE 45

THE EFFECT OF AMPLITUDE SCINTILLATION ON DECODING PERFORMANCE
PROBABILITY OF DELETION VS TRIALS/FRAME

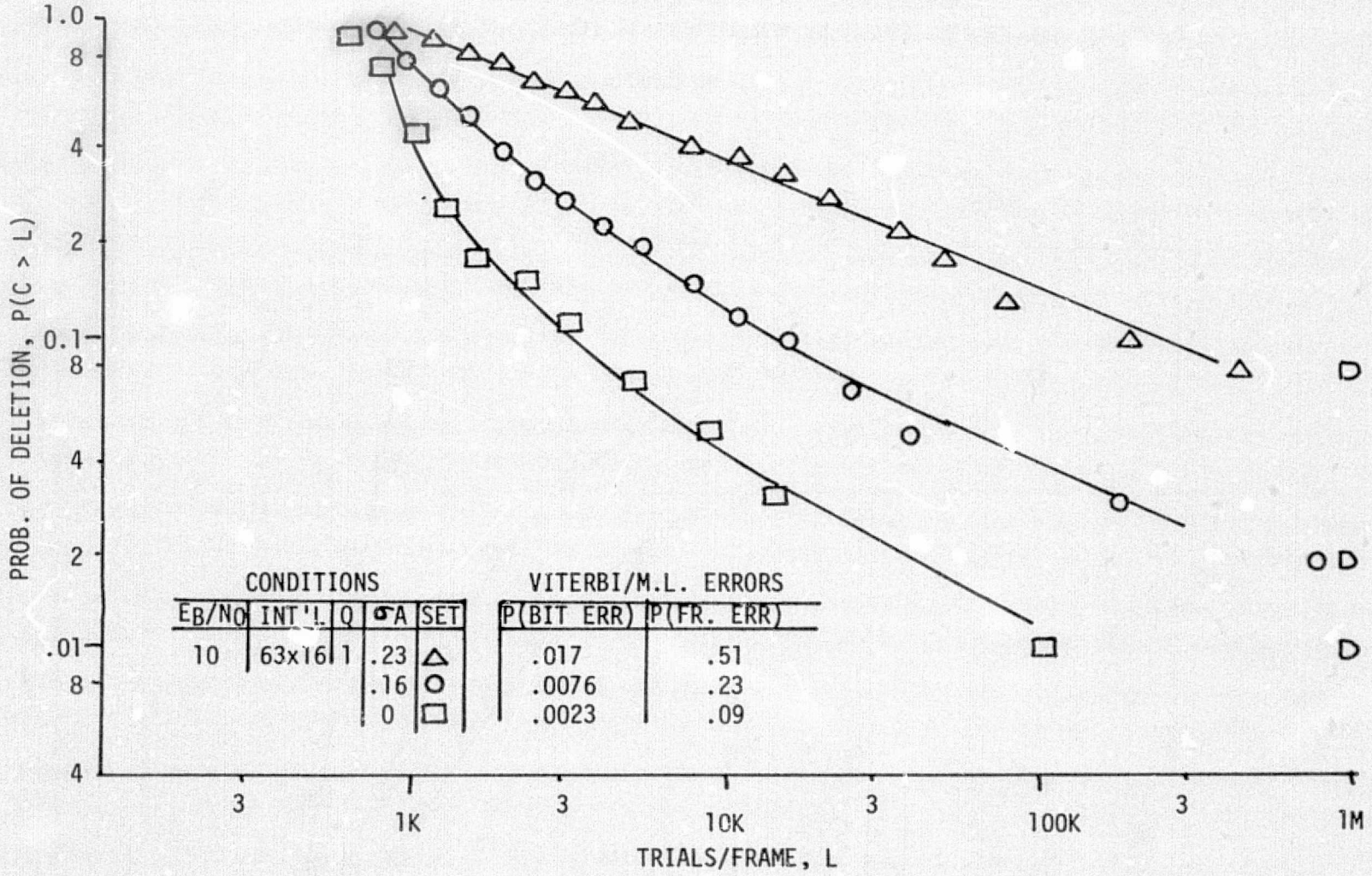

FIGURE 46

THE EFFECT OF AMPLITUDE SCINTILLATION ON DECODING PERFORMANCE

PROBABILITY OF DELETION VS TRIALS/FRAME

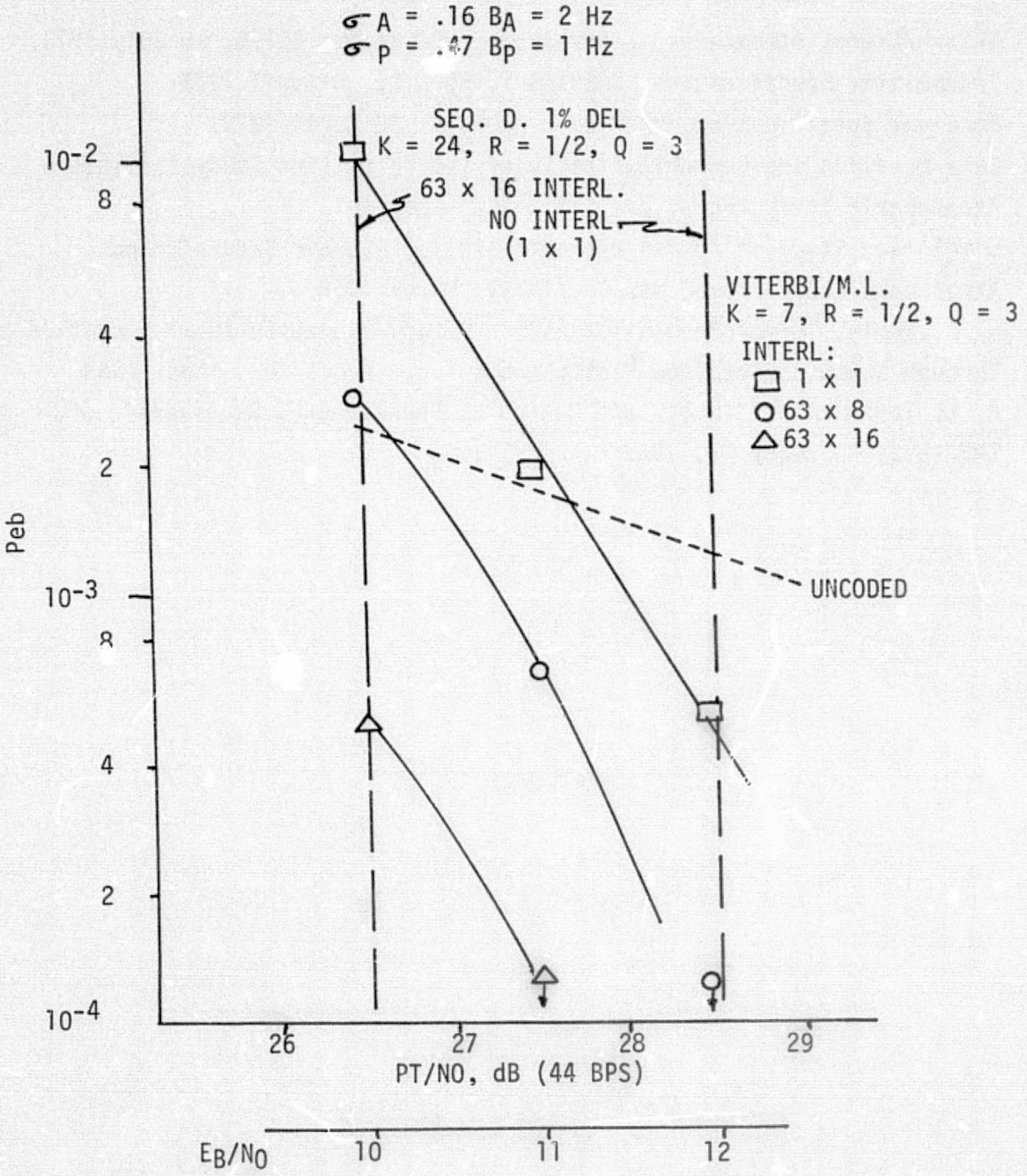

FIGURE 47

MODEM/CODING PERFORMANCE

REFERENCES

1. Saturn/Uranus Atmospheric Entry Probe, MDC Report E0870, 18 July 1973.
2. Transmitter Specification, SAEP-ES-7, Rev. B, 30 April 1973.
3. Receiver Specification, SAEP-ES-8, Rev. B. 30 April 1973.
4. Data Handling and Communication Subsystem Definition Study for Saturn Atmospheric Entry Probe, TRW S/N 23765, July 1973.
5. Simulation Study of Communications Link for Pioneer Saturn/Uranus Atmosphere Entry Probe, NAS CR-114739, March 1973.
6. G. L. Turin, "Error Probabilities for Binary Symmetric Ideal Reception Through Nonselective Slow Fading and Noise," Proc. IRE, Sept. 1958.
7. R. C. Tausworthe, "Theory and Design of Phase-Locked Receivers", JPL TR32-819, February 15, 1966.